Journal of
Materials Chemistry A

REVIEW

View Article Online
View Journal | View Issue

Published on 05 December 2014. Downloaded by Library for Natural Sciences of the RAS on 23/03/2015 11:48:51.

Cite this: *J. Mater. Chem. A*, 2015, **3**, 3182

# Noble metal-based composite nanomaterials fabricated *via* solution-based approaches

Hui Liu,[a] Yan Feng,[ab] Dong Chen,[ab] Chengyin Li,[ab] Penglei Cui[a] and Jun Yang*[a]

Received 29th October 2014
Accepted 2nd December 2014

DOI: 10.1039/c4ta05801a

www.rsc.org/MaterialsA

One of the key frontiers in nanomaterial fabrication is the integration of different materials within the same structure to increase functionality. In particular, interactions between nanoscale materials with distinctly different physical and chemical properties can greatly improve the overall application performance of the nanocomposites and can even generate new synergetic properties. Within the last decade, the development of wet-chemistry methods has led to the development of research in to composite nanomaterials. The efforts of many leading research groups have led to a rich variety of composite nanomaterials. However, the design and synthesis of composite nanomaterials with controlled properties remain a significant challenge. We devote this review for summarizing the solution-based methods used for the preparation of noble metal-based nanocomposites, their characterization and their potential applications in diverse areas to provide readers with a systematic and coherent overview of the field.

## 1 Introduction

We are currently witnessing impressive advances in nanoscience and nanotechnology. A variety of recipes have been developed to synthesize, assemble and package nanomaterials/nanostructures into forms more amenable for a wide range of applications.[1–17] After close to a decade of intense effort, many nanoparticles can now be produced with fairly good control over their shapes and sizes. A number of nanoparticle geometries, such as wires,[18] rods,[19] cubes,[12] and prisms,[11,20] can be routinely synthesized by solution chemistry methods in polar and non-polar environments. There is also an increased interest in the synthesis of more complex nanostructures because of their promising tunable properties for a new generation of technology-driven applications in catalysis,[21–24] chemical and biological sensing,[25,26] and optics.[19,27] As presented in this review, after the remarkable success in synthesizing more conventional hybrid nanomaterials, *e.g.*, core–shell,[28–31]

---

[a] *State Key Laboratory of Multiphase Complex Systems, Institute of Process Engineering, Chinese Academy of Sciences, Beijing, China 100190. E-mail: jyang@ipe.ac.cn; Fax: +86-10-8254-4915; Tel: +86-10-8254-4915*

[b] *University of Chinese Academy of Sciences, No. 19A Yuquan Road, Beijing, China 100049*

*Hui Liu studied Environmental Engineering at South-Central University for Nationalities (B.S. 2008) and Organic Chemistry at the University of Science and Technology, Beijing (M.S. 2010). She received her PhD with Prof. Jun YANG at the Institute of Process Engineering, Chinese Academy of Sciences (IPE-CAS) in 2014 and started as an Assistant Professor of the Materials for Energy Conversion and Environmental Remediation (MECER) Group at IPE-CAS in the same year. Her research interests focus on the synthesis of novel composite nanomaterials for energy conversion and environmental remediation, electrocatalysis, and the phase transfer-based extraction of heavy metals.*

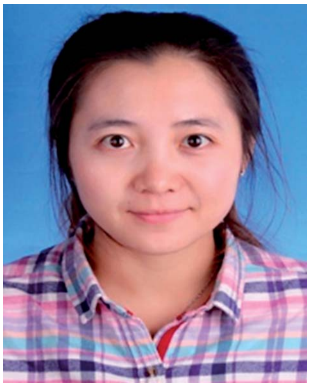

*Yan Feng received her BSc in Applied Chemistry in 2012 from the University of Jinan. She is currently a PhD student at the Institute of Process Engineering, Chinese Academy of Sciences (IPE-CAS). Her research focuses on the study of Pt-based nanocomposites as selective catalysts in direct methanol fuel cell reactions.*

This journal is © The Royal Society of Chemistry 2015

Published on 05 December 2014. Downloaded by Library for Natural Sciences of the RAS on 23/03/2015 11:48:51.

alloy,[32–34] and bimetallic heterostructures with controlled dimensions and intriguing morphologies,[35–41] increasing interest have been devoted towards the development of nanocomposites that consist of different classes of materials with solid-state interfaces.[42–61] The attracting factor of these nanostructured composites is that they combine materials with distinctly different physical and chemical properties to yield unique hybrid systems with tunable optical properties,[62,63] enhanced photocatalytic activities,[45,64–66] and ultrafast carrier dynamics.[67,68] Furthermore, interactions between the nanoscale metal and semiconductor components can greatly improve the overall application performance of the nanocomposites and can even generate new synergetic properties. For example, the metal ingredients in semiconductor–metal nanocomposites can enhance the photocatalytic and light-harvesting efficiencies of semiconductors by improving the charge separation and by increasing the light absorption.[69–71] In addition, as presented by Talapin and coworkers, contrary to the n-type PbS semiconductor, core–shell structured Au–PbS nanocomposites demonstrate strong p-type gate effects due to the intra-particle charge transfer. The energy level alignments of PbS and Au facilitate the electron transfer from the highest occupied $1S_h$ quantum confined state of the PbS shell to the Au core, which is analogous to the injection of mobile holes into the PbS shell.[72]

Composite nanomaterials based on noble metals would be particularly useful for catalytic applications. The adjacent domains of semiconductors or metal oxides with different electron affinities and appropriate energy level alignments could either donate or withdraw electrons from the noble metal domain through the nanometer contact at the interface of the nanocomposites, thus inducing changes in the electron density around the metal atoms. These changes in electron density would tune the catalytic property of noble metals by altering the adsorption of reactants on the metal catalyst. In addition, useful applications could also emerge in the field of photocatalysis because nanoscale sections of certain metals combined with semiconductors or metal oxides could allow the photogenerated charge carriers to perform redox reactions with high efficiency. Therefore, the potential for catalytic applications is expected to dramatically increase with increases in the complexity of the

*Dong Chen received his Master's degree from the College of Environmental and Energy Engineering in 2013 at the Beijing University of Technology. He is currently a PhD student at the Institute of Process Engineering, Chinese Academy of Sciences (IPE-CAS). His research focuses on the design and synthesis of Pd-based electrocatalysts for oxygen reduction and formic acid oxidation in proton exchange membrane fuel cells (PEMFCs).*

*Penglei Cui received her PhD in Chemical Engineering from Tianjin University in 2013, and then became an Assistant Professor at the Institute of Process Engineering, Chinese Academy of Sciences (IPE-CAS) in 2014. Her research interests focus on ionic liquid-based synthesis and the structural tuning of multi-metallic heterogeneous nanomaterials.*

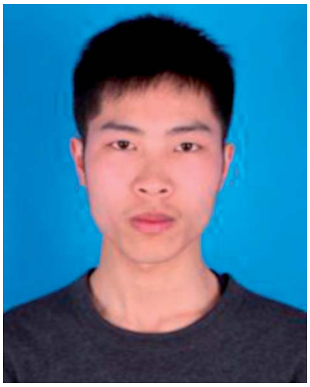

*Chengyin Li received his BSc in Chemical Engineering in 2013 from Nanjing University of Science and Technology. He is currently a Master's student at the Institute of Process Engineering, Chinese Academy of Sciences (IPE-CAS). His research focuses on the study of phase transfer-based extraction for the recovery of metal ions and its application in nanocrystal synthesis.*

*Jun Yang received his PhD in Chemical and Biomolecular Engineering in 2006 from the National University of Singapore (with Professor Jim Yang LEE). After completing postdoctoral research at Boston College and the University of Toronto, he joined the Institute of Bioengineering and Nanotechnology, Singapore in 2007. In 2010, he moved to the Institute of Process Engineering, Chinese Academy of Sciences, as the leader of the Group of Materials for Energy Conversion and Environmental Remediation (MECER). His main research interests include (i) applied catalysis, (ii) nanocomposites for energy conversion, (iii) the synthesis and application of novel nanocrystalline materials, and (iv) separation techniques.*

Published on 05 December 2014. Downloaded by Library for Natural Sciences of the RAS on 23/03/2015 11:48:51.

nanocomposites that can be fabricated. We will discuss these possible scenarios in more detail in the corresponding sections.

The early studies of metal-based nanocomposites involved different metals (*e.g.*, Au, Ag, and Pt) deposited on or doped in $TiO_2$ powders for photocatalytic applications.[73–79] In these structures, the metal domain induces charge equilibrium in photoexcited $TiO_2$ nanocrystals, which affects the energetics of the nanocomposites by shifting the Fermi level to more negative potentials. The shift in the Fermi level is indicative of the improved charge separation in $TiO_2$–metal systems, and is effective towards enhancing the photocatalytic efficiency.[64,65]

Only within the last decade the wet-chemistry methods have developed and become a powerful approach toward the synthesis of nanocomposites. In 2004, Banin and coworkers made a breakthrough in semiconductor–metal nanocomposites.[42] They demonstrated a solution synthesis for nanohybrids *via* the selective growth of gold tips on the apexes of hexagonal-phase CdSe nanorods at room temperature. The resulting novel nanostructures displayed modified optical properties due to strong coupling between the gold and semiconductor components. The gold tips showed increased conductivity, as well as selective chemical affinity for forming self-assembled chains of rods. The architecture of these nanostructures is qualitatively similar to bifunctional molecules such as dithiols, and provides a two-sided chemical connectivity for self-assembly and for electrical devices, as well as contact points for colloidal nanorods and tetrapods. These researchers later reported the synthesis of asymmetric semiconductor–metal heterostructures in which gold was grown on one side of CdSe nanocrystalline rods and dots. Theoretical modeling and experimental analysis showed that the one-sided nanocomposites were transformed from the two-sided architectures through a ripening process.[80] Subsequently, various approaches were developed for the synthesis of semiconductor or metal oxide–noble metal nanocomposites (*e.g.*, ZnO–Ag,[81,82] CdS–Au,[83,84] InAs–Au,[85] $TiO_2$–Co,[86] $Fe_3O_4$–Au,[87] $CoFe_2O_4$–Ag,[88] PbS–Au,[43,44,72,89,90] $Ag_2S$–Au,[48] and semiconductor–Pt systems[46,47,91,92]) by the anisotropic growth of metals on semiconductors through reduction, physical deposition, or photochemistry.

We therefore prefer to devote this review for summarizing the solution-based methods for the preparation of noble metal-based nanocomposites, their characterization and potential applications in catalysis to provide readers with a systematic and coherent overview of this field. Most of the works have only been carried out in the last few years, particularly by the authors in different laboratories. Regarding the great opportunities and tremendous challenges due to the accumulation in nanocomposites, in the final section of this review, we offer some perspectives for the future development of noble metal-based composite nanomaterials. The human being is at the interface of a number of forefront research areas in this period of technology development. We hope through this research effort, researchers can establish a general materials synthesis methodology to influence a rethinking of the current processing technologies: to move towards molecular-level control and regulation, and away from the "top-down" approach and the stringent and expensive control inherent in conventional manufacturing processes.

## 2 Phase transfer protocols for metal ions and nanoparticles

Metal nanoparticles of different shapes and sizes can be obtained in the organic phase by preparing them in the organic phase itself or by transferring nanoparticles from the aqueous phase to the organic phase. The latter has the advantage of leveraging the many existing methods for preparing metal nanoparticles in the aqueous phase.[93,94] In particular, the wet chemistry-based synthesis of nanomaterials including nanocomposites is often carried out in specific solvents. Therefore, the phase transfer of metal ions and nanoparticles is capable of creating favorable solvent surroundings for maximizing the advantages of wet chemistry approaches in fabricating noble metal-based nanocomposites with multiple functionalities.

The phase transfer of metal nanoparticles from aqueous solution to the organic phase is usually accomplished by capping nanoparticles with thiols and amines,[95] or by using surfactants to improve the solubility of nanoparticles in the organic phase.[96] The applications of phase transfer in metal nanoparticle synthesis and in the surface modifications of quantum dots have recently been reviewed in a number of articles.[97,98,99] Thus, this review does not intend to provide a comprehensive coverage of such topics. Instead, we devoted this section to a general protocol for the transfer of metal ions from aqueous solution to an organic medium after providing a brief update of the literature.[49] This transfer strategy involves mixing an aqueous solution of metal salts with an ethanol solution of dodecylamine, and then extracting the metal ions into an organic layer (*e.g.*, toluene, hexane or other non-polar solvents). It could be successfully applied towards the synthesis of a variety of metal, alloy and semiconductor nanoparticles. Compared with other general approaches,[100,101] this protocol allows metal or semiconductor nanocrystals to be synthesized in an organic medium using aqueous soluble metal salts as starting materials, which are relatively inexpensive and can be easily obtained. In addition, this protocol could also be extended to transfer a variety of noble metal nanoparticles from an aqueous phase to non-polar organic media. As shown in later sections, this phase transfer protocol is an important step preceding the fabrication of noble metal-based nanocomposites with favorable physical/chemical properties.

### 2.1 Brust–Schiffrin method

The often-cited Brust–Schiffrin method is the earliest approach employing phase transfer to prepare *thiol-stabilized nanoparticles*.[102,103] In this method, gold metal ions from an aqueous solution are extracted to a hydrocarbon (toluene) phase using tetraoctylammonium bromide (TOAB) as the phase transfer agent. A subsequent reduction occurs in the organic solution using an aqueous $NaBH_4$ solution in the presence of an alkanethiol, yielding Au particles with average diameter of $\sim$2.5 nm.

This journal is © The Royal Society of Chemistry 2015

Published on 05 December 2014. Downloaded by Library for Natural Sciences of the RAS on 23/03/2015 11:48:51.

The overall reaction is summarized in eqn (1) and (2), where the source of electrons is $NaBH_4$:[102]

$$AuCl_4^-(aq) + N(C_8H_{17})_4^+(C_6H_5Me) \rightarrow N(C_8H_{17})_4^+AuCl_4^-(C_6H_5Me) \quad (1)$$

$$mAuCl_4^-(C_6H_5Me) + nC_{12}H_{25}SH(C_6H_5Me) + 3me^- \rightarrow 4mCl^-(aq) + (Au_m)(C_{12}H_{25}SH)_n(C_6H_5Me) \quad (2)$$

Here, the nucleation and growth of the gold particles and the attachment of the thiol molecules simultaneously occur in a single step.

It should be noted that we emphasize the *thiol-stabilization* in the Brust–Schiffrin method. However, early in 1988, Meguro *et al.* reported the extraction of $H_2PtCl_6$ into organic solvents from an aqueous solution using dioctadecyldimethylammonium chloride, trioctylmethylammonium chloride, or trioctylphosphine oxide as the extractants.[104] In this process, $Pt^{4+}$ ions after extraction were reduced by formaldehyde or benzaldehyde in the presence of sodium hydroxide for several hours at 65 °C. The Pt particles obtained in $CHCl_3$, cyclohexane, or methylisobutylketone were very stable with diameters of 1.5–2.5 nm. Subsequently in 1989, they extended this extraction method for the preparation of organo–gold nanoparticles. The relationship between Au particle size and preparative condition was also discussed.[105]

Considerable subsequent work with modifications to this classic method ensued, including the use of alkanethiol of different chain lengths,[106,107–109] aromatic thiol,[110] dialkyl disulfides,[111] and various thiol/Au reactant ratios,[112] for the synthesis of monolayer-protected clusters (MPCs). In 1998, Murray's group employed hexanethiol instead of dodecanethiol as the stabilizer in a 3 : 1 thiol/Au ratio and chilled the reaction to yield a solution of clusters with a mean diameter of 1.6 nm and an average composition of $Au_{145}(S(CH_2)_5CH_3)_{50}$.[106] In their subsequent work,[113] the same group addressed specific issues of particle growth and monodispersity issues in the preparation of hexanethiol-protected Au clusters by monitoring the size evolution of the particles over the course of 125 h. The researchers found that the average diameter of the Au core gradually increased over the first 60 h of the reaction and then remained largely unchanged afterward (up to 125 h) at *ca.* 3 nm. The results support the findings that MPCs of the smallest core size could be best obtained by quenching the reaction at a relatively early time,[112,114,115] and thus were important for understanding how MPC core sizes evolve in the Brust–Schiffrin cluster synthetic reaction.

Further insights can be derived from the similar treatment of platinum, lending greater understanding for the preparation of other noble metal nanomaterials. Early in 1999, the Brust–Schiffrin method was also extended by Horswell and coworkers for the synthesis of isocyanide-protected platinum nanoparticles.[116] The authors followed every step of the Brust–Schiffrin method to prepare tetraoctylammonium-stabilized Pt nanoparticles, which were further functionalized by dodecyl isocyanide *via* a ligand exchange process. Transmission electron microscopy (TEM) showed that Pt particles of 1–3 nm in diameter with well-defined crystalline structure were obtained this way.

The Brust–Schiffrin method for nanoparticle synthesis was then extended to generate amine-stabilized nanoparticles by simply substituting an appropriate amine for the thiol. Leff *et al.* first reported the synthesis of amine-stabilized Au nanoparticles using the Brust–Schiffrin method by substituting the dodecanethiol with dodecylamine or oleylamine.[117] Larger Au nanoparticles with diameters up to 7 nm could be accessed by this modified Brust–Schiffrin method. In a later work, Wikander *et al.* used tetrakisdecylammonium bromide instead of tetraoctylammonium bromide to transfer platinum(IV) chloride from an aqueous solution to toluene, and then reduced the platinum ions using $NaBH_4$ in the presence of alkylamine of different chain lengths. This research demonstrated that the length of the primary amine chains used to coat the platinum nanoparticles could be used to control the nanoparticle size (Fig. 1). The calculated average diameter indicated that there is an inverse relationship between the size of the nanoparticles and the length of the alkylamine. The inspection of the TEM images reveals that Pt nanoparticles are more spherical in shape when short-chain alkylamine are used rather than their longer-chain homologues.[118]

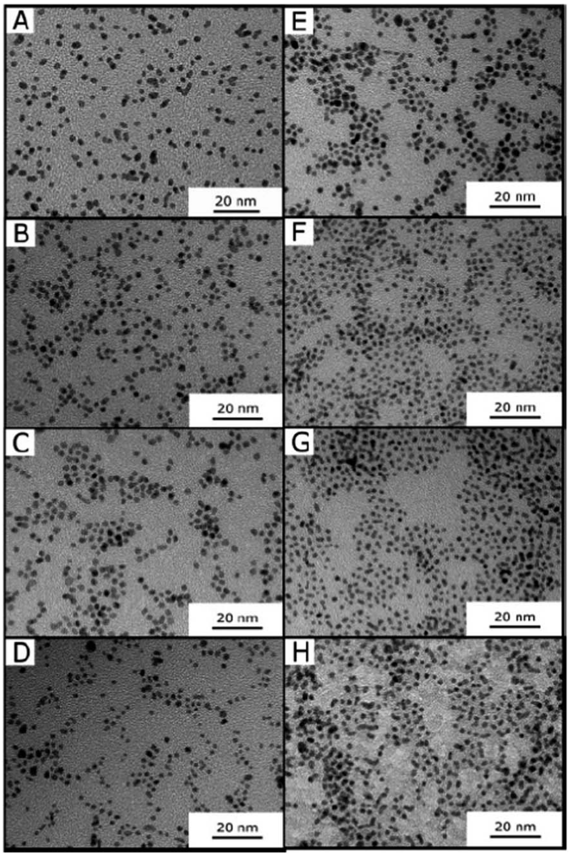

Fig. 1 TEM images of platinum nanocrystals obtained by phase-transfer method using different alkylamines as stabilizing agents: (A) $C_6NH_2$, (B) $C_7NH_2$, (C) $C_8NH_2$, (D) $C_9NH_2$, (E) $C_{10}NH_2$, (F) $C_{12}NH_2$, (G) $C_{16}NH_2$, and (H) $C_{18}NH_2$. Reproduced from ref. 118 with permission from the American Chemical Society.

Published on 05 December 2014. Downloaded by Library for Natural Sciences of the RAS on 23/03/2015 11:48:51.

The extension of Brust–Schiffrin method for the syntheses of nanomaterials is still very active and continues to be a useful tool to prepare Au, Ag, or Pt nanoparticles with controlled size and improved dispersity.[119–121] With a suitable choice of phase transfer agent, the Brust–Schiffrin method has also been employed to produce Cu,[122] CoPt alloy,[123] $Ag_2S$,[124,125] and PbS.[126] However, because the phase transfer agent and the stabilizer for particles in Brust–Schiffrin syntheses are chemically different, the nanoparticles so obtained were found to contain nitrogenous surface impurities due to the phase-transfer agent. In addition to this contamination problem, the greatest limitation of the Brust–Schiffrin preparation is that the stabilizing ligands, such as thiol or amine, must be compatible with all of the reagents, including the reducing (*i.e.*, $NaBH_4$) and phase transfer agents, thus avoiding adverse influences on the reaction chemistry.

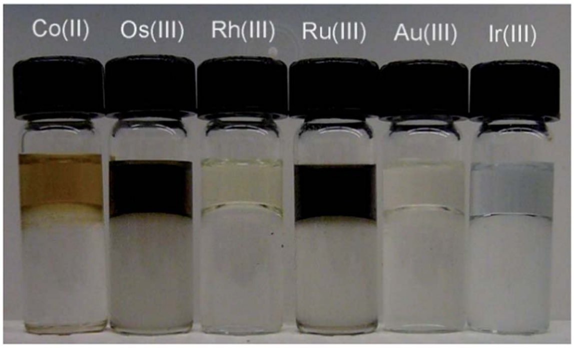

Fig. 2 Images showing the successful transfer of Co(II), Os(III), Rh(III), Ru(III), Au(III), and Ir(III) metal ions from an aqueous phase to toluene. Reproduced from ref. 49 with permission from the Nature Publishing Group.

### 2.2 Ethanol-mediated phase transfer

Notwithstanding the contamination issue, the Brust–Schiffrin method should be recognized for its ability to produce finer metallic nanoparticles. Furthermore, an ethanol-mediated protocol, in which alkylamine is used as a stabilizer-cum-phase transfer agent, has been developed to realize the distinctive advantage of the Brust–Schiffrin method without its associated problem of impurity contamination.[49] This protocol is also generic enough for the transition metal ions and can be easily extended to the preparation of metallic and semiconductor nanocrystals with finer sizes.

The transfer of metal precursors from the aqueous solution to the hydrocarbon layer is a two-step approach.[49] Typically, the aqueous solution of metal ions is mixed with an equal volume of ethanol containing dodecylamine (DDA) and the mixture is stirred for 3 minutes. Then, toluene is added and stirring is continued for 1 more minute before transferring the mixture to a separating funnel. The formation of two immiscible layers occurs within a few minutes. The transfer of metal salts from the aqueous phase to toluene then completes, leaving behind a colorless aqueous solution. Ethanol is important for the transfer of metal precursors. Metal ions would otherwise not be transferred to the organic phase by the direct mixing of an aqueous metal precursor solution with an organic solvent containing DDA. Prolonged agitation would only result in a turbid mixture of metal salt solution and organic solvent, but no transfer of metal ions took place after the mixture settled down into two immiscible layers in the separating funnel. However, the transfer of metal ions could occur using ethanol as an intermediate solvent based on the fact that water and ethanol are miscible, and this ensures the maximum contact between the metal ions and DDA. Fig. 2 illustrates the complete bleaching of the aqueous phase as the metal ions are successfully transferred from water to toluene.

The mechanism of this protocol was different from that of the Brust–Schiffrin method in which the gold ions from an aqueous solution were directly transferred to a hydrocarbon phase (toluene) based on the electrostatic interaction with tetraoctylammonium bromide.[102,103] It was hypothesized that a metal complex between the metal ions and DDA was formed in the process, which could then be more easily extracted by toluene.[49] Analyses by inductively coupled plasma-atomic emission spectrophotometry (ICP-AES) indicated that the phase transfer efficiencies for a wide variety of metal ions were higher than 95%.

After transfer into the organic solvent, a large number of commonly used methods, *e.g.*, wet chemistry reduction, seed-mediated growth, co-reduction, and solvothermal approaches could be adopted to produce metal or semiconductor nanoparticles with different structures or morphologies. The synthesis of noble metal nanoparticles could thus serve as a typical example to demonstrate the extension of this transfer protocol to nanomaterial preparation. At 100 °C, the reducing agent solution (*i.e.*, a toluene solution of hexadecanediol, tetrabutylammonium borohydride or an aqueous solution of $NaBH_4$) was added to the toluene solution of the noble metal precursor (*i.e.*, $Ru^{3+}$, $Rh^{3+}$, $Pd^{2+}$, $Ag^{+}$, $Os^{3+}$, $Ir^{3+}$, $Pt^{2+}$, $Pt^{4+}$, or $Au^{3+}$), and the mixture was agitated for several minutes. The noble metal colloids thus obtained were highly stable, and showed no sign of agglomeration, even after weeks of storage. The synthesis could be easily scaled up by proportionately increasing the volumes of the metal ion aqueous solution, DDA ethanolic solution and toluene. The nanoparticles and nanostructures synthesized with this phase transfer protocol include monometallic, bimetallic alloy and core–shell, and semiconductors (Fig. 3). Compared with other general approaches,[100,101] this protocol allows the synthesis of nanocrystals to be performed in an organic medium using aqueous soluble metal salts as the starting materials, which are relatively inexpensive and can be easily obtained. As demonstrated in later sections, a notable advantage of this transfer protocol is that it could be easily extended to synthesize a large number of semiconductor–noble metal composite nanomaterials, an important challenge in current materials synthesis.[42,43,48,60,98] Thus, this universal phase transfer approach represents a simple and flexible route for fabricating nanostructured materials with novel structures and multiple functionalities.

Published on 05 December 2014. Downloaded by Library for Natural Sciences of the RAS on 23/03/2015 11:48:51.

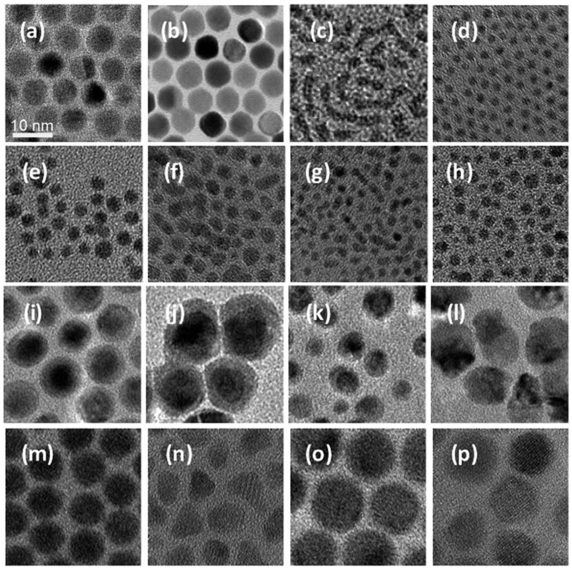

Fig. 3 TEM images of metal nanoparticles. (a) Ag derived with HDD. (b) Au, (c) worm-like Pd, and (d) Pt from Pt(IV) derived with TBAB. Alloy nanoparticles of (e) Ag–Au, (f) Pd–Pt, (g) Pt–Rh, and (h) Pt–Ru synthesized by co-reduction of the metal precursors with TBAB. Core–shell nanoparticles of (i) 7.4 nm Au@Ag, (j) 12.7 nm Au@Ag, (k) 3.9 nm Pt@Ag, and (l) 9.2 nm Pt@Ag synthesized by seed-mediated growth. Semiconductor nanocrystals of (m) $Ag_2S$, (n) CdS, (o) HgS, and (p) PbS. Reproduced from ref. 49 with permission from the Nature Publishing Group.

The ethanol-mediated phase transfer method, described in the previous section, is also applicable for the transfer of a large variety of noble metal nanoparticles from the aqueous phase to a hydrocarbon layer.[98,127,128] Analogous to the formation of metal ion–DDA complexes, ethanol-mediated transfer for noble metal nanoparticles is primarily based on the formation of uniform alkylamine-stabilized metal nanoparticles through a stabilizer exchange process that involves the mixing of the metal hydrosol and an ethanol solution of DDA, and then the extraction of DDA-stabilized metal nanoparticles into toluene. The typical experiment follows the same steps for transferring metal ions from aqueous phase to a nonpolar organic medium. For example, citrate-stabilized metal hydrosol prepared by the $NaBH_4$ reduction of metal precursors was mixed with an equal volume of ethanol containing dodecylamine, and the mixture was stirred for 2 minutes. Then, toluene was added and the stirring was continued for 3 more minutes. DDA-stabilized metal nanoparticles were rapidly extracted into the toluene layer, leaving behind a colorless aqueous solution.[127] This ethanol-mediated transfer method could be used to transfer metal nanoparticles capped by a variety of surfactants such as sodium acetate, polyvinylpyrrolidone (PVP), bis(*p*-sulfonatophenyl)-phenylphosphine (BSPP), or Triton X-100.[129,130] This process was also applicable to transfer nanoparticles prepared by the $NaBH_4$ reduction of metal precursors without a stabilizer. In comparison with the procedure reported by Sarathy and coworkers,[131,132] where concentrated HCl has to be used to facilitate the nanoparticle transfer, the ethanol-mediated method is considerably gentler. In addition to its generic applicability, it offers ease of operation and is compatible with the transfer of metals that are reactive towards concentrated HCl.

## 3 Nanocomposites of gold and semiconductors

Nanocomposites constructed by depositing gold on the surface of semiconductor nanocrystals are among the most studied nanocomposites.[42–45,48–51,80–92,98,133] The deposition of noble metals on the surface of semiconductor nanocrystals is usually conducted in a nonpolar organic solvent *via* a seed-mediated growth at room temperature. In detail, high quality semiconductor nanocrystals are first prepared in an organic solvent at elevated temperatures, and simultaneously the metal precursors are also transferred into nonpolar organic solvent using established methods. The semiconductor organosol and the metal precursor solution in organic solvent are then mixed together, followed by the addition of a weak reducing agent (usually dodecylamine, DDA). The DDA reduces the metal precursors into metal atoms in the presence of semiconductor nanocrystals, which nucleate and grow on the surface of semiconductor nanocrystals, resulting in the formation of semiconductor–noble metal nanocomposites. Usually, noble metal precursors cannot dissolve in nonpolar organic solvents; however, for gold, there are a number of approaches, *e.g.*, the Brust–Schiffrin method,[102,103] the general phase transfer protocol introduced in the previous section,[49] and the dodecyldimethylammonium (DDAB)-facilitated strategy developed by Banin and coworkers,[42] which could be used to transfer its precursors, *e.g.*, commonly used $HAuCl_4$, from the aqueous phase to nonpolar organic solvents. In addition, the successful deposition of noble metals on the surface of semiconductor nanocrystals has some specific requirements for the reducing agent; for example, very strong reducing agent, *e.g.*, $NaBH_4$, can lead to a separate nucleation of the noble metal atoms in the solution instead of their growth on the semiconductor nanocrystals. Therefore, although the general phase transfer protocol could assist a wide variety of metal precursors to dissolve in nonpolar organic solvents, only the deposition of gold on the surface of semiconductor nanocrystals has been extensively studied over the past decade.

### 3.1 Deposition of Au on the surface of semiconductor nanocrystals

Banin and coworkers are pioneers in the preparation of nanocomposites consisting of a semiconductor and gold, and they made a huge breakthrough in 2004.[42] They demonstrated a solution synthesis for nanocomposites *via* the selective growth of gold tips on the apexes of hexagonal-phase CdSe nanorods at room temperature. The authors prepared CdSe rods and tetrapods of different dimensions by the high-temperature pyrolysis of suitable precursors in a coordinating solvent containing a mixture of trioctylphosphineoxide and phosphonic acids. They dissolved $AuCl_3$ in toluene with the addition of dodecyldimethylammonium bromide (DDAB) and dodecylamine, which

Published on 05 December 2014. Downloaded by Library for Natural Sciences of the RAS on 23/03/2015 11:48:51.

serve as reducing agents. Then, they mixed this solution at room temperature with a toluene solution of the colloidal-grown CdSe nanorods or tetrapods. After the reaction, the composite products were precipitated by the addition of methanol, separated by centrifugation, and then re-dispersed in toluene for further characterization. The novel nanostructures displayed modified optical properties due to the strong coupling between the gold and semiconductor components. The gold tips showed increased conductivity, as well as selective chemical affinity for forming the self-assembled chains of rods. The architecture of these nanostructures was qualitatively similar to bifunctional molecules such as dithiols, which provided two-sided chemical connectivity for self-assembly and for electrical devices, as well as contacting points for colloidal nanorods and tetrapods. These researchers later reported the synthesis of asymmetric semiconductor–metal heterostructures in which gold was grown on one side of CdSe nanocrystalline rods and dots, as displayed in Fig. 4. Theoretical modeling and experimental analysis showed that the one-sided nanocomposites were transformed from the two-sided architectures through a ripening process.[80]

Banin's group further explored the growth mechanism of gold nanocrystals onto preformed cadmium sulfide nanorods to form hybrid metal nanocrystal/semiconductor nanorod colloids.[83] By manipulating the growth conditions, they obtained nanostructures that exhibited Au nanocrystal growth at only one nanorod tip, at both tips, or at multiple locations along the nanorod surface. Under anaerobic conditions, they found that the growth of Au occurs only at one tip of the nanorods; thus, generating asymmetric structures. In contrast, the presence of oxygen and trace amounts of water during the reaction promotes etching of the nanorod surface, which provides additional sites for metal deposition, as shown in the scheme in Fig. 5. Three growth stages are observed when Au growth is carried out under air: (1) Au nanocrystal formation at both nanorod tips, (2) growth onto defect sites on the nanorod surface, and finally (3) a ripening process, in which one nanocrystal tip grows at the expense of the other particles present on the nanorod. An analysis of the hybrid nanostructures by high-resolution TEM shows that there is no preferred orientation between the Au nanocrystal and the CdS nanorod, indicating that the growth is nonepitaxial. The optical signatures of the nanocrystals and the nanorods (*i.e.*, the surface plasmon and first exciton transition peaks, respectively) are spectrally distinct; thus, allowing the different stages of the growth process to be easily monitored. The initial CdS nanorods exhibit a band gap and trap state emission; both are quenched during Au growth.

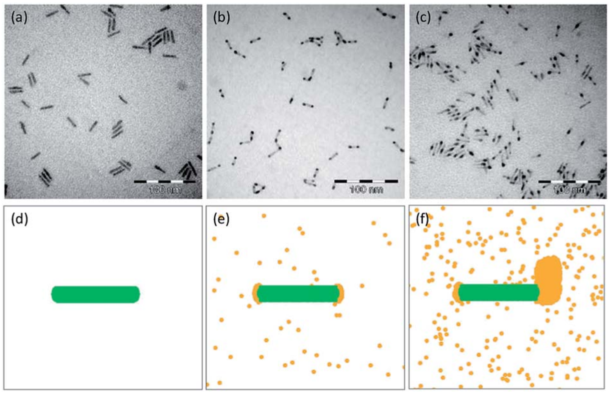

Fig. 4 Effect of increasing Au/rod molar ratio on growth. The top panels show the experimental results. (a) Original rods of dimension 25 × 4 nm$^2$. (b) NDBs after adding 1.3 μmol of gold precursors to (a). (c) NBTs after adding 1.3 μmol of gold precursors to (b). The lower panels show the theoretical results. (d) Presentation of the system on a two-dimensional lattice. (e) Image of the final morphology at a low gold concentration (the two-dimensional gold density is $\rho_g = 0.001$) yielding a two-sided growth. (f) Image of the final morphology at a high gold density ($\rho_g = 0.01$) showing a one-sided growth. Reproduced from ref. 80 with permission from the Nature Publishing Group.

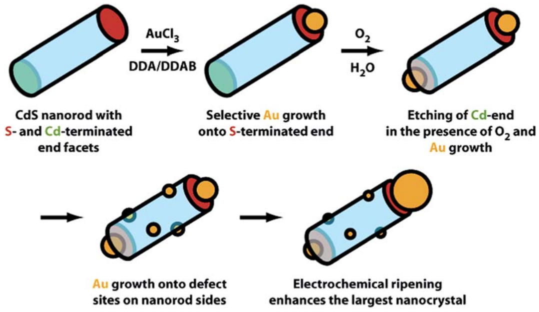

Fig. 5 Schematic of the growth process of Au nanocrystals onto CdS nanorods. Without oxygen, gold grows only at one tip. In the presence of oxygen, the Cd-terminated end is etched, providing a second high-energy site for gold growth, followed by a side growth. With long reaction times, the gold growth ceases and electrochemical ripening leads to the migration of gold from the smallest nanocrystals to the largest nanocrystal. Reproduced from ref. 45 with permission from the American Chemical Society.

Banin and coworkers also studied the photocatalytic properties of nanocomposites consisting of CdSe nanorods and gold

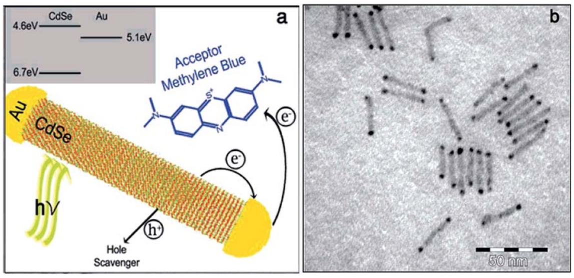

Fig. 6 (a) Scheme of a light-induced charge separation mechanism in a CdSe–Au composite particle in which the photogenerated electron–hole pair separates so that the electron resides at the gold tip and the hole at the CdSe nanorod. The scheme also depicts the transfer of the hole to the scavenger and the reduction of the methylene blue molecule upon electron transfer from the gold tip. The inset shows the energy band alignment between CdSe and Au. (b) TEM image of CdSe–Au nanocomposites synthesized in aqueous solution. Reproduced from ref. 83 with permission from the American Chemical Society.

This journal is © The Royal Society of Chemistry 2015

Published on 05 December 2014. Downloaded by Library for Natural Sciences of the RAS on 23/03/2015 11:48:51.

nanoparticles.[45] They found that under visible light irradiation, a charge separation could take place between the semiconductor and the metal parts of the composite particles (Fig. 6a). Analysis of the band offsets between Au and CdSe suggests that this is due to a rapid electron transfer from the conduction band of CdSe to the Au tips, leading to a charge separation (inset of Fig. 6a).[134,135] To perform the photocatalysis in the aqueous phase, Banin and coworkers developed a method to directly deposit gold on the surface of CdSe nanorods in aqueous phase instead of transferring the CdSe–Au nanocomposites from an organic solvent to the aqueous phase *via* ligand exchange reactions because the latter is time-consuming and difficult to realize for large amounts.[66] In their new approach, CdSe nanorods were grown by a high-temperature pyrolysis of suitable precursors in a coordinating solvent containing a mixture of trioctylphosphineoxide and phosphonic acids.[136] The CdSe nanorods were then transferred to the aqueous phase by exchanging the surface ligands to mercaptoundecanoic acid (MUA),[66,137] leading to the formation of a stable hydrosol of CdSe nanorods. Then, CdSe–Au nanocomposites with a selective growth of Au at both CdSe rod tips were obtained by adding an aqueous gold precursor solution ($HAuCl_4$) to the CdSe hydrosol with vigorous stirring and under ambient light (Fig. 6b), which displayed a superior catalytic property for the direct photoreduction of a model acceptor molecule, *i.e.*, methylene blue.

In addition to their excellent work in the synthesis, characterization, and application of semiconductor–gold nanocomposites, Banin's group also revealed some unique scientific phenomena in composite nanomaterials. For example, they reported an interesting diffusion of gold into InAs semiconductor nanocrystals at room temperature.[85] The diffusion of Au occurs either in solution or in a solid-state reaction. In the first stage, gold patches are grown on the nanocrystal surface, and a further increase in the gold concentration, or waiting for 24 h, gold diffuses into the nanocrystals. This behavior differs from the case of CdSe, where Au grows on the surface and ripens to form one gold patch in high concentration. As a result of the Au diffusion, InAs is converted into an amorphous InAs or oxidized shell (Fig. 7). The diffusion process found by them might offer a new strategy for metal doping in semiconductor nanoparticles.

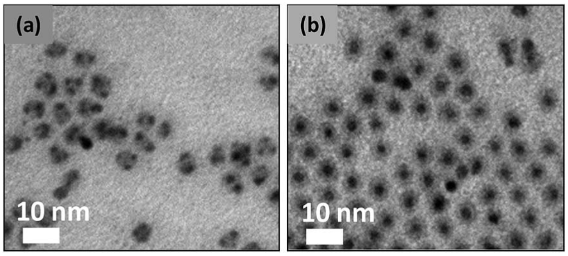

Fig. 7 TEM images of InAs nanocrystals after treatment with gold in toluene solution as a function of increasing gold concentration: (a) after adding $2.75 \times 10^{-6}$ mol of gold; (b) after adding $5.5 \times 10^{-6}$ mol of gold. Reproduced from ref. 85 with permission from Wiley-VCH.

Following the breakthrough made by Banin's group, various strategies have been developed for the synthesis of semiconductor–Au nanocomposites by the anisotropic growth of gold on the surface of semiconductor nanocrystals through reduction, physical deposition or photochemistry. The structure displayed in Fig. 8 for the nanocomposites composed of PbS and gold was reported by Yang and coworkers.[89] They chose to use PbS prepared in oleylamine as the target semiconductor nanocrystal because it has a typical cubic crystal structure and can be easily produced in controlled shapes and sizes. They dissolved gold precursors into toluene using Brust–Schiffrin method,[102,103] and then mixed them together, followed by the addition of dodecylamine as a reducing agent, which resulted in the formation of PbS–Au nanocomposites. High quality and monodisperse PbS–$Au_1$ and PbS–$Au_4$ nanostructures and PbS–$Au_n$ nanocubes could be obtained by controlling the molar ratio of PbS and Au precursors. The authors provided a reasonable method to control the size, number, and distribution of gold nanocrystals on semiconductors, which is important to assist the design and fabrication of composite nanomaterials for catalysis, optoelectronic devices, and chemical/biological sensors. Owing to their narrow size distribution and intrinsic high symmetry, the as-synthesized PbS–$Au_4$ nanocomposites could easily self-assemble into hexagonal arrays. Nonlinear optical measurements show that the PbS–$Au_4$ nanostructure could alter the nonlinear response time of PbS nanocrystals; thus, confirming the applicability of the metal-decorated semiconductor nanocrystals in the development of saturable absorber devices.

Collaborating with Zeng and Swihart, Prasad's group reported a universal approach for the synthesis of ternary nanocomposites consisting of metal oxide, gold, and

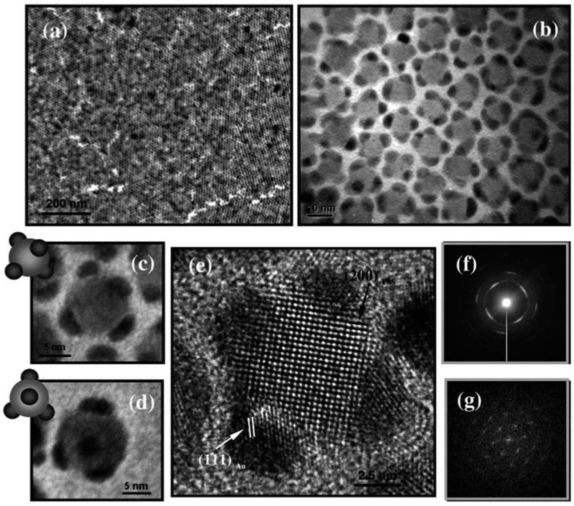

Fig. 8 (a and b) TEM images of the ordered array of PbS–$Au_4$ heterogeneous nanostructures; (c and d) TEM images of a typical PbS–$Au_4$ nanostructure; (e) HRTEM image of a typical PbS–$Au_4$ nanostructure; (f) SAED pattern; and (g) FFT pattern obtained from the ordered array of PbS–$Au_4$ heterogeneous nanostructures. Reproduced from ref. 89 with permission from the American Chemical Society.

Published on 05 December 2014. Downloaded by Library for Natural Sciences of the RAS on 23/03/2015 11:48:51.

semiconductors, as demonstrated in Fig. 9.[43] In brief, they mixed PbO, oleic acid, and phenyl ether in a three-necked flask set on a heating mantle. Under argon gas flow, the mixture was heated to 120 °C until a Pb-oleate complex was formed. Then, the pre-prepared peanut-like $Fe_3O_4$–Au nanoparticles in hexane were injected, and the hexane was distilled out. Subsequently, a trioctylphosphine (TOP) solution of selenium was rapidly injected into the reaction mixture at 160 °C. The final ternary $Fe_3O_4$–Au–PbSe nanocomposites were then withdrawn, washed with acetone under air, followed by centrifugation, and then re-dispersed in hexane. The authors found that the heating strategy and seed particle dimensions were important for forming ternary hybrids. For instance, if the gold component was less than 3 nm in diameter, then the nucleation of PbS or PbSe was difficult, presumably because of the small amount of gold surface area exposed. Moreover, for the ternary $Fe_3O_4$–Au–PbS nanocomposites, if the temperature of the reaction mixture was quickly increased to 150 °C after sulfur injection, both dumbbell-like Au–$Fe_3O_4$ hybrid nanoparticles and $Fe_3O_4$–Au–PbS ternary composite nanoparticles were formed. This suggests that some Au–$Fe_3O_4$ peanut-like particles aggregated to form dumbbell-like Au–$Fe_3O_4$ particles in the presence of sulfur before PbS could nucleate and grow on Au–$Fe_3O_4$. The multifunctional nanocomposites that combine magnetic, plasmonic, and semiconducting properties and that are tunable in size and morphology could be obtained. Furthermore, the properties of each component within the hybrids could be strongly modulated by the conjugating component(s) aided by the coherent interfaces between them. In particular, the self-assembling of these nanoparticles into thin films and bulk materials could lead to composite materials with tremendous design freedom, geometric complexity, and multifunctionality.

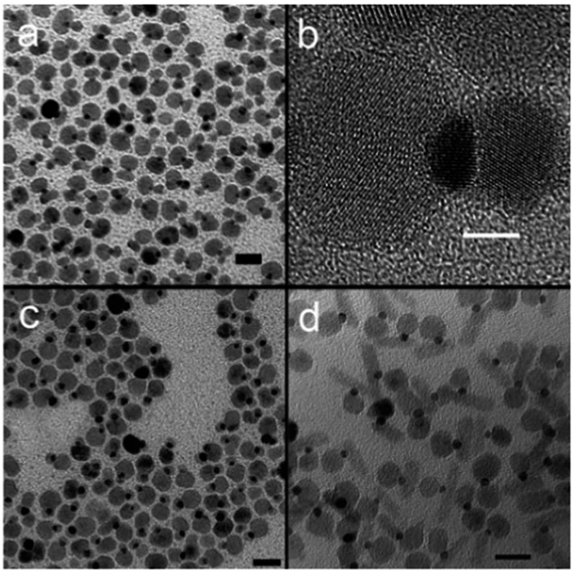

Fig. 9 TEM images (a, c, and d) and HRTEM image (b) of $Fe_3O_4$–Au–PbSe (a and b) and $Fe_3O_4$–Au–PbS (c and d) ternary hybrid nanoparticles. The scale bars are 20 nm in (a), (c), and (d) and 4 nm in (b). Reproduced from ref. 43 with permission from the American Chemical Society.

Based on the morphology of the pre-prepared semiconductor nanocrystals, nanocomposites with unique architecture could be obtained after integrating with gold. Qi and coworkers demonstrated the preparation of uniform PbS–Au nanostar–nanoparticle heterodimers consisting of one Au nanoparticle grown on one horn of a well-defined six-horn PbS nanostar using the PbS nanostars as growth substrates for the selective deposition of Au nanoparticles.[51] They produced uniform, well-defined, star-shaped PbS nanocrystals with six horns using the method they previously developed,[138] as shown in Fig. 10a. The synthesis of PbS–Au nanostar–nanoparticle heterodimers with an Au tip on one horn was achieved by the reduction of $HAuCl_4$ with ascorbic acid in an aqueous dispersion of PbS nanostars in the presence of CTAB. The microscopic image in Fig. 10b shows the PbS–Au heterostructures obtained with a PbS concentration of 0.48 mM at 27 °C, indicating the exclusive formation of uniform nanostar–nanoparticle heterodimers consisting of PbS nanostars of ~80 nm and gold nanoparticles of ~50 nm. An enlarged TEM image is shown in Fig. 10c, which clearly shows that one gold nanoparticle is preferentially grown on one horn of the PbS nanostar. The single crystallinity of the PbS stars is further confirmed by the HRTEM image shown in Fig. 10d, while the crystalline nature of the Au nanoparticles is confirmed by the HRTEM image shown in Fig. 10e. The related XRD pattern (Fig. 10f) shows sharp peaks corresponding to cubic PbS

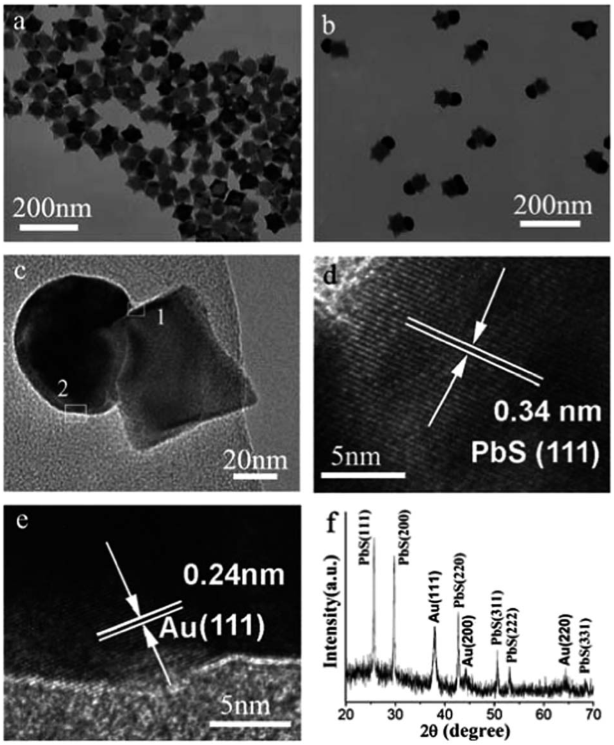

Fig. 10 (a) TEM image of PbS nanostars. (b), (c) TEM images. (d), (e) HRTEM images and (f) XRD pattern of PbS–Au nanostar-nanoparticle heterodimers formed with [PbS] = 0.48 mM at 27 °C. The HRTEM images shown in (d) and (e) correspond to the framed areas 1 and 2 in (c), respectively. Reproduced from ref. 51 with permission from the Royal Society of Chemistry.

This journal is © The Royal Society of Chemistry 2015

Published on 05 December 2014. Downloaded by Library for Natural Sciences of the RAS on 23/03/2015 11:48:51.

with a rock salt structure and cubic gold. The size of the Au nanoparticles on the horns of the PbS nanostars could be readily adjusted by changing the PbS concentration for the deposition of Au nanoparticles. Furthermore, unusual PbS–Au nanoframe–nanoparticle heterodimers could be obtained after etching the PbS–Au nanostar–nanoparticle heterodimers using 0.05 M oxalic acid, which might be promising candidates as anisotropic nanoscale building blocks for the controlled assembly of useful, complex architectures.

When the synthesis order was reversed, *e.g.*, in the synthesis of semiconductor nanocrystals in the presence of previously formed gold nanoparticles, the nanocomposites thus obtained usually have a core–shell structure.[48,52,72,139] In an early study, Talapin's group reported the synthesis of core–shell Au@PbS nanocomposites.[74] Typically, they added PbO and oleic acid in 1-octadecene (ODE), and heated the mixture to 150 °C under vacuum to form a Pb-oleate complex. After cooling the reaction mixture to 100 °C, dodecanethiol-capped Au nanoparticles with an average size of 4.2 nm dispersed in 1 mL of toluene were added and toluene was distilled out. The growth of PbS shells was initiated by the injection of 0.13 mL of bis(trimethylsilyl) sulfide dissolved in 2 mL of ODE with vigorous stirring. The reaction mixture was maintained at the injection temperature for 5–10 min and then cooled to the room temperature, followed by the purification of nanocrystals from the crude solution. The Au@PbS core–shell nanocomposites thus obtained (Fig. 11) could form stable colloidal solutions in chloroform, toluene, and tetrachloroethylene. The thickness of the PbS shell could be tuned by the reaction time, concentration of Au seeds, and amount of injected sulfur precursor. In the Au@PbS core–shells, the authors observed an enhancement of the absorption cross-section due to a synergistic coupling between the plasmon and exciton in the core and shell, correspondingly. Field-effect devices with channels assembled from arrays of Au@PbS core–shell nanostructures demonstrated strong p-type doping, which they attributed to the formation of an intra-particle charge transfer complex. Their work might provide the starting guidelines for designing solution-processed semiconductors with enhanced absorbance and controlled electronic doping for photovoltaic and thermoelectric applications. The core–shell morphology maximizes the interaction between the components and provides a convenient platform for studying exciton–plasmon interactions and other fundamental phenomena at the nanoscale level. Their approach can be applied to a variety of material combinations, such as metal–semiconductor and semiconductor–magnetic material.

Yu, Wang, and coworkers employed an alternative approach to generate Au@CdS nanocomposites with core–shell construction.[52] As illustrated by the scheme in Fig. 12, the gold nanorods used as starting materials were synthesized in aqueous solutions using a seed-mediated growth method.[4,140] Their protocol included three steps to obtain Au–Ag, Au–$Ag_2S$, and Au–CdS nanorods: (i) Ag shell growth. First, the silver shell can be easily grown on the gold nanorods because of the perfect match of the lattice constants of the two metals. (ii) $Ag_2S$ shell growth. Because the electronegativity of Ag is similar to that of many anions, the Ag shells can easily be modified to form silver compound shells.[49,63,141,142] $Ag_2S$ shells were obtained by adding excess of sulfur in a growth solution containing Au–Ag nanorods. (iii) CdS shell growth. The $Ag_2S$ layer coated on the Au nanorods was converted to the CdS shell through cation exchange reactions between $Ag^+$ and $Cd^{2+}$ precursors ($Cd(NO_3)_2$),[143,144] which could be further accelerated by adding $NaBH_4$. The final Au@CdS composite products had complete core–shell structures, and the shell thickness could be controlled from about 4.5 to 15.0 nm by regulating the molar ratio of Cd/Au in the reaction solution. The exciton–plasmon interactions observed in the Au@CdS nanorods induce a shell thickness-tailored and red-shifted longitudinal surface

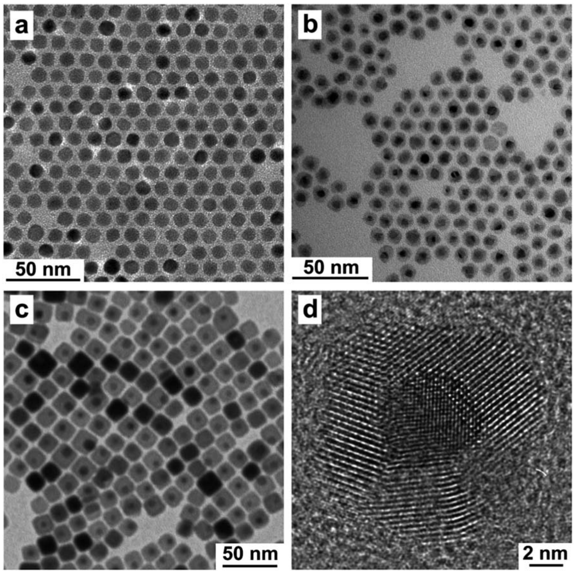

Fig. 11 TEM images of (a) PbS nanocrystals and (b–d) Au–PbS nanostructures. (c) Cubic Au–PbS nanostructures synthesized at 150 °C. (d) Representative high-resolution TEM image of an Au–PbS core–shell nanostructure. Reproduced from ref. 72 with permission from the American Chemical Society.

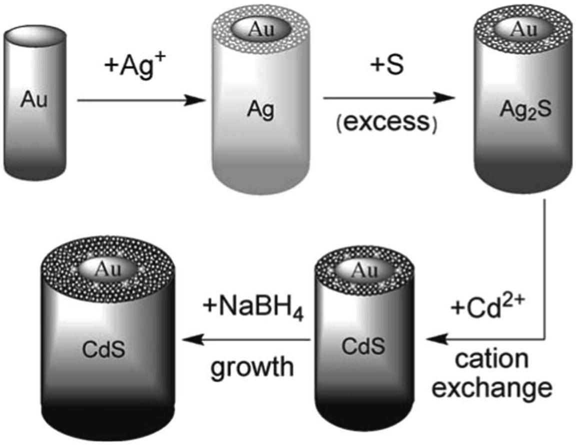

Fig. 12 Growth scheme of Au@CdS core–shell nanorods. Reproduced from ref. 145 with permission from Wiley-VCH.

Published on 05 December 2014. Downloaded by Library for Natural Sciences of the RAS on 23/03/2015 11:48:51.

plasmon resonance and quench CdS luminescence under ultraviolet light excitation. Furthermore, the Au@CdS nanorods demonstrate an enhanced and plasmon-governed two-photon luminescence under near-infrared pulsed laser excitation. This approach has the potential to be used for the preparation of other metal–semiconductor hetero-nanomaterials with complete core–shell structures, and these Au@CdS nanorods may open up intriguing new possibilities at the interface of optics and electronics.

Dodecylamine (DDA) is often used as a reducing agent in the deposition of gold on the surface of semiconductor nanocrystals in nonpolar organic solvents.[42,44,45,48,49,89] For the procedures that use Brust–Schiffrin method[102,103] or dodecyldimethylammonium bromide (DDAB)[42] to transfer gold precursors into an organic solvent for the subsequent deposition reaction because the phase transfer agent and the reducing agent are chemically different materials, the obtained nanocomposites would contain surface impurities due to the phase-transfer agent, which could complicate the particle surface and lead to a negative effect on further modifications and applications. The general phase transfer protocol described in the previous section could overcome this issue, in which the dodecylamine used as the phase-transfer agent would also act as the reducing agent for the subsequent reduction of gold precursors in the presence of pre-formed semiconductor nanocrystals. No additional reducing agent would thus be needed. This strategy makes use of the distinctive advantage of dodecylamine as a suitable reducing agent for gold deposition on the surface of semiconductor nanocrystals without its associated problem of impurity contamination, and is generic enough to be applied to the preparation of semiconductor–gold nanocomposites, as demonstrated by a number of typical examples given in this section.

Upon the DDA-assisted transfer of gold ions, we found that both the reaction time and the metal–semiconductor precursor ratio could have an effect on the deposition of gold on the surface of semiconductor nanocrystals, which we illustrated using a CdS–Au composite nanosystem.[145] The effect of prolonging the reaction time on the morphologies of CdS–Au nanocomposites is shown in Fig. 13. The deposition of Au on the surface of CdS nanocrystals was carried out in the presence of excess dodecylamine and with a CdS–Au molar ratio of 1 : 3. After mixing the CdS and $Au^{3+}$ precursors in toluene for 1 min at room temperature, uniform CdS–Au heterogeneous nanocomposites (Fig. 13a) were obtained as the dominant product. Isolated Au nanoparticles were not observed, indicating that Au preferentially nucleates on the existing CdS nanocrystals rather than homogeneously under the experimental conditions. In most of the cases, the nucleation and growth of Au occur at multiple sites on the surface of CdS nanocrystals. The diameter of the deposited Au domain is *ca.* 1.1 nm. For the sample collected at 5 min, as displayed in the TEM image in Fig. 13b, an increase in the number and size of Au dots on each CdS nanocrystal is observed. As the time increases, the average size of the Au dots reaches *ca.* 2.4 nm at 10 min, with no apparent change compared to the dot size at 5 min. However, the number of Au dots on the surface of each CdS nanocrystal continues to increase, as evidenced by the TEM image in Fig. 13c. When the reaction time was increased to 30 min, the TEM image of CdS–Au nanocomposites in Fig. 13d is almost the same as the previous one (Fig. 13c), indicating that the deposition of Au on the surface of CdS nanocrystals could be completed in 30 min.

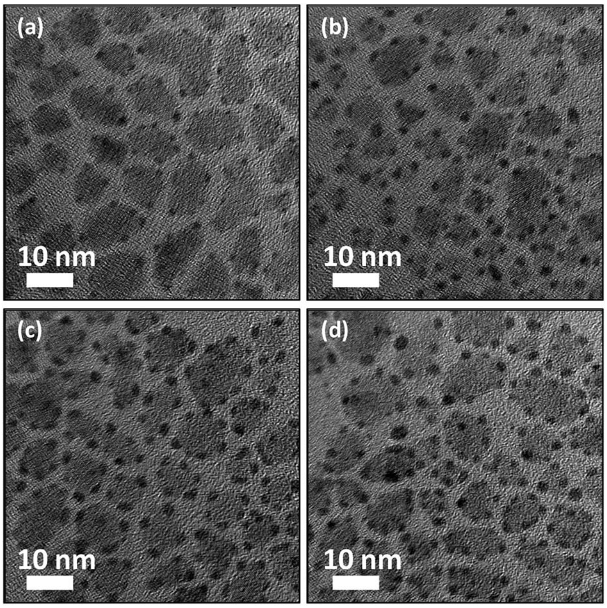

Fig. 13 TEM images of CdS–Au nanocomposites synthesized after physically mixing CdS nanocrystals and $Au^{3+}$ precursors in toluene for 1 min (a), 5 min (b), 10 min (c), and 30 min (d). Reproduced from ref. 145 with permission from the Royal Society of Chemistry.

The effect of the CdS–Au precursor ratio on the morphologies of the CdS–Au nanocomposites is shown in Fig. 14. When the growth was conducted at a high CdS–Au molar ratio (*i.e.*, 9 : 1), CdS–Au heterogeneous nanocomposites with tiny Au dots of approximately 0.8 nm diameter at multiple sites on the surface of CdS nanocrystals were observed under TEM and HRTEM, as shown by Fig. 14a and b. With decrease in the molar ratio of CdS–Au (*i.e.*, a relatively higher ratio of gold in the CdS–Au nanocomposites), analogous to the time-dependent growth of Au dots on the surface of CdS nanocrystals, both the number and size of the Au domains on each CdS nanocrystal were clearly increased, as demonstrated by the TEM and HRTEM images in Fig. 14c–f. When the molar ratio of CdS–Au was reduced to 1 : 6, the growth of Au on the surface of the CdS nanocrystals significantly changed. As shown by the TEM and HRTEM image in Fig. 14i and j, although the average size of the Au dots continuously increased to approximately 3.2 nm, the number of Au domains on the surface of each CdS nanocrystal was clearly reduced compared with that at the CdS–Au ratio of 1 : 3 (Fig. 14g and h). The low CdS–Au ratio inducing an intriguing reduction of the Au dot numbers on the surface of CdS nanocrystals could be considered analogous to the work reported by Banin and co-workers,[80] in which the two-sided growth of Au tips on CdSe quantum dots or rods was transformed into a one-sided growth at a relatively lower CdSe–Au molar ratio *via* an electrochemical ripening process. Similarly, the experimental

This journal is © The Royal Society of Chemistry 2015

Published on 05 December 2014. Downloaded by Library for Natural Sciences of the RAS on 23/03/2015 11:48:51.

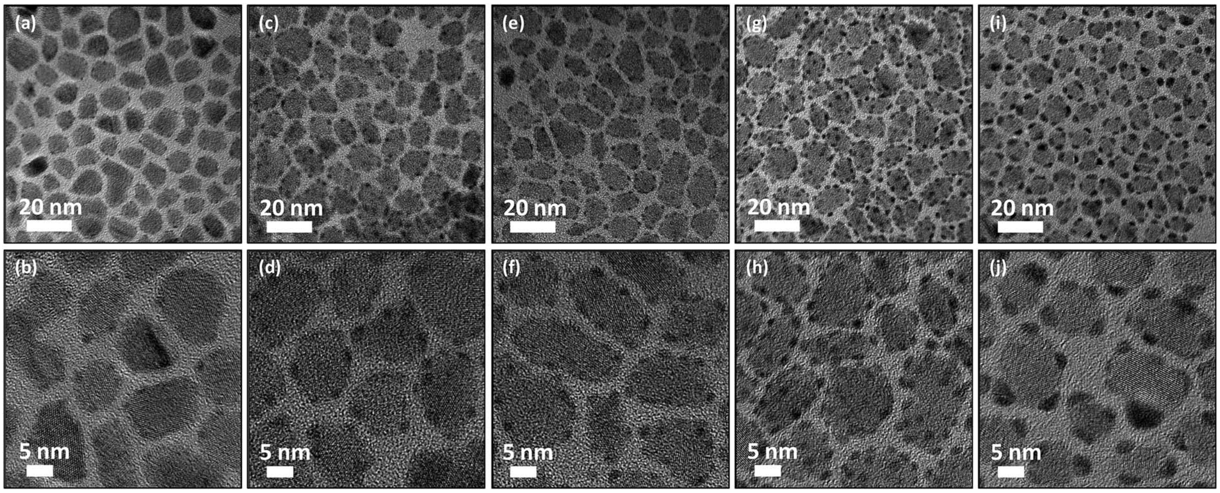

Fig. 14 TEM (a, c, e, g, and i) and HRTEM images (b, d, f, h, and j) of CdS–Au nanocomposites at CdS/Au molar ratio of 9 : 1 (a and b), 3 : 1 (c and d), 1 : 1 (e and f), 1 : 3 (g and h), and 1 : 6 (i and j), respectively. Reproduced from ref. 145 with permission from the Royal Society of Chemistry.

phenomena observed could be interpreted by a more common Ostwald ripening process, which is a phenomenon in which particles larger than a certain critical size grow at the expense of smaller particles due to their relative stabilization by the surface energy term.[146] At a high molar ratio of CdS–Au, the gold nucleates and grows at multiple sites on the surface of CdS nanocrystals. With an increase in the Au molar ratio during the synthesis, Ostwald ripening occurs when the size of the Au domains reaches a critical size, as described in common Ostwald ripening theories.[147] Upon its completion, each composite particle contains several larger gold dots, resulting in a decrease in the number of Au domains.

The deposition of Au on the surface of different metal sulfide nanocrystals has also been investigated. The nanocomposites obtained are illustrated in Fig. 15, in which the deposition of Au on the surface of different semiconducting metal sulfide nanocrystals can be clearly identified through the brightness contrast in the TEM and HRTEM images. Fig. 15 shows that gold is deposited only at a single site on each $Ag_2S$ nanocrystal, whereas it is deposited at multiple sites on each nanocrystal of the other metal sulfides (*i.e.*, CuS, CdS, and PbS). An extreme case is observed with the HgS–Au system (Fig. 15i and j), where numerous sites are available for the nucleation of Au nanoparticles, which could grow and eventually coalesce to form a continuous Au shell on each HgS nanocrystal. The observed species-dependent features for Au deposition on semiconductor nanocrystals have been attributed to the crystal structure of the starting metal sulfide nanocrystals. It might be speculated that the number of sites for Au deposition on the surface of metal sulfide nanocrystals increases with the increase in the structural similarity between Au and semiconductor substrates. For $Ag_2S$ nanocrystals, which provide a single site for Au deposition (Fig. 15a and b), its monoclinic structure is significantly different from that of the face-centered cubic Au particle.

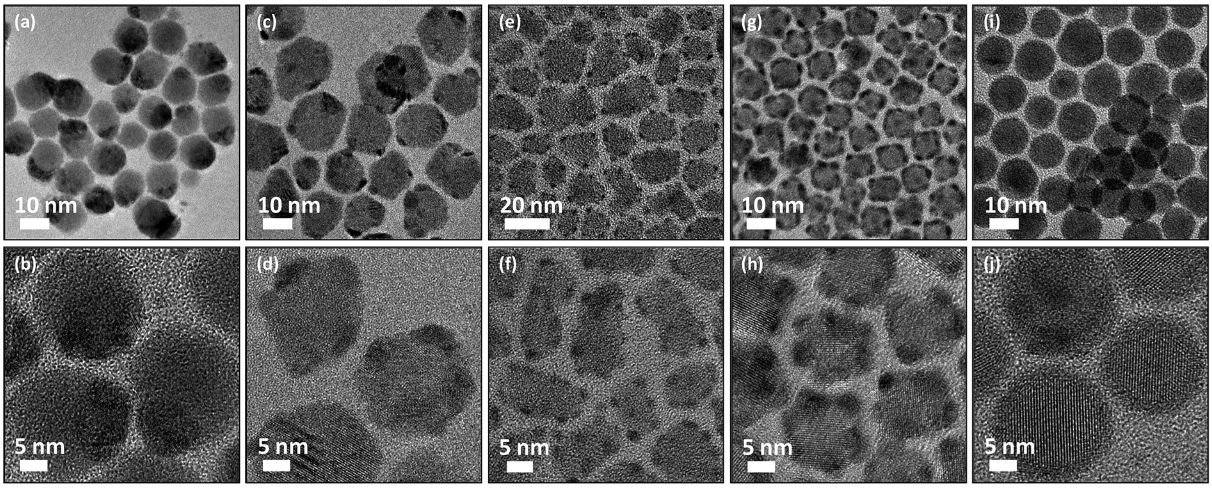

Fig. 15 TEM (a, c, e, g, and i) and HRTEM images (b, d, f, h, and j) of $Ag_2S$–Au (a and b), CuS–Au (c and d), CdS–Au (e and f), PbS–Au (g and h), and HgS–Au nanocomposites (i and j), respectively. Reproduced from ref. 145 with permission from the Royal Society of Chemistry.

Published on 05 December 2014. Downloaded by Library for Natural Sciences of the RAS on 23/03/2015 11:48:51.

Hexagonal CuS and face-centered cubic Au also have distinct differences in their crystal structure, while only two or three sites for Au deposition are observed on the surface of each CuS nanocrystal (Fig. 15c and d). For cubic CdS, PbS, and HgS nanocrystals with structures more analogous to that of the face-centered cubic Au particles, multiple Au domains, and even continuous Au shells, are formed on their surfaces, as evidenced by the other TEM images in Fig. 15.

### 3.2 Deposition of other noble metals on the surface of semiconductor nanocrystals

Motivated by their unique properties and great potential in a wide variety of applications, the syntheses of nanocomposites consisting of semiconductor and noble metals other than gold have also attracted significant attention in recent years.[46,47,148] Actually, early in the 1980s, researchers had loaded platinum (Pt) or Rhodium (Rh) on the surface of CdS or ZnS semiconductors for producing hydrogen.[149–151] However, the overall size of the semiconductor substrates in those reports exceeded the scope of nanotechnology.

Alivisatos' group conducted a pioneering study on the photodeposition of Pt on the surface of CdS and CdSe–CdS nanocrystals.[148] Different from the previously studied aqueous-based deposition of Pt on the surface of semiconductors using a photoreduction approach, they performed the deposition reaction in an organic phase, which included CdS nanorods, an organic soluble Pt precursor, (1,5-cyclooctadiene)dimethylplatinum(II) ($(CH_3)_2PtCOD$), and an excess of a tertiary amine (such as TEA or diisopropylethylamine (DIPEA)), which was used as a hole-scavenging agent. An excitation wavelength of 458 nm was chosen by the researchers to ensure that CdS was the only light-absorbing component; thus, preventing a homogeneous nucleation of platinum. After irradiating the reaction mixture for a while under an inert atmosphere, the solution turned from translucent yellow to translucent brown, and the fluorescence of CdS was quenched. TEM images before and after the irradiation showed the formation of heterostructures consisting of small nanoparticles positioned along the length of the CdS nanorods (Fig. 16). The average diameters of the nanoparticles ranged from 1.5 to 2.7 nm, depending on the reaction conditions. The results obtained by Alivisatos's group are in contrast to CdSe–Au heterostructures synthesized by thermal methods, where the gold deposition often preferentially occurs on the nanorod ends.[42,83] The authors also found that the photodeposition of Pt on CdS shows a strong dependence on the nature of the amine used. The highest yields were observed with bulky tertiary amines such as DIPEA or TEA. A comparison with octylamine, dioctylamine, and trioctylamine revealed no photodeposition for the primary amine, very little for the secondary, and the most for trioctylamine.

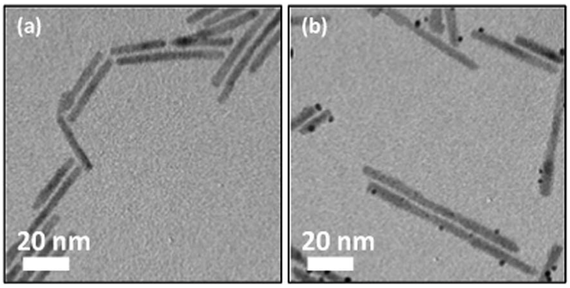

Fig. 16 Photodeposition of Pt on CdS nanorods. (a) TEM images of CdS nanorods before irradiation and (b) the photodeposition product. After exposure to light, Pt nanoparticles appear along the length of the nanorods. Reproduced from ref. 148 with permission from Wiley-VCH.

Subsequently, Banin's group reported the synthesis of rod-like CdSe–Pt nanocomposites and their photocatalytic property toward methylene blue.[46] They produced CdSe nanorods (70 × 8 nm$^2$) using a previously established method.[136,152] After synthesis, the CdSe nanorods were transferred to an aqueous solution by exchanging the alkylphosphine surface ligands with mercapto-undecanoic acid (MUA).[66] The deposition of Pt on the surface of CdSe nanorods could be achieved through a facile route. The platinum precursor ($PtCl_4$) was dissolved in water and vigorously mixed with the aqueous CdSe nanorod solution at room temperature for 2 days. A dark brown/black precipitate was formed and collected by centrifugation to yield the CdSe–Pt composite particles, which are displayed by the microscopic images in Fig. 17. No additional reducing agent was added during the deposition process. A comparison between the TEM images of the samples taken before and after the reaction with platinum showed that the mean length of CdSe nanorods was reduced from 70 nm to 55 nm. Comparing the electrochemical potentials,[153] two ions of $Se^{2-}$ from CdSe nanorods can reduce $Pt^{4+}$ to Pt(0) and form Se(0); thus, the nanorods evolve into

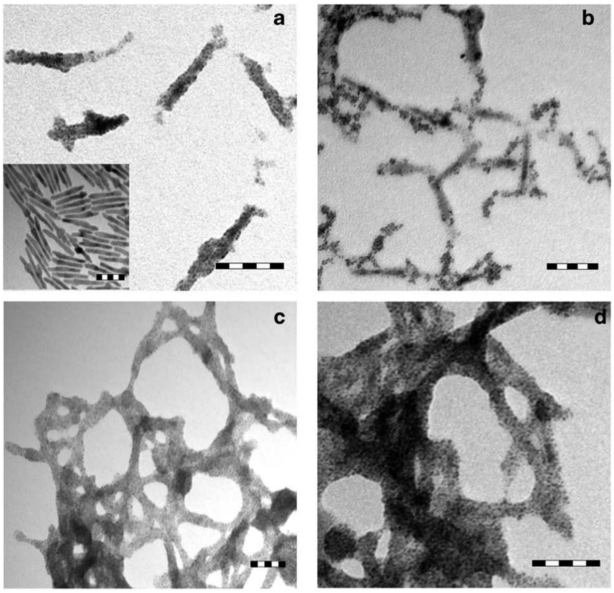

Fig. 17 (a–d) Transmission electron microscopy images of Pt growth on CdSe nanorods in aqueous solutions under different pH conditions (scale bars: 50 nm). (a) Isolated nanorods after Pt growth at pH 10. The inset shows the original rod sample with dimensions of 70 nm × 8 nm. (b) An intermediate state is obtained at pH 7. (c and d) pH 4 produces a nanonet structure in which Pt grows along the rod surface. Reproduced from ref. 46 with permission from Wiley-VCH.

This journal is © The Royal Society of Chemistry 2015

Published on 05 December 2014. Downloaded by Library for Natural Sciences of the RAS on 23/03/2015 11:48:51.

shorter structures while Pt dots grow. A similar effect has been previously observed in the case of gold growth on a CdTe–CdS–CdTe rod system.[154]

The above-mentioned method developed by Banin's group for the growth of Pt on the surface of CdSe nanorods is very complex and time consuming. More importantly, although the rod-like CdSe–Pt nanocomposites they prepared have superior visible light photocatalytic activity for the reduction of methylene blue, the nanocomposites are easily aggregated in aqueous phase, as shown in Fig. 17c and d, and this leads to a significant decrease in the surface area available for the photocatalytic reduction of methylene blue. However, the authors applied a phase transfer to avoid the use of expensive organic metal precursors for producing the semiconductor–noble metal nanocomposites in the aqueous phase, and thus this method offers a good strategy to deposit noble metals on the surface of semiconductor nanocrystals.

Mokari and co-workers prepared CdS nanorods in an organic solvent, but they did not transfer them into the aqueous phase; instead, they directly deposited Pt on the surface of CdS nanorods in diphenyl ether at an elevated temperature using platinum acetylacetonate ($Pt(acac)_2$) as the metal precursor.[47] Analogous to the deposition of Au on the CdSe nanorods, as reported by Banin and coworkes,[42] upon increasing the concentration of a Pt precursor, Pt was also selectively grown at one or two tips of the CdS nanorods because the reactivity of the nanorods is higher at the tips than along the body of the rod due to the increased surface energy, as shown in Fig. 18. The method developed by Mokari and coworkers could be easily extended to deposit bimetallic PtNi or PtCo on the tips of CdS nanorods, and the resulting heterostructures could be of special interest for a variety of applications, including photocatalysis, water splitting, and magnetic applications.

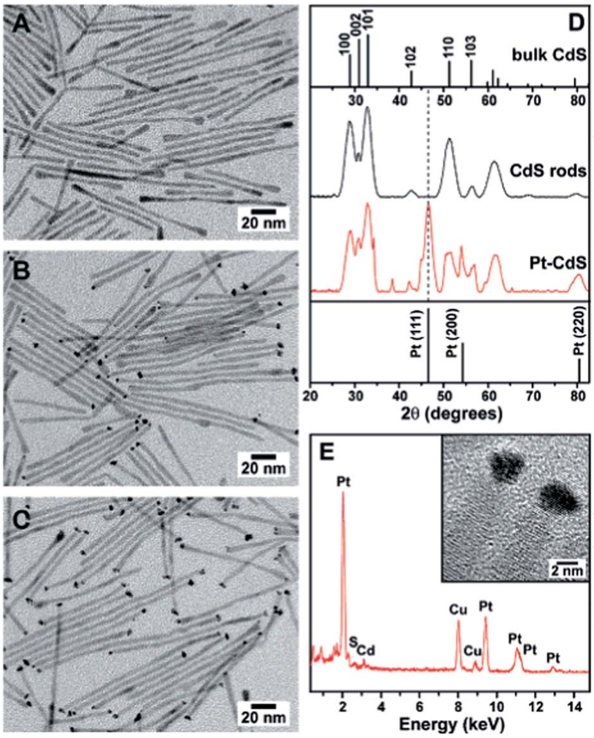

Fig. 18 Selective growth of Pt nanoparticles with different sizes on CdS nanorods, (A) CdS rods (120 nm × 4 nm), (B) CdS with small single Pt tips (4.3 nm), (C) CdS with larger double Pt tips (5.7 nm), (D) XRD patterns of CdS rods and Pt–CdS hybrid structures with corresponding CdS and Pt bulk patterns (the stick patterns shown above and below, respectively), and (E) selected area EDS spectrum of a single Pt tip, with the inset showing an HRTEM image of two Pt–CdS hybrids. Reproduced from ref. 47 with permission from the American Chemical Society.

## 4 Nanocomposites consisting of silver sulfide ($Ag_2S$) and noble metals

As discussed in the previous section, the deposition of noble metals on the surface of semiconductor nanocrystals is usually conducted in nonpolar organic solvents *via* a seed-mediated growth method. Nevertheless, the noble metals are only limited to gold (Au), silver (Ag), and platinum (Pt)[47,48,51,54,66,72,80,83–85,89,90,118–120,133,148] due to the lack of noble metal precursors soluble in nonpolar organic solvents. The general phase transfer protocol described in the previous section could enable a wider variety of metal precursors to transfer from the aqueous phase to nonpolar organic media. However, besides Au and Ag, the other metals cannot be successfully deposited on the surface of semiconductor nanocrystals after phase transfer due to the lack of a suitable reducing agent. In addition, the specific applications of nanocomposites (*e.g.*, photocatalysis) are often carried out in aqueous systems. This makes the aqueous synthesis of nanocomposites an important aspect for the wide-ranging application of composite nanomaterials. Therefore, in this section, we aim to summarize the aqueous route for the synthesis of nanocomposites consisting of $Ag_2S$ and different noble metals. By reducing various noble metal precursors using citrate in an aqueous phase in the presence of preformed $Ag_2S$ nanocrystals, uniform semiconductor–noble metal heterogeneous nanostructures are obtained as the dominant product. In addition to binary nanocomposites, ternary and quaternary hybrid systems can also be achieved *via* the successive deposition of different noble metals on the surface of $Ag_2S$ nanocrystals. In particular, Pt-containing nanocomposites are found to exhibit superior catalytic activity toward methanol oxidation reaction (MOR), the key reaction in direct methanol fuel cell (DMFC), due to the electronic coupling effect between the ultrafine Pt crystallites and semiconductor domains.

### 4.1 Aqueous synthesis of $Ag_2S$ nanocrystals

Numerous studies have been devoted to the synthesis of $Ag_2S$ nanocrystals in organic media.[100,125,155–159] For example, Zhao's group reported a one-step route to control the organization of semiconductor $Ag_2S$ nanocrystals.[157] In a typical synthetic process, they mixed aqueous $AgNO_3$ solution and the toluene solution of dodecylthiol to form a yellow-colored micellar solution with intensive stirring at room temperature. After 30 min, aqueous $Na_2S$ solution was dropped into the

Published on 05 December 2014. Downloaded by Library for Natural Sciences of the RAS on 23/03/2015 11:48:51.

microemulsion for the formation of $Ag_2S$ nanocrystals, which self-assembled into hexagonal, quasi-orthogonal, and chain-like arrays on the TEM grid. A few studies also report the synthesis of $Ag_2S$ nanocrystals in the aqueous phase, either using a protein[160,161] or a polymeric membrane[162] to passivate the surface of $Ag_2S$ nanocrystals to prevent them from aggregating in the solution. However, their self-assembly and poor quality, in terms of morphology, size, and size distribution, makes them unsuitable substrates for the deposition of noble metals.

Alternatively, Yang and Ying developed a room-temperature method based on the reaction between sodium sulfide ($Na_2S$) and coordinating compounds formed by $Ag^+$ ions and bis(*p*-sulfonatophenyl)phenylphosphane dihydrate dipotassium salt (BSPP) to derive aqueous dispersible $Ag_2S$ nanocrystals.[60] Typically, 600 mg of BSPP was added to 300 mL of an aqueous $AgNO_3$ solution (1 mM) in a 1000 mL beaker. The mixture was stirred for 1 h to form BSPP–$Ag^+$ complexes,[130,163] followed by the prompt addition of 10 mL of aqueous $Na_2S$ solution (50 mM), which resulted in a series of color changes before finally arriving at a brown $Ag_2S$ hydrosol. A TEM image of the as-prepared $Ag_2S$ nanocrystals is shown in Fig. 19a. The nanocrystals were spherical, nearly monodispersed, and had an average size of 7.2 nm. The high-resolution TEM (HRTEM) image (Fig. 19b) illustrates the lattice planes in these nanocrystals, showing an interplanar spacing of ~0.26 nm, which correspond to the $(\bar{1}21)$ planes of monoclinic $Ag_2S$.

### 4.2 Binary and multiple $Ag_2S$–noble metal nanocomposites

$Ag_2S$ nanocrystals could be used as seeds for the formation of nanocomposites with different metals. With sodium citrate as a reducing agent, and under the experimental conditions (aqueous phase and elevated temperature), metals preferentially nucleated on the existing $Ag_2S$ nanocrystals, rather than homogeneously. The TEM images of binary $Ag_2S$–Au, $Ag_2S$–Pt, $Ag_2S$–Os, and $Ag_2S$–Pd nanocomposites are illustrated in Fig. 20a–d, respectively. The deposition of noble metals on the $Ag_2S$ nanocrystals could be clearly identified *via* brightness contrast, and was confirmed by the energy-dispersive X-ray (EDX) analysis of an arbitrary single particle with high-angle annular dark-field scanning transmission electron microscopy (HAADF-STEM).

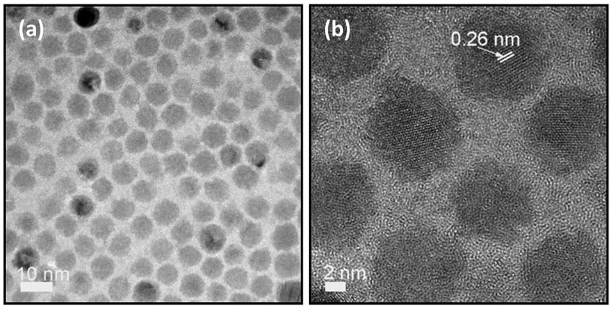

Fig. 19 (a) TEM and (b) HRTEM images of the as-prepared $Ag_2S$ nanocrystals. $\bar{d}$ = 7.2 nm, $\sigma$ = 0.6 nm, $\bar{\sigma}$ = 8.4%. $\sigma$ and $\bar{\sigma}$ are the standard derivation and the relative standard derivation, respectively. Reproduced from ref. 60 with permission from Wiley-VCH.

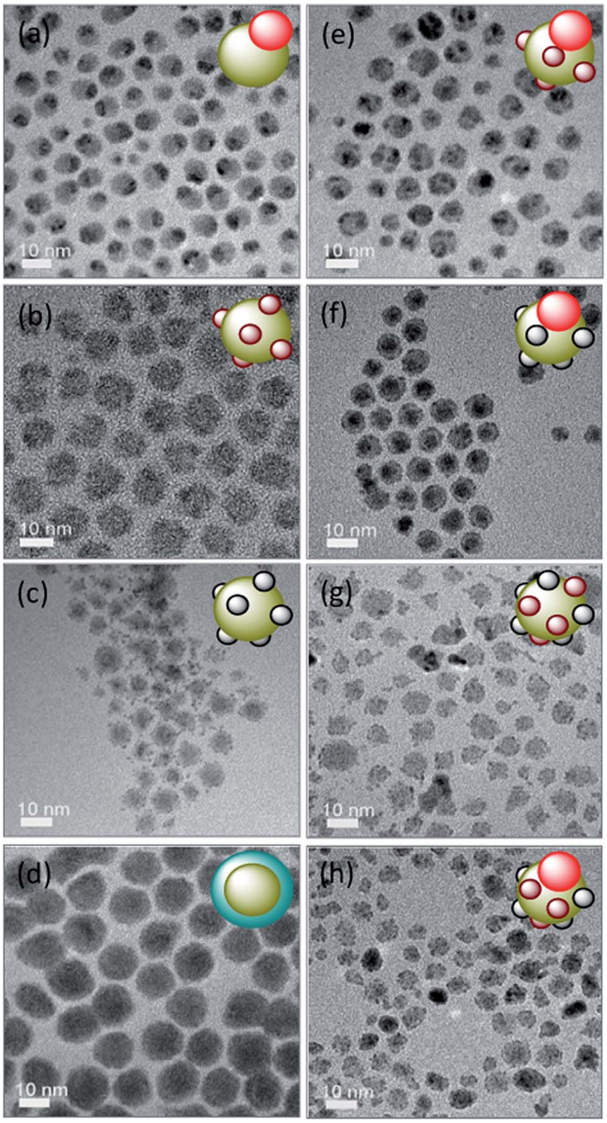

Fig. 20 TEM images of binary $Ag_2S$–Au (a), $Ag_2S$–Pt (b), $Ag_2S$–Os (c), $Ag_2S$–Pd (d), multiple $Ag_2S$–Au–Pt (e), $Ag_2S$–Au–Os (f), $Ag_2S$–Pt–Os (g), and $Ag_2S$–Au–Pt–Os (h) nanocomposites. Reproduced from ref. 60 with permission from Wiley-VCH.

The final morphology of the nanocomposites depended on whether the surface of the substrate particles allowed for only a single nucleation site or multiple ones. Unlike face-centered cubic (fcc) or hexagonal materials, monoclinic $Ag_2S$ has very complicated crystal structures. For instance, it has many facets with different lattice spacings, which provide favorable sites to match the lattice planes of various noble metals for their epitaxial growth on the substrate seeds. The experimental results show that only a single site on $Ag_2S$ nanocrystal surface is suitable for the nucleation of gold clusters; however, multiple sites exist over the surface of $Ag_2S$ seeds for Pt and Os noble metals. An extreme case is observed in the $Ag_2S$–Pd system (Fig. 20d), where numerous sites are provided for the nucleation

This journal is © The Royal Society of Chemistry 2015

Published on 05 December 2014. Downloaded by Library for Natural Sciences of the RAS on 23/03/2015 11:48:51.

of Pd nanoparticles, which could grow and eventually coalesce to form a continuous shell on each $Ag_2S$ nanocrystal.

The species-dependent features of noble metal deposition on $Ag_2S$ nanocrystals could be further employed to derive multiple semiconductor–metal nanocomposites. Complex $Ag_2S$–Au–Pt, $Ag_2S$–Au–Os, $Ag_2S$–Pt–Os and $Ag_2S$–Au–Pt–Os semiconductor–noble metal nanocomposites have been prepared by the successive reduction of noble metal precursors using citrate in the presence of preformed $Ag_2S$ nanocrystals, as characterized by the TEM images in Fig. 20(e–h). The growth of more than one type of metal on each $Ag_2S$ nanocrystal demonstrates that the nucleation sites on the surface of $Ag_2S$ nanocrystals are specific to different metals, which enables the possibility of creating complex nanocomposites between $Ag_2S$ and multiple metals *via* a simple and flexible route.

Pt-containing $Ag_2S$–noble metal nanocomposites are attractive for catalytic applications due to their relative small Pt domain size in the nanocomposite systems. The smaller Pt crystallite size translates to a higher surface area, which is beneficial for catalytic reactions. The electrochemically active surface area (ECSA) of Pt in Pt-containing $Ag_2S$–noble metal nanocomposites was determined using cyclic voltammetry. Although the coherent interfaces between Pt and $Ag_2S$ in the nanocomposites resulted in some blockage of the surface area of the Pt domains, the ECSA of the Pt in Pt-containing $Ag_2S$–metal nanocomposites averaged 84.5 $m^2\ g^{-1}$, which was 16% higher than that of commercial Pt/C (72.9 $m^2\ g^{-1}$) due to the smaller Pt domain size of the former ($\sim$1 nm).

### 4.3 Electrochemical properties of Pt-containing $Ag_2S$–noble metal nanocomposites

The other important feature of the nanocomposites is the electronic coupling between the metal and semiconductor domains. X-ray photoelectron spectroscopy (XPS) analyses of the Pt-containing nanocomposites demonstrated that electrons are transferred to Pt from other domains of the nanocomposites due to the intra-particle charge transfer (see Fig. 21 for the energy level diagram). An analogous charge transfer has been observed in the Au@PbS system in which electrons transfer from the PbS shell to the inner Au core results in an n-type to p-type change in hydrazine-treated PbS.[72] The electron transfer from $Ag_2S$ to Pt could also be described by the generation of a hole in the $Ag_2S$ domain. In the presence of Au domain (work function = 5.1 eV),[164,165] the alignment of energy levels in Au and $Ag_2S$ are favorable for an electron transfer from Au to $Ag_2S$ to fill the hole generated by the electron transfer to the Pt domains, further promoting electron transfer from $Ag_2S$ to Pt for the Fermi levels to match at the interface. The electron transfer from other domains to Pt in Pt-containing nanocomposites increases the electron density around the Pt sites, causing a weakening of CO chemisorption, and thus an increase in their electrochemical activity for the methanol oxidation reaction, a key reaction in direct methanol fuel cells.[60]

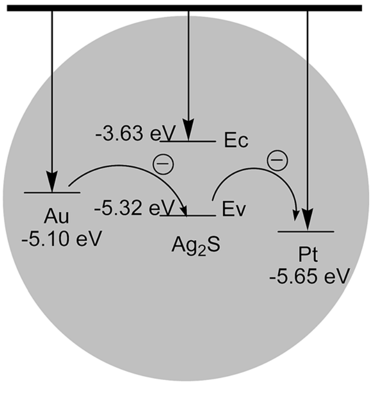

Fig. 21 Energy level diagram for $Ag_2S$–noble metal nanocomposites predicting the intraparticle charge transfer between different domains. Reproduced from ref. 60 with permission from Wiley-VCH.

However, Pt-containing $Ag_2S$–noble metal nanocomposites exhibit poor activity for oxygen reduction reaction (ORR), another key reaction in DMFC.[166–169] This is not surprising based on a report by Watanabe and co-workers,[170] which discussed the alloying of Fe, Ni or Co with Pt to enhance the electro-catalytic activity for oxygen reduction. Fe, Ni and Co have more 5d vacancies than Pt and could withdraw electrons from the latter. This withdrawing effect induces an increase in the 5d vacancies in Pt, increasing 2$\pi$ electron donation from $O_2$ to the Pt surface, and resulting in an enhanced $O_2$ adsorption to favor oxygen reduction. However, for the Pt-containing $Ag_2S$–noble metal nanocomposites, electron donation from the semiconductor to the Pt domains would decrease the 5d vacancies in Pt, and thus the adsorption of $O_2$ on the nanocomposites would be too weak for the $O_2$ dissociation reaction.[171–174] This would account for the poor activity of the Pt-containing nanocomposites towards oxygen reduction.

## 5 Cadmium selenide–platinum nanocomposites with a core–shell construction

The role of surface strain in catalysis, particularly as a means of tuning the catalytic activity, has attracted significant interest in recent years.[175–177] When a metal is deposited on a substrate with different lattice parameters, a compressive or tensile strain in the surface of the metal layer usually occurs to fulfill the requirement of epitaxial growth, and this often affects the overlap of the electron orbitals between the metal atoms, and therefore changes the electronic properties of the surface and its reactivity, which in turn influences the bond strength of an adsorbate.[178,179] Therefore, the application of compressive strain or tensile stain to a surface can be an effective means to influence the surface reactivity.[180] Strain and the associated shift of the d-band can be brought about by growing the desired metal on other materials with a different lattice constant. The overlayer may thus be strained or compressed depending on the lattice mismatch between the two materials. This lateral strain has been studied in a number of pseudomorphic metal monolayers formed on electrode substrates[179,181–184] or core–shell nanoparticles constructed by different metals.[185–187] However, the investigations of lateral strain in semiconductor–metal

Published on 05 December 2014. Downloaded by Library for Natural Sciences of the RAS on 23/03/2015 11:48:51.

nanocomposites, a type of nanostructure that combines materials with distinctly different physical and chemical properties,[42,52,61,68,72,188] have not yet been presented.

Analogous to the deposition of Pd on $Ag_2S$ nanocrystals,[52] we found that in aqueous media, numerous sites on CdSe nanocrystals are also provided for the nucleation of Pt nanoparticles, which then grow and eventually coalesce to form a continuous shell on each CdSe nanocrystal, as displayed by the TEM, HRTEM and STEM images in Fig. 22.[59] The thickness of the Pt shell could be controlled by varying the CdSe–Pt molar ratio in the synthesis. Fig. 22d–f illustrate the core–shell CdSe@Pt nanocomposites synthesized at CdSe–Pt molar ratios of 1 : 1, 2 : 1, and 1 : 2, respectively. The thickness of the Pt shell could be varied, as shown by comparing these figures.

The XRD analyses of the core–shell CdSe@Pt nanocomposites at different CdSe–Pt molar ratios suggest that the interplanar spacing of Pt is compressed to match the lattice plane of CdSe for its epitaxial growth on the CdSe substrates. The compression of Pt lattice spacing can also be verified by the HRTEM images in Fig. 22. Digital analyses of the images show that the spacing of Pt (111) decreases from 0.2244 nm to 0.2148 nm with decrease in Pt molar ratio in the core–shell nanocomposites. The compressive strain effect of the CdSe core on the deposited Pt shell could be an interesting feature for the core–shell composite nanomaterials in a given catalytic reaction.

At a specific CdSe–Pt molar ratio, *e.g.*, 1 : 1, the core–shell CdSe@Pt nanocomposites display superior catalytic activity toward the oxygen reduction reaction (ORR).[59] ORR is the key reaction at the cathode of a direct methanol fuel cell (DMFC),[189–191] and the low activity of the cathode catalysts at room temperature is one of the significant challenges that need to be resolved before the commercialization of DMFCs.[38,174,192] To overcome this problem, it is necessary to maximize the activity of Pt-based catalysts by engineering their structure, morphology and/or composition.

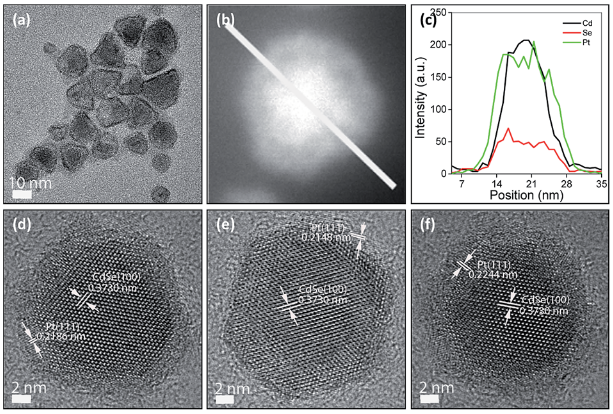

Fig. 22 Core–shell CdSe–Pt nanocomposites synthesized in an aqueous phase using 10 nm CdSe cores: (a) TEM image, (b) STEM image, (c) elemental profile, and (d) HRTEM image of core–shell CdSe–Pt nanocomposites at a CdSe–Pt molar ratio of 1 : 1; (e and f) HRTEM images of core–shell CdSe@Pt nanocomposites at a CdSe–Pt molar ratio of 2 : 1 and 1 : 2, respectively. Reproduced from ref. 59 with permission from the Royal Society of Chemistry.

The observed enhanced catalytic activity for the ORR of core–shell CdSe@Pt nanocomposites could result from the reasonably compressive strain effect of the CdSe core on the Pt shell. It is generally accepted that the common ORR process, *i.e.*, the series 4 electron pathway,[193] must involve both the breaking of an O–O bond and the formation of O–H bonds.[168,173,174] The most active Pt-based catalyst should have a d-band center with an intermediate value because an optimal ORR catalyst needs to facilitate both the bond-breaking and bond-making steps without hindering either one.[171,172] As has been demonstrated,[194] the surface of a Pt-based catalyst with a high d-band center value tends to bind adsorbents more strongly; thus, enhancing the kinetics of the dissociation reactions producing these adsorbents. However, a surface with a lower d-band center value tends to bind adsorbents more weakly and facilitates the formation of bonds between them. The compressive strains of the CdSe core on the Pt shell, leading to a broader d-band, result in a down-shift of the d-band center of the Pt shell. At an appropriate CdSe–Pt molar ratio (*e.g.*, 1 : 1) in core–shell nanocomposites, the downward shift of the d-band center sufficiently balances the bond-breaking and bond-making steps of the ORR process; thus, offering the optimum catalytic activity.

It is worth noting that the core–shell CdSe@Pt nanocomposites also exhibit excellent catalytic activity toward the methanol oxidation reaction (MOR), another key reaction in DMFC,[190,195] at a CdSe–Pt molar ratio of 1 : 2.[59] The enhanced MOR catalytic activity of the core–shell CdSe@Pt nanocomposites could also be attributed to the reasonably compressive strain effect of the CdSe core on the deposited Pt shell, which results in the appropriate shift of the d-band center of the Pt shell and an improvement in the adsorption of methanol on the surface of the Pt catalysts. Interestingly, the CdSe–Pt molar ratio for core–shell CdSe@Pt nanocomposites offering the highest activity for MOR is different from that for ORR. This is an interesting feature for these core–shell nanocomposites for their use in DMFC. Compared with DMFC using Pt/C catalysts both at anode and cathode, the inhibition of methanol crossover to a certain level could be expected when core–shell nanocomposites with the optimal CdSe–Pt molar ratio for ORR are used at cathode. This is important for the commercialization of DMFC because the crossover of methanol from the anode to the cathode through the polymer electrolyte membrane (PEM) would interfere with oxygen reduction at the cathode, resulting in the creation of a mixed potential, and leading to a drastic decrease in the DMFC performance.[196–198]

## 6 Nanocomposites of silver sulfide and noble metals with a controlled nanostructure

These nanostructured composites are attracting interests due to the possibility of integrating materials with vastly different physical and chemical properties into a hybrid nanosystem with a multiplexing capability and tunable physical and chemical properties that may not be obtainable otherwise.[62,63,199–201] The

This journal is © The Royal Society of Chemistry 2015

Published on 05 December 2014. Downloaded by Library for Natural Sciences of the RAS on 23/03/2015 11:48:51.

interactions between the nanoscale metal and semiconductor components, when synergistic, can lead to significant improvements in application performance. In addition, noble metal nanoparticles with controlled internal structures have been used to modify the noble metal properties in a diverse range of applications such as catalysis,[21,202,203] nanoreactors,[204] and in drug delivery systems.[205–207] For example, Pt nanoparticles with a hollow interior are twice as active as solid Pt nanospheres of roughly the same size for methanol oxidation.[98,208] Hyeon and co-workers also reported good catalytic activity for Pd nanoparticles with a hollow interior in Suzuki cross-coupling reactions. Here, the hollow Pd nanoparticle catalyst could be reused seven times without the loss of catalytic activity.[21] The increase of activity in these examples could easily be attributed to the large surface area of the hollow structure, and the internal surface of the catalyst being made accessible to the reactants through the porosity in the shell.

Therefore, the integration of semiconductor and noble metal nanoparticles into a nanosystem with a controlled architecture may lead to further improvements of the application performance of noble metal–semiconductor hybrid materials. In this section, we introduce the research developments in fabricating nanocomposites of silver sulfide and noble metal nanoparticles with an overall hollow or cage-bell structure. The synthetic approach is based on a unique diffusion phenomenon of Ag in core–shell nanoparticles with Ag residing in the core or in an internal shell region. In this strategy, core–shell nanoparticles with Ag residing in the core or inner shell region are first prepared as starting templates. Sulfur is then used to promote the inside-out diffusion of Ag from the core or the inner shell region of the core–shell nanoparticles, and to convert the diffused Ag into $Ag_2S$. The overall result is the conversion of the Ag-containing core–shell nanoparticles into silver sulfide–noble metal nanoparticles with hollow or cage-bell structures.

### 6.1 Inside-out diffusion of Ag in Ag-containing core–shell metal nanoparticles

The inside-out diffusion of Ag in Ag-containing single or double shell core–shell metal nanoparticles is the basis for the synthesis of nanocomposites consisting of $Ag_2S$ and noble metals nanoparticles with controlled structures.[209,210] Typically, core–shell Ag–Pt nanoparticles have been used to illustrate this interesting diffusion phenomenon. The transmission electron microscopy (TEM) images in Fig. 23a and b show the initial uniform core–shell Ag–Pt nanoparticles. After storage in toluene for seven months at room temperature, Ag diffuses out from the interior of the core–shell Ag–Pt nanoparticles and the TEM images show a product very different from the original nanoparticles (Fig. 23c and a). There is an increasing presence of isolated Ag nanoparticles and hollow Pt nanoparticles in a mixture of nanoparticles. The high-resolution TEM (HRTEM) image of Fig. 23d reveals the structures of the isolated Ag and hollow Pt nanoparticles in which two different sets of lattice fringes with separations of 0.236 nm and 0.228 nm, corresponding to the (111) planes of face-centered cubic (fcc) Ag and Pt, are found in the solid and hollow nanoparticles, respectively.

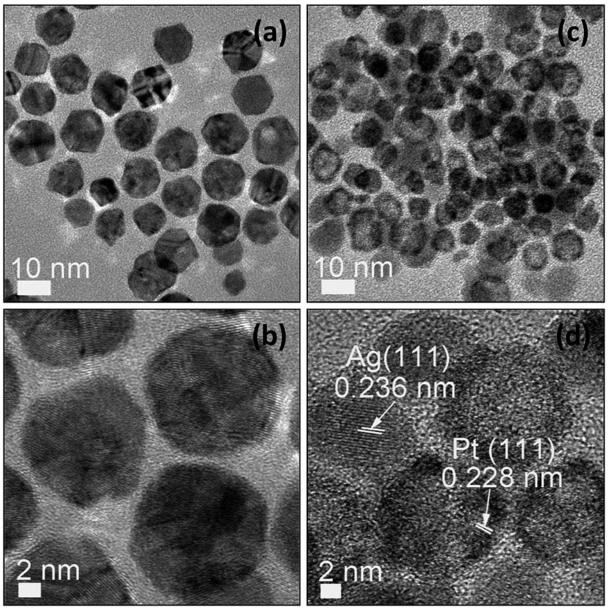

Fig. 23 Inside-out diffusion of Ag in core–shell Ag–Pt nanoparticles. (a) TEM and (b) HRTEM images of the original core–shell Ag–Pt nanoparticles; (c) TEM and (d) HRTEM images of the core–shell Ag–Pt nanoparticles after aging in toluene for seven months at room temperature. Reproduced from ref. 209 with permission from the American Chemical Society.

The inside-out diffusion of Ag is promoted by the multiple-twinned structure of the Ag seeds, which has a strong influence on the stability of the Ag nanoparticles and the overlaid Pt shell. These imperfections in the Ag seed nanoparticles are disruptive to the epitaxial deposition of Pt atoms on the Ag seeds, resulting in a roughness and discontinuity in the subsequently formed Pt shell. The twinned Ag nanoparticles are also inherently unstable and could slowly be etched by dissolved $O_2$ and by $Cl^-$ dissociated from the Pt precursor. Because of the concentration gradient between the interior of the core–shell particles and the surrounding solution, the $Ag^+$ ions generated from the $O_2/Cl^-$ etching of twinned Ag seeds diffuse out through the discontinuous Pt shell, and are reduced by oleylamine to form isolated single crystalline Ag nanoparticles in the colloidal solution. Over time, the core–shell Ag–Pt nanoparticles would eventually disappear due to the etching and outward diffusion of Ag to leave behind a physical mixture of hollow Pt nanoparticles and single crystalline Ag nanoparticles.

### 6.2 Nanocomposites consisting of $Ag_2S$ and noble metal nanoparticles with hollow or cage-bell structures

This inside-out diffusion of Ag in core–shell nanoparticles has been developed into a general protocol for the fabrication of noble metal nanoparticles with a hollow or cage-bell structure.[209] The protocol begins with the synthesis of core–shell Ag–M or core–shell–shell $M_A$–Ag–$M_B$ nanoparticles in an organic solvent. Ag is then removed from the core or from the inner shell by bis(*p*-sulfonatophenyl)phenylphosphane (BSPP), which binds strongly with $Ag^+$ ions to promote the inside-out diffusion

Published on 05 December 2014. Downloaded by Library for Natural Sciences of the RAS on 23/03/2015 11:48:51.

process and to allow the complete removal of Ag in 24–48 hours, leaving behind an organosol of hollow– or cage-bell-structured metal nanomaterials.

Subsequently, Yang's group found a more cost-effective alternative to produce hollow/cage-bell–structured metal nanomaterials, and they employed elemental sulfur (S) to replace expensive BSPP to remove the Ag component from the core–shell particles. However, they experimentally found that the inside-out diffusion of Ag in core–shell nanoparticles could be further developed as a general protocol to fabricate nanocomposites of $Ag_2S$ and metal nanoparticles with a hollow or cage-bell structure.[210] As illustrated by the scheme in Fig. 24, after mixing the core–shell nanoparticles and sulfur in toluene, the $Ag^+$ ions released by the $O_2/Cl^-$ etching of the twinned Ag seeds diffuse out through the discontinuous metal shell, and react with sulfur to form $Ag_2S$ nanocrystals decorated on the outer shell of the metal nanoparticles (Fig. 24a). The $Ag_2S$ nanocrystals grow with the continued outward diffusion of $Ag^+$ ions until the Ag core is completely removed, leaving behind a colloidal solution of nanocomposites consisting of $Ag_2S$ and metal nanoparticles with a hollow interior (Fig. 24b). Finally, the $Ag_2S$ nanocrystals on the surface of the metal shell undergo a ripening process, *e.g.*, Ostwald ripening,[146] to form larger and more stable domains on the surface of the metal shell (see Fig. 24c).

With a slight modification, the abovementioned protocol could also be used to prepare nanocomposites of $Ag_2S$ and noble metal nanoparticles with a cage-bell structure. As a typical example, the core–shell–shell Au–Ag–Pt nanoparticles are first prepared, and after treatment with elemental sulfur, the internal Ag shell is removed from the core–shell–shell Au–Ag–Pt nanoparticles by the aforementioned inside-out diffusion of $Ag^+$ ions. The reaction of $Ag^+$ ions with the sulfur results in the formation of $Ag_2S$ patches on the surface of the as-prepared cage-bell Au–Pt nanoparticles; thus, finalizing the fabrication of the nanocomposites of $Ag_2S$ and Au–Pt nanoparticles with a cage-bell structure. The morphologies of the starting core–shell–shell Au–Ag–Pt nanoparticles and the final nanocomposite are shown by the TEM images in Fig 25a and b. The cage-bell structure of the metallic domains is revealed by the appearance of the void space between the core and the outer shell regions. The void space is formed by the removal of the Ag inner shell by elemental sulfur. The $Ag_2S$ patches on the surface of the cage-bell metal domains display a stronger contrast than the void space, as can be seen in the TEM image in Fig. 25b. The HRTEM image in Fig. 25c of a single composite $Ag_2S$–cage-bell Au–Pt nanoparticle shows three different sets of lattice fringes, with separations of 0.26 nm in the light patches, 0.24 nm in the core, and 0.23 nm in the shell region. These fringes correspond to the $(\bar{1}21)$ planes of monoclinic $Ag_2S$ and the (111) planes of face-centered cubic Au and Pt, respectively. The TEM characterizations confirm that the size and morphology of the remaining metallic domains in the nanocomposites are virtually unchanged after the treatment with sulfur, suggesting that the diffusion of the Ag from the inner shell of the core–shell–shell nanoparticles did not cause the collapse of the particle geometry.

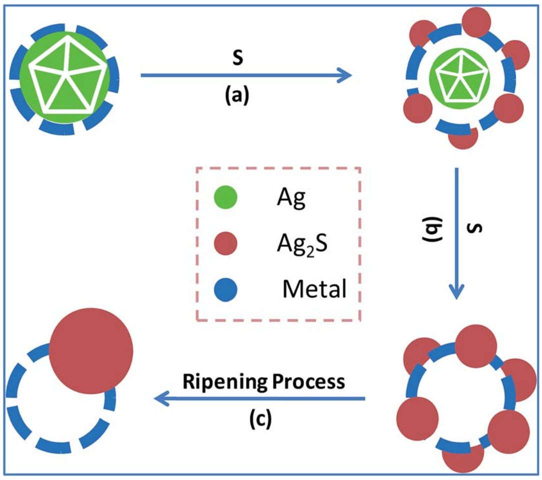

Fig. 24 Schematic illustration showing the formation of nanocomposites consisting of $Ag_2S$ and metal nanoparticles with a hollow interior based on the inside-out diffusion of $Ag^+$ in Ag-containing core–shell nanoparticles. Reproduced from ref. 210 with permission from the Royal Society of Chemistry.

### 6.3 Ternary nanocomposites consisting of $Ag_2S$, Au, and Pt nanoparticles with hollow interiors

The strategy for the fabrication of nanocomposites of $Ag_2S$ and hollow-structured noble metal nanoparticles could be further developed to produce ternary nanocomposites

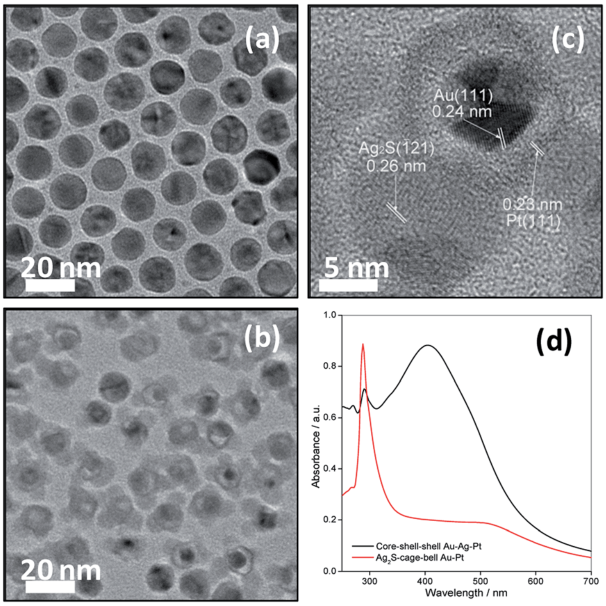

Fig. 25 TEM images of core–shell–shell Au–Ag–Pt (a), $Ag_2S$–cage-bell Au–Pt (b); HRTEM images of the nanocomposites of $Ag_2S$–cage-bell Au–Pt (c); UV-visible spectra of core–shell–shell Au–Ag–Pt nanoparticles before and after treatment with elemental sulfur (d). Reproduced from ref. 210 with permission from the Royal Society of Chemistry.

This journal is © The Royal Society of Chemistry 2015

Published on 05 December 2014. Downloaded by Library for Natural Sciences of the RAS on 23/03/2015 11:48:51.

consisting of $Ag_2S$, Au, and Pt nanoparticles with hollow interiors, labeled as $Ag_2S$–Au–hPt.[211] In brief, the gold precursors ($HAuCl_4$) were first transferred from an aqueous solution to toluene using the general transfer protocol described in the second section, and then mixed with the $Ag_2S$–hollow Pt ($Ag_2S$–hPt) nanocomposite organosol in toluene. Ternary $Ag_2S$–Au–hPt nanocomposites are found as the dominant product after aging the mixture of $Ag_2S$–hPt hetero-dimers and $HAuCl_4$ in toluene for 2 h, as indicated by the TEM and HRTEM images in Fig. 26. The isolated Au nanoparticles were not observed, indicating that Au preferentially nucleates on the existing $Ag_2S$–hPt heterodimers under the experimental conditions. In most of the cases, Au is deposited only at a single site on the $Ag_2S$ domain in each $Ag_2S$–hPt heterodimer. The average diameter of the deposited gold patches is *ca.* 8.3 nm, which is discernible by the strong brightness contrast in the TEM and HRTEM images.

Direct evidence for the formation of ternary $Ag_2S$–Au–hPt nanocomposites is provided by the line scanning analysis and the elemental mapping of an arbitrary single composite nanoparticle (Fig. 26c) in the high-angle annular dark-field STEM mode. As shown in Fig. 26d for the line-scanning analysis, Au and Pt signals are present on the left- and right-hand side, respectively, whereas the Ag and S signals are only concentrated in the core region. The line-scanning analysis is in accordance with the nanoscale mapping results (Fig. 26e–i), which also show that the Au and Pt components are distributed on two different sides of the ternary nanocomposites. Furthermore, the HRTEM image reveals that the crystal planes of Au are not parallel to those of $Ag_2S$ in each heterodimer nanoparticle (Fig. 26b), indicating that the growth of Au on the surface of $Ag_2S$ domain takes place under different orientations.

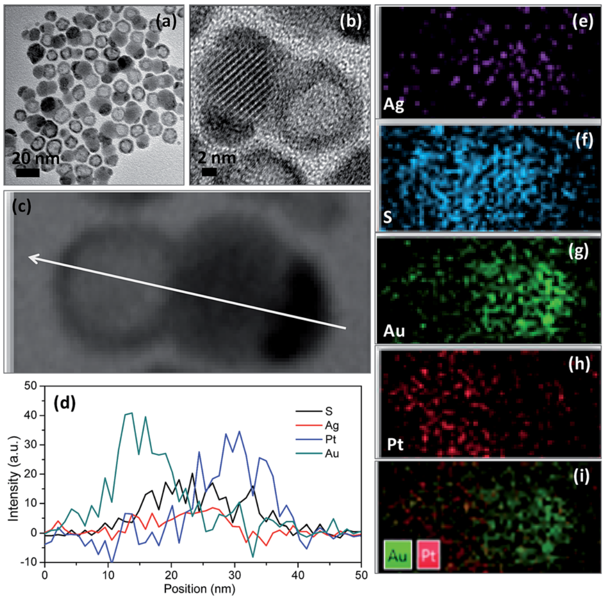

Fig. 26 TEM image (a), HRTEM image (b), STEM image (c), line-scan analysis (d), and elemental mapping (e–i) of a single particle (c) of the ternary $Ag_2S$–Au–hPt nanocomposites as prepared by depositing Au on the $Ag_2S$–hPt heterodimers in toluene at room temperature. Reproduced from ref. 211 with permission from the Nature Publishing Group.

The ternary $Ag_2S$–Au–hPt nanocomposites exhibit an enhanced electrocatalytic property toward the methanol oxidation reaction due to the strong electronic coupling between Pt and other domains in the hybrid particles. This study offers a vivid example of the enhancement of the material properties by the structural tailoring of the nanocomposites, and suggests that the concept might have potential for the design and synthesis of other heteronanostructures for catalytic applications other than methanol oxidation reaction.

## 7 Nanocomposites of metal oxides and noble metals

Heterogeneous nanoparticles consisting of metal oxides and noble metals represent an important type of composite nanomaterial, which often shows improved physical/chemical properties over those of the single-component nanoparticles,[212–214] analogous to the case of semiconductor–noble metal nanocomposites. The enhancement could be attributed to the synergetic effect that occurs at the interface of the noble metal and metal oxide domains in the nanocomposites.[213,215–219] For example, gold is usually a chemically inert metal, but Au nanoparticles deposited on a metal oxide substrate display superior catalytic activity for the oxidation of carbon monoxide (CO).[213,217–224] It is believed that the high activity of metal oxide–Au nanocomposites is induced by a junction effect, which arises from the transfer of electrons from the oxide support to the Fermi level of the adjacent gold domain through the intimate contact between them.[215,225]

As summarized by Sun and coworkers,[226] it is important to study metal oxide–noble metal nanocomposites because each side of the domain in the heterogeneous structure is restricted to the nanometer scale and a small variation in electron transfer across the interface between these two limited electron "nanoreservoirs" can lead to a drastic change in properties for each domain. Therefore, metal oxide–noble metal nanocomposites offer an interesting platform to investigate the physical/chemical properties of materials based not only on each particle dimension and morphology, but also on the communication between the two different domains. Analogous to the hot topics related to semiconductor–noble metal nanocomposites, the primary objectives in the field of metal oxide–noble metal nanocomposites could be categorized as follows: (i) to develop general strategies to prepare metal oxide–noble metal nanocomposites with the control on the size and morphology of each domain in the composite particles; (ii) to understand the synergetic effect and interface boundary sites in metal–metal oxide systems, which are of importance for the enhanced properties of the metal oxide–noble metal nanocomposites, *e.g.*, catalysis; (iii) to explore various applications of the nanocomposites, *e.g.*, as highly active catalysts for energy conversion reactions and as multifunctional probes for target-specific imaging and delivery. In this section, we introduce the recent research progress in the syntheses and applications of metal

Published on 05 December 2014. Downloaded by Library for Natural Sciences of the RAS on 23/03/2015 11:48:51.

oxide–noble metal nanocomposites, particularly highlighting the general strategies used to produce dumbbell-like nanocomposites that contain noble metal and magnetic nanoparticles or quantum dots, and we illustrate the interesting optical and magnetic properties found in these composite particles.

### 7.1 The pioneering work by Haruta *et al.*

The pioneering discovery of Haruta and coworkers on the low-temperature CO oxidation by gold nanoparticles, when supported on appropriate metal oxides, started a new era of research into Au as a catalyst for a plethora of catalytic reactions.[220] The oxidation of CO is an important issue in many industrial, environmental, and domestic sectors of society. The stationary emissions of CO continue to pose problems in many industrial processes that involve combustion and partial oxidation of hydrocarbons. Before Haruta's discovery, the catalysts used for CO oxidation were hopcalite catalysts (mixed oxides mainly composed of Mn and Cu) or noble metals, *e.g.*, platinum or palladium. However, these catalysts, although they have high catalytic activities, are either not water tolerant or are not sufficiently active at ambient temperature nor in the presence of concentrated CO.[227–230] The novel gold catalysts employed by Haruta and coworkers were prepared by co-precipitation from an aqueous solution of chloroauric acid and the nitrate of transition metals. The authors found that the novel catalysts were composed of ultrafine gold particles and one of the oxides of the 3d transition metals of group VIII, namely, Fe, Co, or Ni. Then, they carried out the CO oxidation catalytic activity measurements in a small fixed-bed reactor, and concluded that the highest oxidation activity was achieved using gold combined with $\alpha$-$Fe_2O_3$, $Co_3O_4$, or NiO. The optimum content of gold was found to be 5 atom% with $\alpha$-$Fe_2O_3$ and $Co_3O_4$, or 10 atom% with NiO. Fig. 27 shows the conversion efficiency of CO as a function of duration time at various catalyst temperatures. These gold catalysts are able to completely oxidize CO even at −70 °C, and exhibit remarkably enhanced activity compared to gold powder and the host metal oxides. For instance, when the latter single compounds are used, the oxidation of CO needs considerably higher temperatures, ranging from 100 °C for $Co_3O_4$ to 300 °C for gold powder under the same experimental conditions.

The authors compared the new catalysts with those obtained by an impregnation method. In conventional gold catalysts supported on $\gamma$-$Al_2O_3$ or $\alpha$-$Fe_2O_3$ by impregnation, even when they were calcined at 200 °C, the gold crystallites were considerably larger, *ca.* 20 nm. Indeed, the results for these impregnated catalysts show that such catalysts are active only at temperatures above 100 °C. Therefore, it is clear that co-precipitation leads to a considerably higher dispersion of gold than impregnation. Moreover, the high dispersion of gold brings about the extremely high activity for CO oxidation at temperatures below 0 °C. Furthermore, because the selection of the host oxides is another important factor, the specific interaction of gold particles with the oxides of Fe, Co, and Ni might also be responsible for the remarkable enhancement of oxidation activity, as evidenced in a number of follow-up studies.

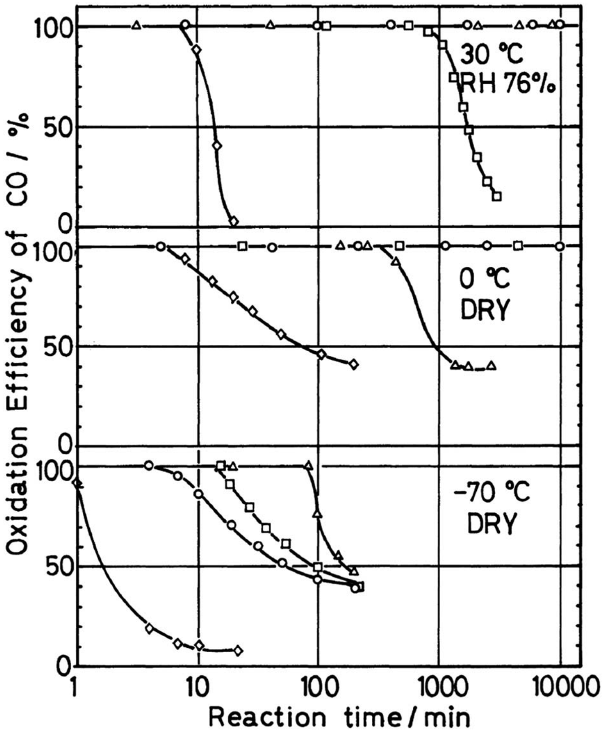

Fig. 27 Oxidation efficiency of CO as a function of duration time. ○ 5 atom% Au/$\alpha$-$Fe_2O_3$; Δ 5 atom% Au/$Co_3O_4$; □ 10 atom% Au/NiO; ◇ hopcalite catalyst; Catalysts 0.20 g, CO 1 vol% air 66 mL $min^{-1}$. Reproduced from ref. 220 with permission from the Chemical Society of Japan.

### 7.2 Early studies in metal oxide–Au nanocomposites

The discovery of the remarkable catalytic activity in the low-temperature oxidation of CO spurred a significant growth in the studies related to metal oxide–gold nanocomposites and metal oxide-supported gold catalysts. Though at early stage, the research in this field emphasizes the importance of catalyst preparation and the effect of different metal oxides on the catalytic activity of deposited gold particles.[217,231–243] In particular, most of the detailed studies have concentrated on $TiO_2$–Au nanocomposites. For example, in their initial work, Haruta *et al.* showed that $\alpha$-$Fe_2O_3$ was active, and subsequently they also showed that Au supported on $TiO_2$ substrates was equally effective for CO oxidation.[221]

It is well established that the deposition precipitation method, in which a previously formed metal oxide support is stirred in a solution of a gold compound and pH value is varied by the addition of a base (*i.e.*, NaOH or urea), could be used to obtain very small gold nanoparticles on the surface of the metal oxide support. The mechanism for the deposition precipitation method in the Au–$TiO_2$ system was studied in great detail by Louis and coworkers.[241] They prepared $TiO_2$–Au composite materials by cation adsorption and deposition–precipitation with urea (DP urea) and NaOH (DP NaOH) and characterized

This journal is © The Royal Society of Chemistry 2015

Published on 05 December 2014. Downloaded by Library for Natural Sciences of the RAS on 23/03/2015 11:48:51.

them by various techniques during the preparation to determine the nature of the species deposited and the chemical phenomena occurring during these preparations. They found that in the case of the cationic adsorption of the $[Au(en)_2]^{3+}$ complex, the preparation has to be performed at room temperature to avoid the decomposition of the complex and reduction of gold. In this way, small gold particles could be obtained after calcination, but the gold loading was low. Both the methods of deposition–precipitation (DP NaOH and DP urea) involve the deposition of a gold(III) species on the $TiO_2$ surface, but the nature of these species is different. For the DP NaOH method, $[AuCl(OH)_3]^-$, the main species present at pH 8 of the preparation, reacts with the hydroxyl groups of the $TiO_2$ surface, and forms a grafted hydroxy-gold compound. This explains the limited amount of gold deposited on $TiO_2$ by this method. For the DP urea method, all the gold present in the solution is deposited on the $TiO_2$ surface as a gold(III) precipitate, which is not gold(III) hydroxide, but an amorphous compound containing nitrogen, oxygen and carbon. This compound is obtained from a reaction between the gold precursor and the products from the decomposition of urea. The metallic gold particles obtained after calcination exhibit a decreasing size as the DP urea method progresses over time. The authors proposed that the progressive increase in the pH, due to the decomposition of urea at 80 °C, results in changes in the surface charge density of the gold precipitate particles, and leads to fragmentation of the particles.

The preparation of Au–$TiO_2$ catalysts by the DP method has been recently studied in detail by Moreau *et al.*[239] They observed that the method involves the close control of many experimental variables, as succinctly summarized by Hashmi and Hutchings as follows:[222]

- The concentration of $HAuCl_4$ solution,
- The ratio of the volume and concentration to the mass of the support,
- The type of $TiO_2$ (Degussa P-25 is the most commonly chosen),
- The base chosen to neutralize the $HAuCl_4$ solution,
- The temperature,
- The pH value, both at the time when $TiO_2$ is added and in the subsequent reaction,
- The time and the temperature allowed for the deposition to occur,
- The method of filtration, washing, and drying,
- The conditions for calcination, if performed,
- The apparent sensitivity of the precursor to light.

Although significant advances in catalyst synthesis and characterization have been achieved, many questions remain concerning the relatively simple CO oxidation reaction; for example, what is the reaction mechanism and what is the nature of the active site? In 2000, Bond and Thompson proposed a model, where Au atoms at the interface between the Au particle and the metal oxide substrate were the active oxidation centers.[244] As schematically illustrated in Fig. 28, they suggested that the peripheral atoms could be cationic gold, and it is these atoms that are responsible for the activation of dioxygen in the catalytic process. Later, Kung *et al.* also used this as the basis for their discussions on the mechanisms.[245] However, it should be noted that although there has been a large number of studies using model systems, a definitive study has not yet been published concerning the relative roles of $Au^0$ and $Au^{n+}$ in the catalytic oxidation of CO.

Goodman and coworkers prepared gold clusters ranging in diameter from 1 to 6 nm on single crystalline surfaces of titania in ultrahigh vacuum to investigate their unusual size dependence for the low-temperature catalytic oxidation of carbon monoxide. They used a combination of scanning tunneling microscopy/spectroscopy (STM/STS) with elevated pressure reaction kinetics measurements to determine whether the unusual reactivity could be due to a quantum size effect in the fine gold particles.[212] The answer was positive, and the authors showed that the structure sensitivity of the CO oxidation reaction on gold clusters supported on titania is related to a quantum size effect with respect to the thickness of the gold islands, and they further found that the islands with two layers of gold are the most effective for catalyzing the oxidation of carbon monoxide. Their results suggest that supported gold clusters, in general, may have unusual catalytic properties as one dimension of the cluster becomes smaller than three atomic spacings.

Later, Chen and Goodman designed well-ordered monolayers and bilayers of gold atoms that completely cover the $TiO_2$ support to address the role played by these peripheral atoms.[213] Their design eliminated the particle shape and direct $TiO_2$ support effects on the catalytic property of gold for CO oxidation. High-resolution electron energy loss spectroscopy and carbon monoxide adsorption confirmed that the gold atoms bonded to the titanium atoms. The authors found that the bilayers were significantly more active than the monolayers; thus, indicating that the catalysis could proceed on the

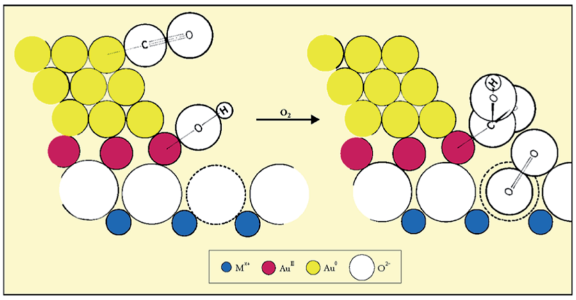

Fig. 28 A representation of the early stages of the oxidation of carbon monoxide at the periphery of an active gold particle. On the left-hand side, a carbon monoxide molecule is chemisorbed on a low coordination number gold atom, and a hydroxyl ion moves from the support to an $Au^{3+}$ ion, creating an anion vacancy. On the right-hand side, they have reacted to form a carboxylate group, and an oxygen molecule occupies the anion vacancy as $O_2^-$; this then oxidizes the carboxylate group by abstracting a hydrogen atom, forming carbon dioxide, and the resulting hydroperoxide ion $HO_2^-$ then oxidizes a further carboxylate species forming another carbon dioxide and restoring the two hydroxyl ions to the support surface. This completes the catalytic cycle. No attempt is made to suggest the charges carried by the reacting species. Reproduced from ref. 244 with permission from Springer.

Published on 05 December 2014. Downloaded by Library for Natural Sciences of the RAS on 23/03/2015 11:48:51.

extended gold surface that was created. Subsequently, Chen and Goodman concluded that the atoms at the periphery in both the model and real catalysts were metallic in nature.[246] However, in these studies, the techniques used could not distinguish between cationic or metallic gold, and consequently an influence of the $TiO_2$ support on the electronic state of the gold could not be ruled out. Indeed the electronic nature of very small gold particles could be expected to be significantly influenced by the nature of the support, especially the availability of defect sites.

Recently, the conclusions drawn from model systems were confirmed by Hutchings and coworkers.[224] They employed aberration-corrected scanning transmission electron microscopy to analyze several iron oxide-supported gold catalyst samples, ranging from those with little or no activity to others with high activity. The authors observed that at higher magnification, the actual Au particle size distribution and morphology in $FeO_x$–Au samples are considerably different. All the samples contained larger (2 to 15 nm) Au particles and a considerable number of individual Au atoms dispersed on the iron oxide surface, as displayed in Fig. 29. They found that the high catalytic activity for carbon monoxide oxidation was correlated with the presence of bilayer clusters that were ~0.5 nm in diameter and contained only *ca.* 10 gold atoms; this result is in accordance with that demonstrated previously with the use of model catalyst systems.

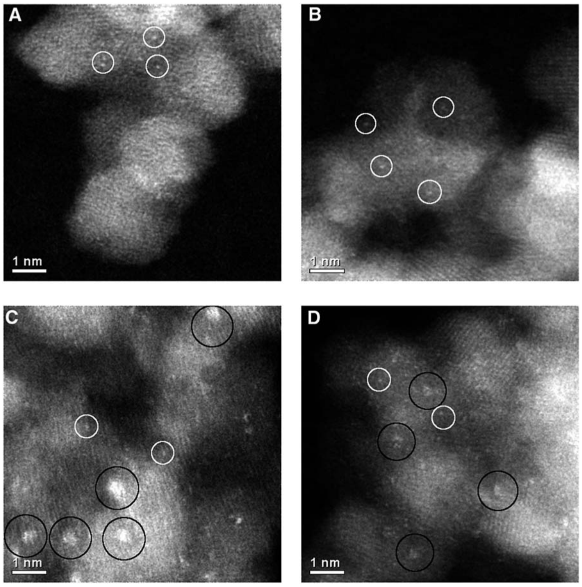

Fig. 29 High-magnification aberration-corrected STEM-HAADF images of (A and B) the inactive and (C and D) the active Au–$FeO_x$ catalysts acquired with the aberration-corrected JEOL 2200FS. The white circles indicate the presence of individual Au atoms, whereas the black circles indicate subnanometer Au clusters consisting of only a few atoms. Note the presence and image intensity difference of the two distinct cluster-types: in (C), there are 0.5 nm higher-contrast clusters, whereas in (D) 0.2–0.3 nm low-contrast clusters dominate. This difference indicates that bilayer and monolayer subnanometer Au clusters are present in the active catalyst. Reproduced from ref. 224 with permission from Science.

### 7.3 Dumbbell-like metal oxide–noble metal nanocomposites

Nanocomposites with two different functional domains sharing an intimate contact are referred to as dumbbell-like structures.[226] The interfacial interactions that originate from electron transfer across the nanometer contact at the interface of the two domains in the nanocomposites can induce new properties that are not present in the individual components. Sun's group at Brown University made a significant contribution in the synthesis and application of nanocomposites consisting of magnetic metal oxides and optical or catalytic noble metals. In contrast to conventional impregnation or deposition–precipitation methods, Sun and coworkers employed a wet-chemistry based approach to generate dumbbell-like nanocomposites consisting of metal oxide and noble metals. The wet-chemistry method, although complicated by many factors, *e.g.*, metal precursors, solvent, surfactants, reducing agent, reaction temperature, and pH value, might offer more space to control and tune the final products in terms of their size, morphology, and structure.[2] As a first example, in 2005, Sun's group demonstrated the synthesis of dumbbell-like Au–$Fe_3O_4$ nanocomposites *via* the decomposition of $Fe(CO)_5$ on the surface of Au nanoparticles, followed by oxidation in 1-octadecene solvent.[87] By varying the experimental conditions, *e.g.*, the seed particle size or the injection mode, the size of the particles could be tuned from 2 to 8 nm for Au and from 4 nm to 20 nm for $Fe_3O_4$ (Fig. 30). The authors found that the nanocontact between Au and $Fe_3O_4$ resulted in a red-shift of the surface plasmon of the Au and slowed the increase in the magnetization of the small $Fe_3O_4$. The dumbbell structure was formed through the epitaxial growth of iron oxide on the Au seeds, and the growth could be affected by the polarity of the solvent because the use of more polar solvent, *e.g.*, diphenyl ether, led to the formation of flower-like Au–$Fe_3O_4$ composite particles. Moreover, Au–$Fe_3O_4$ could be readily converted into Au–$Fe_2O_3$ ($\gamma$-$Fe_2O_3$ or $\alpha$-$Fe_2O_3$), making it possible to use it in the systematic studies of nanoscale interactions and their effects on the physical and chemical properties of the Au–iron oxide nanocomposites.

Moreover, in 2005, Sun and coworkers reported the enhanced magneto-optical response in dumbbell-like Ag–$CoFe_2O_4$ nanocomposites.[88] They first prepared $CoFe_2O_4$ nanoparticles using the method they had established before[247] and further treated the $CoFe_2O_4$ nanoparticles with 1-hexadecanethiol in phenyl ether. Then, the treated $CoFe_2O_4$ nanoparticles were mixed with $AgNO_3$ and tetrahydronaphthalene and heated at 100 °C for 1 h for the formation of dumbbell-like Ag–$CoFe_2O_4$ nanocomposites. The magneto-optical characterization demonstrated that at short wavelengths, the magnitude of the rotation and the shape of the hysteresis loops were considerably comparable for the two types of particles with a common particle concentration, with coercivity values below 50 Oe and with a saturation field of approximately 500 Oe. The authors interpreted this similarity to be originating from the dominant effects of the $CoFe_2O_4$ interband transitions to the magneto-optical tensor (diagonal

Published on 05 December 2014. Downloaded by Library for Natural Sciences of the RAS on 23/03/2015 11:48:51.

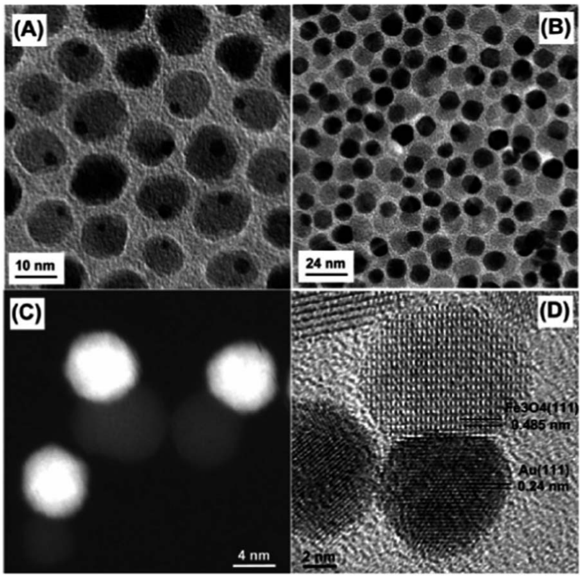

Fig. 30 TEM and STEM images of dumbbell-like Au–$Fe_3O_4$ nanoparticles: (A) TEM image of the 3–14 nm Au–$Fe_3O_4$ particles; (B) TEM image of 8–14 nm Au–$Fe_3O_4$ particles; (C) HAADF-STEM image of 8–9 nm Au–$Fe_3O_4$ particles; and (D) HRTEM image of an 8–12 nm Au–$Fe_3O_4$ particle. The specimens for TEM and STEM analyses were prepared by the room-temperature deposition of the hexane dispersions of the particles on carbon-coated copper grids. Reproduced from ref. 87 with permission from the American Chemical Society.

and off-diagonal terms) in the highly absorptive violet/blue wavelength regime.

While a dramatic contrast was observed between the magneto-optical response for the Ag–$CoFe_2O_4$ dimers and $CoFe_2O_4$ monomers at longer wavelengths, these were outside the $CoFe_2O_4$ interband transition-dominated regime. Although the overall magnitude of the Faraday rotation decreased away from the absorption edge of $CoFe_2O_4$, the rotation became significantly enhanced for the dimers relative to the monomers by nearly an order of magnitude near 633 nm. This approximate wavelength range also corresponds to a "crossover" regime, where the sign of the Faraday effect changes for the monomer nanoparticles, while the dimers remain unaffected in this regard. Sun and coworkers hypothesized that this strong contrast in the spectral behavior was due to the dielectric contribution of the Ag-nanoparticle component in the Ag–$CoFe_2O_4$ dimer. In particular, the crossover behavior for the $CoFe_2O_4$ monomer, which was absent in the dimer case, occurs in the Ag nanoparticle plasmon tail, where the dielectric contribution by Ag to the dimer appears to produce a significant additive contribution to the overall magneto-optical response of the composite nanoparticle Ag–$CoFe_2O_4$ particle pairs.

Magnetically and optically active dumbbell-like nanocomposites containing two different chemical surfaces are particularly suitable for selected nanoparticle functionalization with both targeting agents and drug molecules, which facilitates their application as multifunctional probes for target-specific imaging and delivery.[15] Specifically, dumbbell-like Au–$Fe_3O_4$ nanocomposites contain both Au and $Fe_3O_4$ nanoparticles, which are known to be biocompatible, and have been used extensively for optical and magnetic applications in biomedicine.[249–258] Compared with conventional single-component Au or $Fe_3O_4$ nanoparticles, dumbbell-like Au–$Fe_3O_4$ composite systems have distinct advantages: (i) the structure contains both a magnetic ($Fe_3O_4$) and an optically active plasmonic (Au) unit and is suitable for simultaneous optical and magnetic detection; (ii) the presence of $Fe_3O_4$ and Au surfaces facilitates the attachment of different chemical functionalities for target-specific imaging and delivery applications; and (iii) the size of either of the two nanoparticles can be controlled to optimize the magnetic and optical properties, while the small particle is only capable of accommodating a few DNA strands, proteins, antibodies, or therapeutic molecules; thus, facilitating kinetics studies in cell targeting and drug release. Upon successful synthesis, Sun and coworkers extended their dumbbell-like Au–$Fe_3O_4$ nanocomposites toward their application as dual-functional probes and for target-specific platin delivery.[218,259] By functionalizing the surface of $Fe_3O_4$ and Au domains in dumbbell-like Au–$Fe_3O_4$ nanocomposites with the epidermal growth factor receptor antibody (EGFRA) and HS–PEG–$NH_2$, respectively, the dumbbell-like nanocomposites could remain stable against aggregation in phosphate-buffered saline (PBS) or PBS containing 10% fetal bovine serum (FBS) at 37 °C for 12 h.[248] In addition, the magnetic and optical studies revealed that the dumbbell-like nanocomposites were both magnetically and optically active and could be used as dual

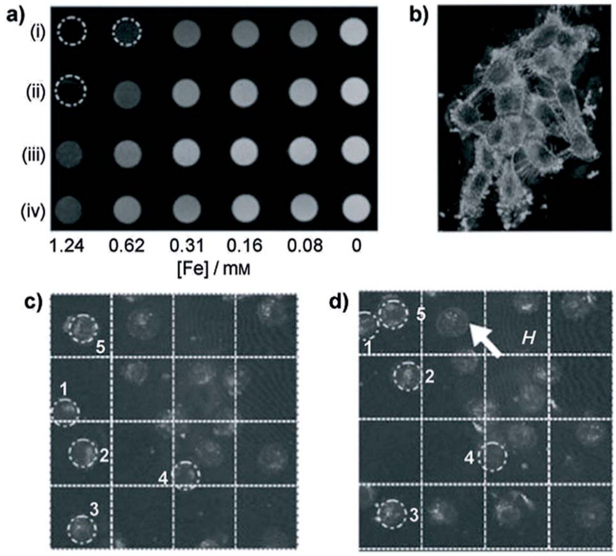

Fig. 31 (a) $T_2$-weighted MRI images of (i) 20 nm $Fe_3O_4$, (ii) 3–20 nm Au–$Fe_3O_4$, (iii) 8–20 nm Au–$Fe_3O_4$ nanoparticles, and (iv) A431 cells labeled with 8–20 nm Au–$Fe_3O_4$ nanoparticles. (b) Reflection images of A431 cells labeled with 8–20 nm Au–$Fe_3O_4$ nanoparticles. (c and d) Images of A431 cells labeled with 8–20 nm dumbbell particles, floating in the medium before (c) and after (d) an external magnetic field was applied (the field gradient in the sample area was in the range 500–100 G). The dashed circles denote individual cells; the numbers label the same cells in (c) and (d); the arrow and H indicate the direction of the applied magnetic field. Reproduced from ref. 248 with permission from Wiley-VCH.

Published on 05 December 2014. Downloaded by Library for Natural Sciences of the RAS on 23/03/2015 11:48:51.

functional probes for cell imaging applications. As a typical *in vitro* test, Sun and coworkers demonstrated that the dumbbell-like Au–$Fe_3O_4$ nanocomposites were suitable probe for A431 (human epithelial carcinoma cell line) cell imaging, as shown in Fig. 31.

Sun's group investigated the mechanical property of dumbbell-like Au–$Fe_3O_4$ nanocomposites from a synthetic point of view by overgrowing additional Au ($Au_2$) on the preformed Au–$Fe_3O_4$ composite particles ($Au_1$–$Fe_3O_4$).[260] The $Au_1$–$Fe_3O_4$ nanocomposites were first synthesized following the procedure they had published previously.[87] The $Au_2$–$Au_1$–$Fe_3O_4$ nanocomposites were prepared by overgrowing $Au_2$ onto the $Au_1$–$Fe_3O_4$ composite particles in octadecene at 80 °C in the presence of $HAuCl_4$ and oleylamine. The authors found that under the experimental conditions, the growth of $Au_2$ did not enlarge $Au_1$ in $Au_1$–$Fe_3O_4$; instead, it led to a new nucleation and epitaxial growth of $Au_2$ on $Au_1$, forming ternary structured nanocomposites. As shown in Fig. 32b–e, the TEM images of $Au_1$–$Fe_3O_4$ seeds and various nanocomposites obtained after the overgrowth at 80 °C for 1, 3, and 6 h, the $Au_1$–$Fe_3O_4$ seeds have average sizes of 5 nm for $Au_1$ and 12 nm for $Fe_3O_4$. The size of $Au_2$ was controlled by the reaction time, with 7–9 nm $Au_2$ formed after 1 h (Fig. 32c) and 12 nm after 3 h (Fig. 32d). A careful examination of the ternary $Au_2$–$Au_1$–$Fe_3O_4$ nanocomposites after 3 h growth revealed that some composite particles exhibited cracks between $Au_1$ and $Fe_3O_4$, which appeared to suggest that $Au_2$ was trying to extract $Au_1$ out of its conjugation with $Fe_3O_4$. At longer growth times, $Au_2$ won over $Fe_3O_4$ for binding to $Au_1$, and $Au_1$ thus detached from $Fe_3O_4$ to form new $Au_2$–$Au_1$ dumbbells, which dented the $Fe_3O_4$ nanoparticles, as shown in Fig. 32e. The particle size-controlled growth and modeling analysis of the stress and strain distribution across the composite particles indicated that this "tug-of-war" was due to the stress accumulated at the heterogeneous interface in $Au_1$–$Fe_3O_4$. This work by Sun's group is helpful for understanding the structural stability at the nanoscale and for the rational design of composite nanostructures for multifunctional applications.

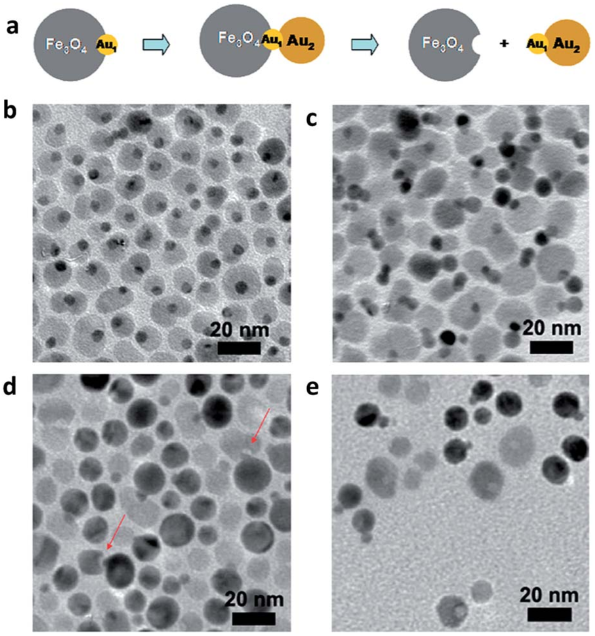

Fig. 32 "Tug-of-war" in $Au_2$–$Au_1$–$Fe_3O_4$ nanocomposites. (a) Schematic of the $Au_2$ overgrowth on the $Au_1$ domain and the $Au_1$ domain detachment from $Fe_3O_4$ domain, forming the new dumbbell-like $Au_1$–$Au_2$ and dented $Fe_3O_4$ nanoparticles. (b–f) TEM images of Au–$Fe_3O_4$ seeding particles (b), and $Au_2$–$Au_1$–$Fe_3O_4$ nanocomposites collected at 1 h (c), 3 h (d), and 6 h (e) in the synthesis. The gaps between $Au_1$ and $Fe_3O_4$ in the $Au_2$–$Au_1$–$Fe_3O_4$ nanocomposites have been labeled with red arrows in (d). Reproduced from ref. 260 with permission from the American Chemical Society.

In a subsequent research, Sun's group developed a unique protocol to understand the synergetic effect in dumbbell-like Au–$Fe_3O_4$ nanocomposites for catalyzing the reduction of $H_2O_2$.[261] The strategy started with the synthesis of dumbbell-like Au–$Fe_3O_4$ nanocomposites, and then single component Au and $Fe_3O_4$ nanoparticles were formed from the dumbbell-like Au–$Fe_3O_4$ nanocomposites by a controlled etching of the composite particles (Fig. 33), which ensured that the individual Au and $Fe_3O_4$ nanoparticles have the same structural features as their corresponding domains in the dumbbell-like Au–$Fe_3O_4$ nanocomposites. Catalytic examinations were carried out, which demonstrated that the dumbbell-like Au–$Fe_3O_4$ nanocomposites had a higher catalytic activity than that of either Au or $Fe_3O_4$ nanoparticles for $H_2O_2$ reduction. The enhanced activity of the dumbbell-like Au–$Fe_3O_4$ nanocomposites for $H_2O_2$ reduction reaction was attributed to the electronic interaction between Au and $Fe_3O_4$ domains in the composite nanoparticles.

Sun and coworkers also developed various approaches to prepare dumbbell-like nanocomposites consisting of $Fe_3O_4$ and noble metals other than gold. Typically, monodisperse dumbbell-like Pt–$Fe_3O_4$ nanocomposites were synthesized by the epitaxial growth of Fe onto Pt nanoparticles, followed by Fe oxidation.[262] The nanoparticle size in the structure was tunable from 2 to 8 nm for Pt and from 6 to 20 nm for $Fe_3O_4$. The Pt nanoparticles in the Pt–$Fe_3O_4$ nanocomposites showed a 20-fold increase in mass activity toward the oxygen reduction reaction compared with the single component Pt nanoparticles and the commercial 3 nm Pt particles. This work proves that it is possible to maximize the catalytic activity of the Pt nanoparticle

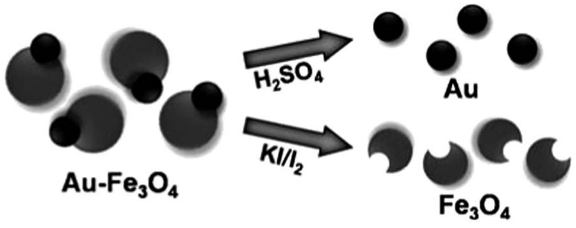

Fig. 33 Schematic illustration showing the selective etching of Au–$Fe_3O_4$ nanocomposites for the preparation of Au and dented $Fe_3O_4$ nanoparticles. Reproduced from ref. 261 with permission from Wiley-VCH.

This journal is © The Royal Society of Chemistry 2015

Published on 05 December 2014. Downloaded by Library for Natural Sciences of the RAS on 23/03/2015 11:48:51.

catalyst through control over not only the Pt size and shape, but also by controlling its interaction with $Fe_3O_4$ nanoparticles.

In recent years, Sun's group has still been very active in the synthesis and application of metal oxide–noble metal nanocomposites. By exploring advanced synthetic strategies, they have been able to greatly enrich the noble metal domains in dumbbell-like nanocomposites, *e.g.*, AuAg,[263] FePd,[264] and PtPd,[265] which has significantly enhanced the applications of the dumbbell-like nanocomposites in catalytic, biological, and biomedical areas, as well as they have provided more physical insights in this field.[265–267]

Moreover, the contribution from other research groups in metal oxide–noble metal nanocomposites cannot be ignored. Xu and coworkers reported the formation of dimeric Ag–$Fe_3O_4$ nanocomposites at the liquid–liquid interface.[268] As schematically shown in Fig. 34, the synthetic route for making the dimeric nanocomposites was easy and straightforward. The as-prepared nanoparticles of $Fe_3O_4$ were dissolved in a proper organic solvent (*e.g.*, dichlorobenzene, dichloromethane, hexane, or dioctyl ether), and then a solution of the nanoparticles was added into an aqueous solution of silver nitrate. Ultrasonic emulsification then afforded a stable emulsion of the two solutions. After a 30 min reaction period, the organic layer containing the well-dispersed dimeric Ag–$Fe_3O_4$ nanocomposites was collected by centrifugation. The authors suggest the following mechanism is responsible for generating the dimeric nanocomposites. Ultrasonication provides the necessary energy to mix the organic phase and the aqueous phase to form the microemulsion, which is stabilized by the nanoparticles that self-assemble at the liquid–liquid interface. The imperfect coverage or labile nature of the surfactant molecules on the surface of the nanoparticles allows a few Fe(II) sites to act as the catalytic center for the reduction of $Ag^+$ ions and for the seeding of the Ag nanoparticles. Once the nucleation sites of the silver are formed, the subsequent reduction of $Ag^+$ proceeds only at the pre-existing nucleation sites until the reaction stops.

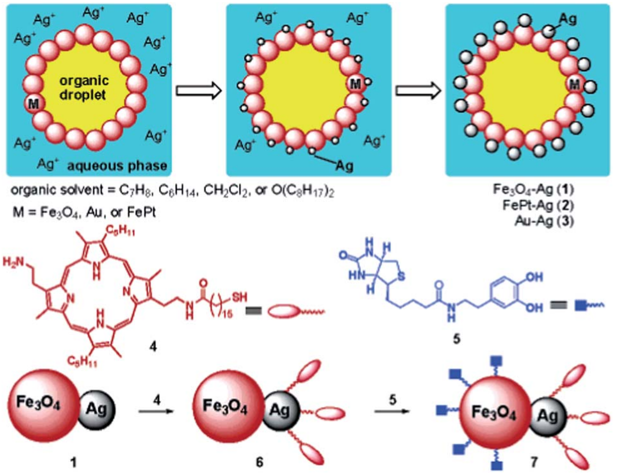

Fig. 34 Schematic illustration showing the synthesis of dimeric Ag–$Fe_3O_4$ nanocomposites at the liquid–liquid interface. Reproduced from ref. 268 with permission from the American Chemical Society.

The protocols developed by Xu's group were used by Jiang and coworkers to fabricate a noble metal nanocrystal-based two-photon fluorescence indicator combined with magnetic nanoparticles as a new class of bifunctional nanocomposite.[269] The resulting hydrophobic Ag–$Fe_3O_4$ heterodimer nanocomposite was then rendered hydrophilic by the functionalization of the iron oxide surface with hydroxyl groups, and the Ag surface with carboxyl- and amine-bearing thiol molecules. The live cells labeled with the heterodimer nanoparticles were successfully imaged by two-photon fluorescence microscopy, and manipulated using an NdFeB permanent magnet.

### 7.4 High-order nanocomposites

High-order nanocomposites refer to those with multiple (three or more) nanoscale domains fused together by solid-state interfaces, as schematically shown in a number of examples in Fig. 35. Composite nanomaterials are currently emerging as an important family of multifunctional nanoscale materials,[226,270,271] which can facilitate diverse applications in solar energy conversion,[45,46] cancer therapy,[259] Suzuki cross-coupling reactions,[272] fuel cell catalysis,[60,210,211,262,273–275] biological imaging,[24,80,276] electronics,[42] and magnetism.[277] However, more sophisticated architectures beyond binary nanocompositites are needed as the applications of these materials continue to expand and the growing disconnection between design and synthesis becomes a critical limitation in their application. Analogous to the semiconductor–noble metal or dumbbell-like metal oxide–noble metal nanocomposites, these unique hybrid lab-on-a-particle systems are also characterized by their interfacial contacts, which support direct electronic and magnetic communication between components that can lead to synergistic effects not observed for physical mixtures or nanostructures assembled using molecular or biological linkers.

Early in 2006, Swihart, Prasad and coworkers reported a general strategy capable of engineering high-order nanocomposites based on a spontaneous epitaxial nucleation and growth of a third component onto seed nanoparticles in high-temperature organic solutions.[43] In particular, magnetic ($Fe_3O_4$)–metallic (Au)–semiconductor (PbSe or PbS) ternary

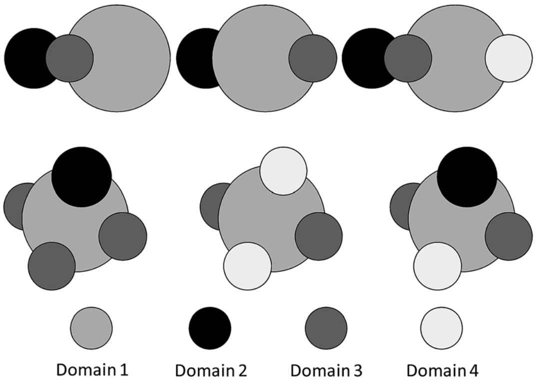

Fig. 35 Schematic illustration showing high order nanocomposites, in which the multiple nanoscale domains are fused together by solid-state interfaces.

Published on 05 December 2014. Downloaded by Library for Natural Sciences of the RAS on 23/03/2015 11:48:51.

nanocomposites were prepared using Au–$Fe_3O_4$ peanut-like nanoparticles, with 12 nm $Fe_3O_4$ and 3–4 nm Au domains as the seeds. The authors found that the heating strategy and seed particle dimensions were important for the formation of ternary nanocomposites. If the gold domain was less than 3 nm in diameter, then the nucleation of PbS or PbSe was difficult presumably because of the small amount of gold surface area exposed. For $Fe_3O_4$–Au–PbS, if the temperature of the reaction mixture was quickly increased to 150 °C after sulfur injection, both dumbbell-like Au–$Fe_3O_4$ composite nanoparticles and $Fe_3O_4$–Au–PbS ternary nanocomposites were formed. This suggests that some Au–$Fe_3O_4$ peanut-like particles aggregated to form dumbbell-like Au–$Fe_3O_4$ particles in the presence of sulfur before PbS could nucleate and grow on Au–$Fe_3O_4$. When the temperature was held at 100 °C after sulfur injection, $Fe_3O_4$–Au–PbS was formed and no dumbbell-like Au–$Fe_3O_4$ particles were observed.

Schaak's group made a significant contribution to the synthesis of high-order nanocomposites by demonstrating that known chemical reactions can be applied in a predictable and stepwise manner to build complex composite nanoparticle architectures including M–Pt–$Fe_3O_4$ (M = Au, Ag, Ni, Pd) heterotrimers, $M_xS$–Au–Pt–$Fe_3O_4$ (M = Pb, Cu) heterotetramers and higher-order oligomers based on the heterotrimeric Au–Pt–$Fe_3O_4$ building block.[278] As a typical example, the authors studied the reduction of a 1-octadecene solution of $HAuCl_4$ with oleylamine in the presence of Pt–$Fe_3O_4$ dumbbell-like nanocomposites at mild (60–90 °C) temperatures. Although the heterogeneous nucleation of Au on Pt–$Fe_3O_4$ seeds might be expected to yield four primary products: Au on Pt, Au on $Fe_3O_4$, Au on both the $Fe_3O_4$ and Pt ends, and Au at the interface of both $Fe_3O_4$ and Pt (Fig. 36a), the authors observed only Au–Pt–$Fe_3O_4$ as the exclusive heterotrimer product (Fig. 36d), which was formed in an approximately 85% yield. The remainder of the product consisted of either unreacted Pt–$Fe_3O_4$ or higher-order structures that were formed from a small number of $Fe_3O_4$–Pt–$Fe_3O_4$ seeds present in the original Pt–$Fe_3O_4$ sample. In the same manner, Ag–Pt–$Fe_3O_4$ (Fig. 36e), Ni–Pt–$Fe_3O_4$ (Fig. 36f) and Pd–Pt–$Fe_3O_4$ (Fig. 36g) could also be synthesized by reducing Ag(I) acetate (Ag(OAc)), $Ni(acac)_2$ and $Pd(acac)_2$, respectively, in the presence of the Pt–$Fe_3O_4$ seeds. Analogous to the Au–Pt–$Fe_3O_4$ system, each reaction resulted in the heterogeneous nucleation of Ag, Ni or Pd exclusively onto the Pt domain of the Pt–$Fe_3O_4$ seeds. The authors did not observe the nucleation of Au, Ag, Ni or Pd on the $Fe_3O_4$ domain or across the Pt–$Fe_3O_4$ interface. This result demonstrates that the chemoselective deposition of a variety of metals occurs exclusively onto the Pt ends of the Pt–$Fe_3O_4$ heterodimers, with no observable side products.

The high electron density around the Pt domain, which was attributed to the electron transfer from $Fe_3O_4$ to Pt,[262] helps to rationalize the observed chemoselectivity. The electron-rich Pt domain may help to anchor and reduce the cationic Au, Ag, Ni and Pd reactants, as well as enhance the polarizability of the Pt domain to help facilitate greater surface interaction with the small nuclei of these metals. This could be considered as a nanocrystal analogue of a molecular substituent effect, in which the enhanced reactivity at a specific site is driven by the electron-transfer phenomenon, which is a well-known phenomenon in the studies related to heterogeneous catalysis.[279–284] The presence of $Fe_3O_4$ and the electronic interactions across the $Fe_3O_4$–Pt interface modify the reactivity of the Pt domain, which makes it behave differently to isolated Pt nanoparticles in a manner that facilitates the chemoselective nucleation and a regiospecific M–Pt–$Fe_3O_4$ connectivity.

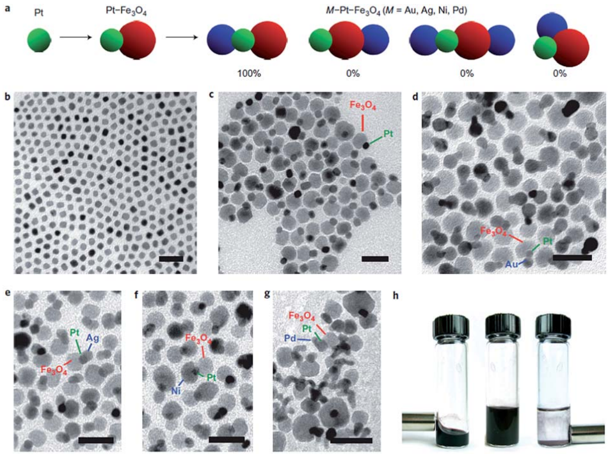

Fig. 36 Stepwise construction of M–Pt–$Fe_3O_4$ heterotrimers (M = Ag, Au, Ni, Pd) (a), schematic showing the multistep synthesis of M–Pt–$Fe_3O_4$ heterotrimers, along with the most significant possible products and their observed frequencies (expressed as the percentage of observed heterotrimers, not total yield). Representative TEM images showing the Pt nanoparticle seeds (b), Pt–$Fe_3O_4$ heterodimers (c) and Au–Pt–$Fe_3O_4$ (d), Ag–Pt–$Fe_3O_4$ (e), Ni–Pt–$Fe_3O_4$ (f) and Pd–Pt–$Fe_3O_4$ (g) heterotrimers. All the scale bars are 25 nm. (h), Images of a vial that contains Au–Pt–$Fe_3O_4$ heterotrimers in hexane (left), which respond to an external Nd–Fe–B magnet; the same vial with Au–Pt–$Fe_3O_4$ heterotrimers in a larger volume of hexanes (middle); and the same vial after precipitation of the heterotrimers with ethanol (right). The precipitated heterotrimers collect next to the external magnet. Reproduced from ref. 278 with permission from the Nature Publishing Group.

This synthetic framework, suggested by Schaak's group, conceptually mimics the total-synthesis approach used by chemists to construct complex organic molecules. The reaction toolkit applies solid-state nanoparticle analogues of chemoselective reactions, regiospecificity, coupling reactions, and molecular substituent effects for the construction of exceptionally complex composite nanoparticle oligomers. Moreover, the emerging advances in nanoparticle separation and purification could further improve yield and homogeneity,[285–288] and the continued development of new classes of reactions, including orthogonal reaction schemes,[289,290] could further expand these synthesis-by-design capabilities.

### 7.5 $RuO_2$-based nanocomposites

Instead of the commonly used seed-mediated growth method, we developed a solvothermal strategy and a mutual oxidation–reduction approach for the fabrication of ruthenium oxide ($RuO_2$)-based nanocomposites including $RuO_2$ and $RuO_2$–Au supported on commercial carbon supports ($RuO_2$–C and $RuO_2$–

Published on 05 December 2014. Downloaded by Library for Natural Sciences of the RAS on 23/03/2015 11:48:51.

Au–C nanocomposites).[291] The novelty of the nanocomposites lies in their synthetic approaches, which are based on the thermal decomposition of metal complexes formed by $RuCl_3$ and dodecylamine at room temperature (for $RuO_2$–C) and the mutual oxidation–reduction phenomenon between $RuCl_3$ and $HAuCl_4$ at elevated temperatures (for $RuO_2$–Au–C) in the presence of carbon supports. As indicated in Fig. 37, the $RuO_2$ and $RuO_2$–Au particles in $RuO_2$–C and $RuO_2$–Au–C nanocomposites are nearly monodispersed, and have average sizes of 1.8 nm and 1.62 nm, respectively. The as-prepared $RuO_2$–C and $RuO_2$–Au–C nanocomposites used for supercapacitors adopting the $H_2SO_4$ electrolyte exhibit high specific capacitances of 537.7 F $g^{-1}$ and 558.2 F $g^{-1}$, respectively, at a current density of 50 mA $g^{-1}$. The specific capacitance maintains 350.1 F $g^{-1}$ for $RuO_2$–C nanocomposites and 478.5 F $g^{-1}$ for $RuO_2$–Au–C nanocomposites at a current density of 200 mA $g^{-1}$ with good cycling stability. In addition, comparison of the electrochemical measurements of the $RuO_2$–C and $RuO_2$–Au–C nanocomposites demonstrates that the presence of Au in the nanocomposites is favorable for an enhancement of the capacitive behavior of $RuO_2$. Considering the remarkable simplicity of the synthetic approaches, the strategies might be promising for creating $RuO_2$-based nanocomposites on a large scale for application in electrochemical capacitors.

## 8 Nanocomposite-related scientific issues

Nanomaterials are proving to be fertile grounds for scientific discoveries and explorations because materials at the nanoscale often exhibit properties that are significantly different from those of single atoms and their bulk counterparts.[292–294] For instance, the confinement or collective oscillation of electrons in the conduction band by a nanoscale particle provides a powerful means to manipulate the electronic, optical, magnetic and catalytic properties of a solid material.[2,35,295–299] For example, although bulk gold does not exhibit catalytic properties, Au nanoparticles have been demonstrated to usually be excellent low temperature catalysts. Another typical examples are the optical properties of Ag–Au nanoparticles arising from surface plasmon resonance (SPR),[300] where the size- and shape-dependent optical properties make gold and silver at nanometer scale useful as sensors, biomarkers, and as building blocks for photonic, optical, and optoelectronic devices.[296,301]

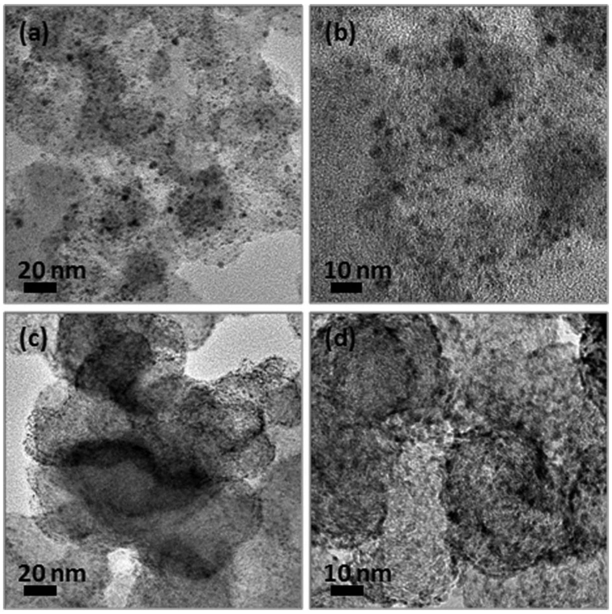

Fig. 37 TEM (a and c) and HRTEM images (b and d) of $RuO_2$–C (a and b) and $RuO_2$–Au–C nanocomposites (c and d) as-prepared by a solvothermal strategy and a mutual oxidation–reduction approach, respectively. Reproduced from ref. 291 with permission from the Royal Society of Chemistry.

In this section, we introduce a number of interesting scientific phenomena observed during the syntheses and characterizations of composite nanomaterials, including the room temperature synthesis and growth mechanism of $Ag_2S$ nanocrystals in a nonpolar organic solvent, the diffusion of gold from the inner core to the surface of $Ag_2S$ nanocrystals, the coalescence of $Ag_2S$ and Au nanocrystals at room temperature, a facile solution route for the synthesis of PbSe–Au nanocomposites with different morphologies, and selective electrocatalysts toward a prototype of the membraneless direct methanol fuel cell. The mechanisms behind these scientific issues and their potential applications will also be discussed in this section regarding the specific features of these discoveries. These interesting scientific phenomena or physical/chemical processes not only satisfy our everlasting human curiosity, but also promise new advances in technology, *e.g.*, the design of sophisticated composite nanomaterials and highly efficient electrocatalysts with superior selectivity.

### 8.1 Room temperature synthesis and growth mechanism of $Ag_2S$ nanocrystals

$Ag_2S$ nanocrystals have become one of the most commonly studied semiconductor nanocrystals (or quantum dots) for their excellent photoelectric and thermoelectric properties and their significant roles in optics, electronics, and near-infrared (NIR) fluorescence probes (*e.g.*, in biological labeling).[302–306] In addition, $Ag_2S$ nanocrystals can be fabricated into semiconductor–metal nanocomposites, which are effective for the catalysis of methanol oxidation at room temperature.[60] Therefore, the synthesis of $Ag_2S$ nanocrystals with uniform sizes and controlled shapes using easily accessible precursors under mild reaction conditions has become an important subject of research. To date, various methods have been developed for the synthesis of $Ag_2S$ nanocrystals. These preparative approaches are usually carried out in organic solvents at high temperatures using expensive and unstable organometallic precursors (*e.g.*, Ag(SCOPh),[302] $(C_2H_5)_2NCS_2Ag$,[304–306] and $CH_3COOAg$[307]). The reaction between Ag inorganometallic precursors (*e.g.*, $AgNO_3$) and S powders in a coordinating solvent, *e.g.*, octadecylamine, provides an improved route to produce $Ag_2S$ NCs,[49,308,309] while the temperature of the reaction system is still maintained at 150 °C or higher. A specific method based on cation exchange

Published on 05 December 2014. Downloaded by Library for Natural Sciences of the RAS on 23/03/2015 11:48:51.

has also been used for the synthesis of $Ag_2S$ NCs.[144,310–312] In this method, the dissolved $Ag^+$ ions displace the $Cd^{2+}$ or $Cu^{2+}$ cations from previously formed CdS nanorods or CuS hollow spheres, and the size and shape of the final $Ag_2S$ products are controlled by the CdS or CuS templates.

Alternatively, Yang and coworkers described a simple and facile room-temperature approach derived from the general phase transfer protocol for the synthesis of uniform $Ag_2S$ nanocrystals, which involved the transfer of $Ag^+$ ions from water to toluene using an ethanol-mediated method, and by reaction with elemental sulfur in toluene at room temperature.[48,313] This protocol allows $Ag_2S$ nanocrystals to be synthesized in an organic medium using aqueous soluble metal salts as the starting materials, which are relatively inexpensive and can be easily obtained. The growth mechanism of $Ag_2S$ nanocrystals in nonpolar organic solvents was found to be remarkably different from the commonly accepted LaMer nucleation-growth model consisting of a nucleation step and growth step.[314,315] As demonstrated in Fig. 38, during the initial stage of the reaction, $Ag_2S$ nanoclusters formed on the surface of the massive S powders and then coalesced to form an extensive network of nanowires, which later fragmented into quasi-spherical particles due to the inside-out diffusion of S in the nanowires. The quasi-spherical particles finally grew into uniform $Ag_2S$ nanocrystals through a ripening process. It was found that the reaction temperature and the molar ratio of Ag/S have a significant influence on the growth process and on the size/morphology of the $Ag_2S$ nanocrystals. The shape of the final $Ag_2S$ products could be easily tuned by varying the molar ratio of the starting precursors. This "coalescence-fracture-ripening" growth mechanism could also be applied for the synthesis of uniform $Ag_2S$ nanocrystals using previously formed Ag nanoparticles as starting materials.

The room-temperature approach for the synthesis of $Ag_2S$ nanocrystals could be easily extended to the preparation of dimeric $Ag_2S$–Au nanocomposites.[28] After aging a mixture of $Ag_2S$ and $HAuCl_4$, which was then transferred into toluene using the ethanol-mediated general phase transfer protocol, dimeric $Ag_2S$–Au nanocomposites were found to be the dominant product (Fig. 39a and b). It is noteworthy that in the absence of $Ag_2S$ nanocrystals, the reduction of Au(III) ions by dodecylamine would require several days; this suggests that the $Ag_2S$ NCs could catalyze the reduction of $Au^{3+}$ ions, as indicated in the PbS–Au system.[44] When the order of nanocrystal synthesis was reversed, *i.e.*, when $Ag_2S$ nanocrystals were generated in the

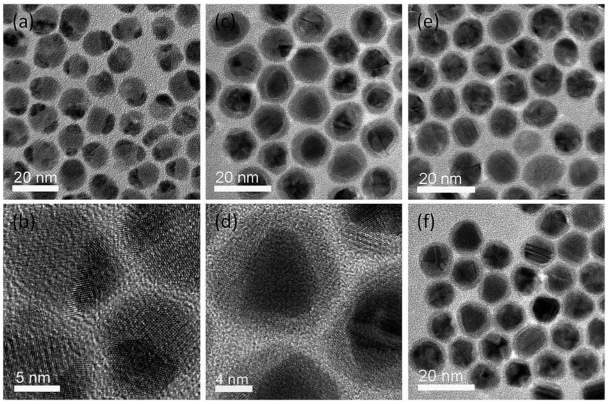

Fig. 39 TEM (a, c, e and f) and HRTEM images (b and d) of $Ag_2S$–Au heterodimers (a and b), core–shell Au@$Ag_2S$ nanoparticles at $Ag_2S$–Au molar ratios of 2 : 1 (c and d), 1 : 1 (e), and 1 : 2 (f), respectively. Reproduced from ref. 48 with permission from the Royal Society of Chemistry.

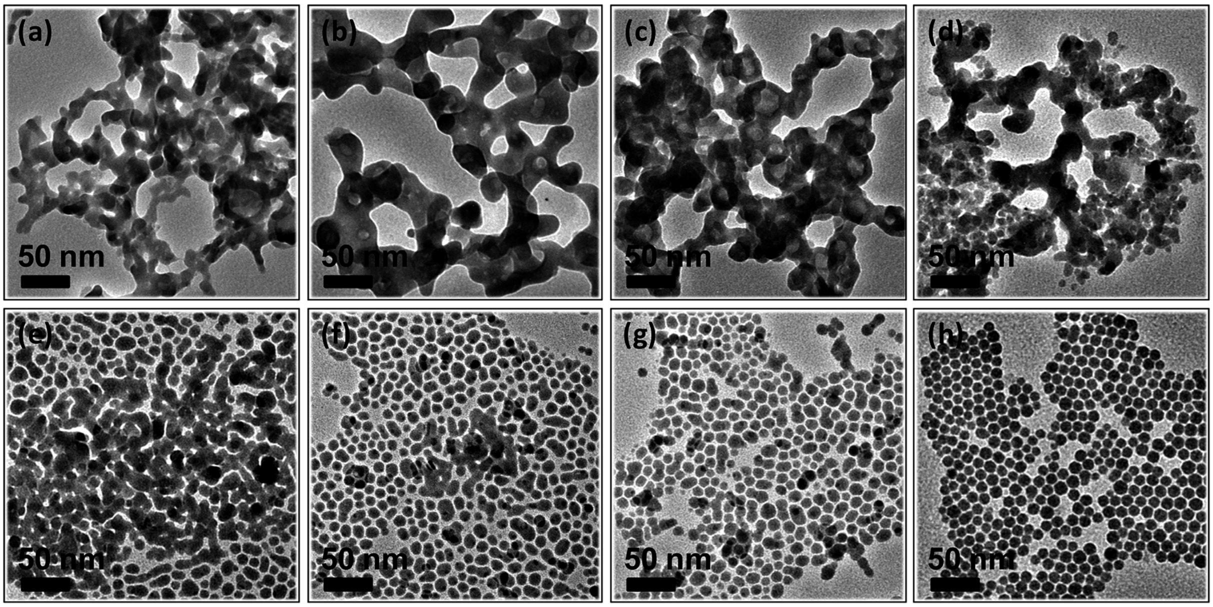

Fig. 38 TEM images of $Ag_2S$ nanocrystals obtained by reacting DDA–$Ag^+$ complexes with elemental sulfur in toluene at 283 K at different times: (a) 1 h, (b) 2 h, (c) 5 h, (d) 15 h, (e) 25 h, (f) 40 h, (g) 80 h, and (h) 1 month. Reproduced from ref. 313 with permission from the Royal Society of Chemistry.

Published on 05 December 2014. Downloaded by Library for Natural Sciences of the RAS on 23/03/2015 11:48:51.

presence of Au nanoparticles, $Ag_2S$ grew homogeneously on the existing Au nanocrystals, resulting in a core–shell Au@$Ag_2S$ structure (Fig. 39c and d, Au : $Ag_2S$ molar ratio = 1 : 2).[48] The thickness of the $Ag_2S$ shell could be controlled by varying the Au : $Ag_2S$ molar ratio in the synthesis. Fig. 39e and f illustrate the core–shell Au@$Ag_2S$ nanocrystals synthesized at Au : $Ag_2S$ molar ratios of 2 : 1 and 1 : 1, respectively. Moreover, the thickness of the $Ag_2S$ shell could be varied, as shown by comparing Fig. 39c, e and f.

As we will describe in the subsequent section, the core–shell Au@$Ag_2S$ nanoparticles are not thermodynamically stable, and at room temperature, Au could diffuse from the core of the particle to the surface, giving rise to the formation of dimeric $Ag_2S$–Au nanocomposites.

### 8.2 Diffusion of gold from the inner core to the surface of $Ag_2S$ nanocrystals

The diffusion of metals in semiconductors has been extensively investigated in bulk materials due to its technological importance for applications in doped materials, catalysts, and functional spintronic devices.[316–321] In contrast, relatively little has been reported on the diffusion in nanostructured materials, which exhibit physical and chemical properties distinctively different from bulk materials.[322–324] Recently, Banin and coworkers reported the diffusion of Au in InAs nanoparticles at room temperature, which resulted in a Au core coated by an amorphous InAs shell.[85] Manna *et al.* also described the diffusion of Au in PbTe nanocrystals at elevated temperatures.[325] In a later study, Yang and Ying discovered an interesting diffusion phenomenon of noble metals in semiconductor nanocrystals. They found that Au could diffuse in $Ag_2S$ nanocrystals from the core to the surface, giving rise to dimeric $Ag_2S$–Au heteronanocomposites.[53] The TEM and high-angle scanning transmission electron microscopy (STEM) images of the core–shell Au@$Ag_2S$ nanoparticles are shown in Fig. 40a and c, respectively, in which the core and shell components can be easily differentiated by the contrast in brightness. The diffusion of Au in $Ag_2S$ from the core to the surface was completed after 72 h of aging (Fig. 40b and d). The resulting dimeric $Ag_2S$–Au nanocomposites (heterodimers) are clearly distinct from the starting core–shell Au@$Ag_2S$ nanoparticles. Energy-dispersive X-ray (EDX) analyses (Fig. 40e and f) of an arbitrary single particle before and after 72 h of aging under STEM mode show that gold moved from the core of the Au@$Ag_2S$ nanoparticle to the surface of the $Ag_2S$ nanocrystal, forming $Ag_2S$–Au heterodimers. The $Ag_2S$ domain remains crystalline after the diffusion of Au from the core to the surface. This is different from the InAs–Au and PbTe–Au systems, in which an amorphous shell of InAs or PbTe, respectively, is left behind after the diffusion of Au from the surface to the core.[85,325]

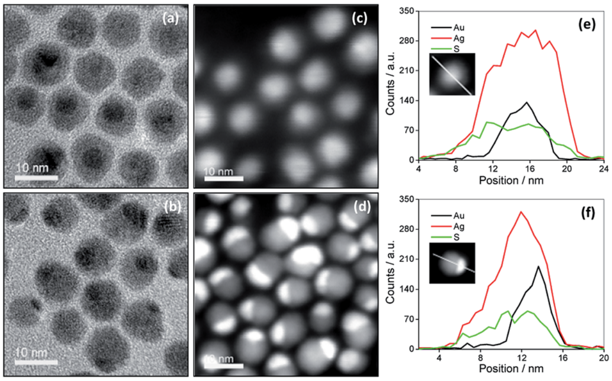

Fig. 40 Diffusion of Au from the inner core to the surface of core–shell Au@$Ag_2S$ nanoparticles: (a and b) TEM images, (c and d) STEM images, and (e and f) elemental profiles of the core–shell Au@$Ag_2S$ nanoparticles (a, c and e) as-prepared and (b, d and f) after 72 hours of aging. Reproduced from ref. 50 with permission from the American Chemical Society.

This reverse diffusion of Au, which could be interpreted by the substitutional–interstitial mechanism, not only has a scientific significance, but also could be used to synthesize complex semiconductor–metal nanocomposites that might not be obtained by direct synthesis. In particular, the synthesis of heterogeneous nanocomposites of core–shell Pt@$Ag_2S$ and Au nanoparticles was demonstrated based on the diffusion of Au in $Ag_2S$ nanocrystals. Ostwald ripening was observed during the characterization of the nanocomposites by TEM (Fig. 41). This elucidated the mechanism of the formation of semiconductor–metal heterostructures as a consequence of the diffusion of Au in $Ag_2S$ nanocrystals. Initially, Au atoms might have diffused in all directions within $Ag_2S$. However, nanocrystals of Au were later formed on the $Ag_2S$ surface, and grew steadily due to Ostwald ripening.

### 8.3 Coalescence of $Ag_2S$ and Au nanocrystals at room temperature

Materials at the nanometer scale may possess new physical/chemical properties or exhibit new physical/chemical phenomena. For example, as mentioned in the previous section, in InAs–Au nanocomposites, Au could diffuse into InAs nanocrystals at room temperature, resulting in a Au core coated by an amorphous InAs shell.[85] In this section, another interesting phenomenon occurring in nanoscale materials, *i.e.*, a

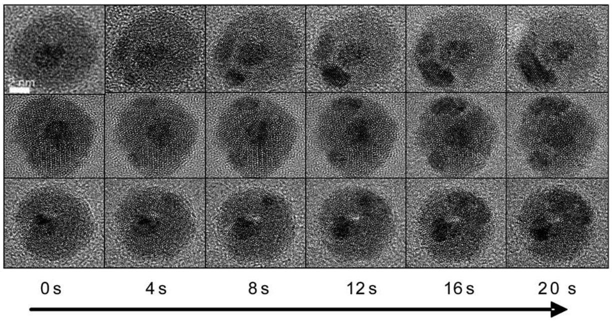

Fig. 41 Ostwald ripening observed during the diffusion of Au in $Ag_2S$. Initially, Au homogeneously diffused in $Ag_2S$ but then evolved as growing nanocrystals on the $Ag_2S$ surface due to Ostwald ripening. Reproduced from ref. 50 with permission from the American Chemical Society.

Published on 05 December 2014. Downloaded by Library for Natural Sciences of the RAS on 23/03/2015 11:48:51.

dissolution–renucleation process leading to the coalescence of $Ag_2S$ and Au nanocrystals at room temperature was observed in an organic medium. Individual $Ag_2S$ and Au nanocrystals in their physical mixture were eventually fused with each other to yield the dimeric $Ag_2S$–Au nanocomposites, as confirmed by the TEM images taken at different time (Fig. 42).[53]

The coalescence between Au and $Ag_2S$ nanocrystals at room temperature could be interpreted by an equilibration of the Fermi levels in the two different types of particles, which has also been observed in a colloidal mixture of lead and silver nanoparticles.[326] As illustrated in Fig. 43c, initially, Au and $Ag_2S$ nanocrystals undergo Brownian encounters in their physical mixture, and then the electrons may tunnel from the Au atoms on the surface of Au nanocrystals to their neighbouring $Ag_2S$ nanocrystals due to the energy level alignment (Fig. 43b). Simultaneously, Au ions are emitted from the Au nanocrystals into the solution. Finally, these Au ions capture the electrons on the surface of $Ag_2S$ nanocrystals, resulting in the renucleation of Au on $Ag_2S$ nanocrystals. In this process, the Au dissolution and renucleation could have occurred around the surface of $Ag_2S$ nanocrystals, and then segregated patches of Au form on each $Ag_2S$ surface due to Ostwald ripening.[50]

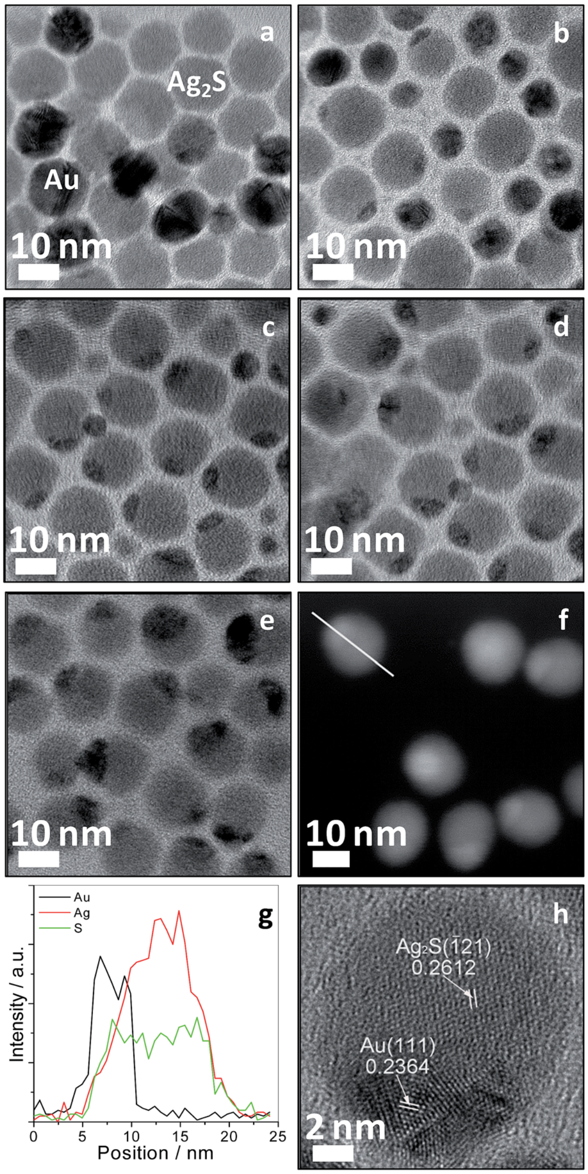

Fig. 42 Coalescence of $Ag_2S$ and Au nanocrystals: (a–e) TEM images of the physical mixture of $Ag_2S$ and Au nanocrystals taken at 0 h, 7 h, 12 h, 24 h, and 36 h, respectively; (f) HAADF-STEM image of $Ag_2S$–Au heterodimers; (g) Au, Ag, and S elemental distributions across a single $Ag_2S$–Au heterodimer (white line indicated in (f)); (h) HRTEM image of a single $Ag_2S$–Au heterodimer. Reproduced from ref. 53 with permission from the Royal Society of Chemistry.

A common coalescence process usually occurs in the homogeneous nanoparticle dispersion and is terminated by the formation of well-confined morphologies such as rods, wires, dendrites and 2-D or 3-D arrays.[327–329] Usually, the coalescence is induced by annealing, drying, or ultrasonic treatment.[330,331] The coalescence between heterogeneous nanocrystals may promise new research techniques. For example, this coalescence process could be applied to extract Au from quantum dot–Au hybrids or from Au-containing alloys; thus, providing an effective strategy to investigate the influence of Au on the properties of Au-containing hybrids or alloys.

### 8.4 PbSe–Au nanocomposites with different morphologies

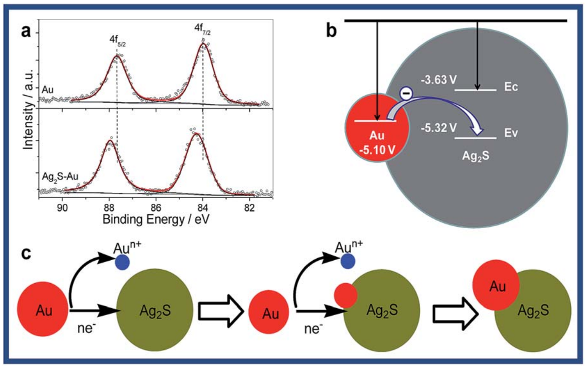

Fig. 43 (a) Au 4f XPS spectra of the original Au nanocrystals and the resulting $Ag_2S$–Au heterodimers; (b) Energy level diagram for $Ag_2S$–Au heterodimers, which predicts the intraparticle charge transfer from Au to $Ag_2S$; (c) Schematic for the coalescence between Au and $Ag_2S$ nanocrystals at room temperature *via* the equilibration of the Fermi levels in the two different types of particles. Reproduced from ref. 53 with permission from the Royal Society of Chemistry.

Because the final morphology of nanocomposites depend on whether the surface of the substrate particles allow for only a single nucleation site or multiple ones, the use of different semiconductor substrates may generate new and insightful results. When depositing gold (Au) on lead selenide (PbSe) semiconductor substrates, Yang's group reported an interestingly experimental observation and understanding of the growth process of gold on the surface of PbSe nanocrystals.[54] They found that the molar ratio of PbSe–Au had a great influence on the morphology of the PbSe–Au nanocomposites. The evolution from nanocomposites with multiple Au deposition on the particle surface to those with a single Au domain, and

This journal is © The Royal Society of Chemistry 2015

Published on 05 December 2014. Downloaded by Library for Natural Sciences of the RAS on 23/03/2015 11:48:51.

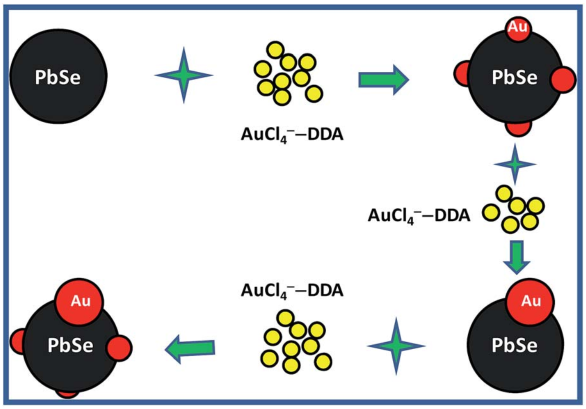

Fig. 44 Schematic of the fabrication of PbSe–Au nanocomposites at different PbSe–Au molar ratios. Reproduced from ref. 54 with permission from the Royal Society of Chemistry.

further to pineapple-like morphologies was observed with the increasing molar ratio of Au–PbSe during the synthesis, as schematically illustrated in Fig. 44. Surprisingly, the experimental observations showed that the growth of Au on the surface of PbSe had an upper limit size. Upon the achievement of this size, the addition of more Au precursors only resulted in the deposition of Au on extra sites over the surface of PbSe instead of a continuous growth of the Au domain; these were termed 'pineapple-like' nanocomposites. Therefore this process extends the opportunities available for the fabrication and control of nanostructures, in particular for nanocrystals composed of different materials.

### 8.5 Selective electrocatalysts toward a prototype of the membraneless direct methanol fuel cell

The strong growing interest in using direct methanol fuel cells (DMFCs) as portable and mobile power sources is rooted in their desirable features of a relatively small environmental footprint, compact system design, and higher volumetric energy densities compared with existing technologies.[190,332] The anode and cathode catalysts of DMFCs are commonly based on Pt.[333–338] These catalysts are not selective to methanol oxidation reaction (MOR) at anode or oxygen reduction reaction (ORR) at cathode, and thus any methanol crossover from the anode to the cathode through the proton exchange membrane can be oxidized by the cathode catalyst. This results in the creation of a mixed potential at the cathode, which degrades the fuel cell performance.[191,339,340] Although a number of research studies have been devoted toward the modification on the proton exchange membrane to overcome this key obstacle for the commercialization of DMFCs, it is generally considered that the commonly used Nafion membrane still has an unacceptably high rate of methanol crossover.[341–347] In this sense, the synthesis of electrocatalysts with high selectivity for MOR and ORR represents an alternative for solving this problem in DMFCs.

With a deep understanding of the mechanisms of the electrocatalytic reactions, Yang's group reported the design and fabrication of Pt-based nanomaterials with enhanced catalytic activity and a high selectivity towards DMFC reactions by making sufficient use of the structural uniqueness and electronic coupling effects between the different domains of the electrocatalysts, so that DMFCs could be efficiently operated without, or at least with little, dependence on the proton exchange membrane.[274] In particular, they reported ternary Au@$Ag_2S$–Pt nanocomposites that displayed a superior methanol oxidation reaction (MOR) selectivity due to the electronic coupling effect between the different domains of the nanocomposites (Fig. 45a), while cage-bell-structured Pt–Ru nanoparticles exhibited excellent methanol tolerance for the oxygen reduction reaction (ORR) at the cathode because of the differential diffusion of methanol and oxygen in the porous Ru shell of the cage-bell nanoparticles (Fig. 45b). The good catalytic selectivity of these Pt-based nanomaterials *via* structural construction enabled a DMFC to be built without a proton exchange membrane between the fuel electrode and the oxygen electrode (Fig. 45c).

The performance of the membraneless DMFC was evaluated in terms of the open circuit voltage (OCV), the current–voltage

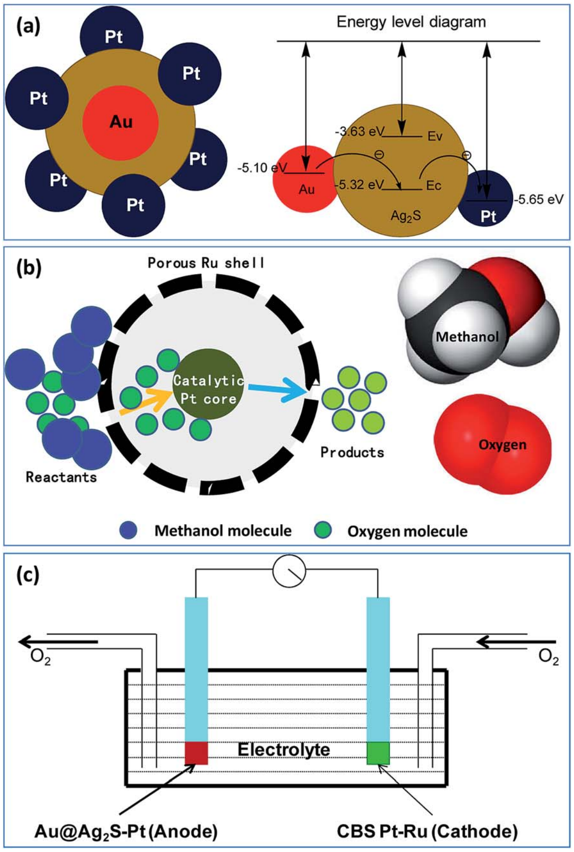

Fig. 45 Schematic illustration of the construction of ternary Au@$Ag_2S$–Pt nanocomposites and the energy level alignment in $Ag_2S$–Au–Pt nanocomposites (a), schematic illustration of the differential diffusion and reaction of methanol and oxygen in CBS Pt–Ru nanoparticles (b), and schematic illustration of the membraneless DMFC (c). Reproduced from ref. 274 with permission from the Nature Publishing Group.

Published on 05 December 2014. Downloaded by Library for Natural Sciences of the RAS on 23/03/2015 11:48:51.

($I$–$V$), and the current–power ($I$–$P$) characteristics under ambient conditions. It was found that the membraneless DMFC with the selective MOR catalyst at the anode and the ORR catalyst at the cathode could maintain an open-circuit voltage of *ca.* 0.38 V for more than 120 min. It is of great importance that a reasonable power with the maximum value of *ca.* 15 μW was obtained without a separate membrane. However, the OCV of the membraneless DMFC was still rather low, at only *ca.* 32% of the theoretical cell voltage of DMFC (*ca.* 1.18 V).[348] The performance of the prototype might have been limited by the use of dissolved oxygen as the source of oxygen. However, despite the limited performance, the prototype did demonstrate the viability of using selective MOR and ORR catalysts to construct a DMFC without the proton exchange membrane. Because the exemption of a proton exchange membrane not only reduces the cost and volume of the DMFC, it also provides more flexibility and allows for miniaturization of the cell design. Its implementation is also simpler than membraneless fuel cells that depend on non-mixing laminar flows[349,350] or a 3D anode.[351–353] The performance of the membraneless fuel cell could be improved using the on-chip fuel cell developed by Osaka's group, which can directly make use of the oxygen from the air.[354]

## 9 Applications of noble metal-based composite nanomaterials

The valuable technological applications of composite nanomaterials envisaged in disparate fields, including photocatalysis, optoelectronics, sensing, and biomedicine, have been recently reviewed by a number of research groups.[61,226,271,355–359] In addition, discussions on the catalytic applications of Pt-containing noble metal-based nanocomposites in direct methanol fuel cell reactions are scattered around in related sections of this review work. Therefore, in this section, we emphasize the catalytic applications of noble metal-based nanocomposites in organic syntheses.

Propargylamines are useful and versatile precursors for the synthesis of various nitrogen-containing biologically active compounds such as natural products and therapeutic drug molecules.[360–364] In comparison with the classical methods involving the nucleophilic addition of an alkynyl–Li or Mg reagent to an imine or other similar C=N electrophiles,[365] a more attractive and atom-efficient strategy for propargylamine synthesis is through a one-pot three-component coupling reaction of an aldehyde, amine and alkyne *via* C–H activation catalyzed by a transition metal. Catalytic multicomponent reactions are highly atom-efficient processes that can enable the implementation of several transformations in a single manipulation. These reactions also produce less side-products compared to classical stepwise methodologies. A number of homogeneous systems, such as iron salts and[366] copper salts[367] and their complexes,[368] silver salts[369–372] and gold salts[373,374] and their complexes,[375,376] iridium complexes,[377] $Hg_2Cl_2$,[378] and a Cu/Ru[379] bimetallic system, have been reported for the preparation of propargylamine *via* this three-component coupling protocol. Although these catalysts were highly effective, the homogeneous systems could not be recovered for reuse.

Heterogeneous catalysts, on the other hand, would be able to overcome this recyclability issue. Heterogeneous systems, such as silica- or hydroxyapatite-supported $Cu^+$ complexes,[380–382] CuO nanoparticles,[383] $Ag^+$ salts in ionic liquids,[384] unsupported[385] and supported gold nanoparticles on $CeO_2$ and $ZrO_2$,[386] and layered double hydroxide,[387] have been reported to display high activities for the three-component coupling reaction of an aldehyde, amine and alkyne. In those reports, some of the heterogeneous catalysts have been recovered and reused for a number of cycles with nearly consistent activity. Referring to the abundant accumulation of semiconductor–gold nanocomposites in recent years, which creates great opportunities but also a tremendous challenge to apply these materials, Chng and coworkers investigated the application of semiconductor–gold nanocomposites for the synthesis of propargylamines *via* a three-component coupling reaction of an aldehyde, amine and alkyne in water. Their process is simple and applicable to a diverse range of aromatic and aliphatic aldehydes, amines and alkynes. Furthermore, the catalyst was stable in air and water, and could be easily recovered and reused.[388]

They prepared three different types of semiconductor nanocrystals for gold deposition *via* solution-based methods. Fig. 46 shows the TEM images of the CdS, CdSe and PbS semiconductor nanocrystals and their nanocomposites with gold. Because gold has a strong imaging contrast, it can be easily identified in the semiconductor–gold nanocomposites. Gold was deposited at multiple sites on each semiconductor. EDX analyses confirm that the heterogeneous structures are composed of the semiconductor and gold components. The gold loading on the semiconductor nanocrystals ranged from 17.1 to 25.4 wt%, and the gold nanoparticles were 1–2 nm in diameter (Fig. 46).

The three semiconductor–Au nanocomposites were tested for their catalytic activities in the three-component coupling reaction for the model substrates: benzaldehyde, piperidine, and phenylacetylene in water at 100 °C, and the results showed that with a catalyst loading of 0.3 mol% Au and a reaction time of 6 h at 100 °C in air, the PbS–Au nanocomposites provided the highest activity, giving rise to the desired propargylamine product by up to 85% in an isolated yield, while the CdS–Au and CdSe–Au nanocomposites gave lower isolated yields of 43% and 53%, respectively. The XPS measurements demonstrated that the oxidized ratio of Au in the PbS–Au nanocomposites was higher than in the CdS–Au and CdSe–Au nanocomposites, which may account for the highest catalytic activity of the PbS–Au nanocomposites in the three-component coupling reaction.

Chng and coworkers also proposed a tentative mechanism for the three-component coupling reaction catalyzed by PbS–Au nanocomposites, as demonstrated by the scheme in Fig. 47. They suggested that the reaction mechanism of the PbS–Au catalyst could proceed *via* the activation of the $C_{sp}$–H bond of the terminal alkyne by the PbS–Au nanocomposite. The alkynyl–Au intermediate generated would then react with the immonium ion generated *in situ* from the aldehyde and the secondary amine to produce the corresponding propargylamine product,

Published on 05 December 2014. Downloaded by Library for Natural Sciences of the RAS on 23/03/2015 11:48:51.

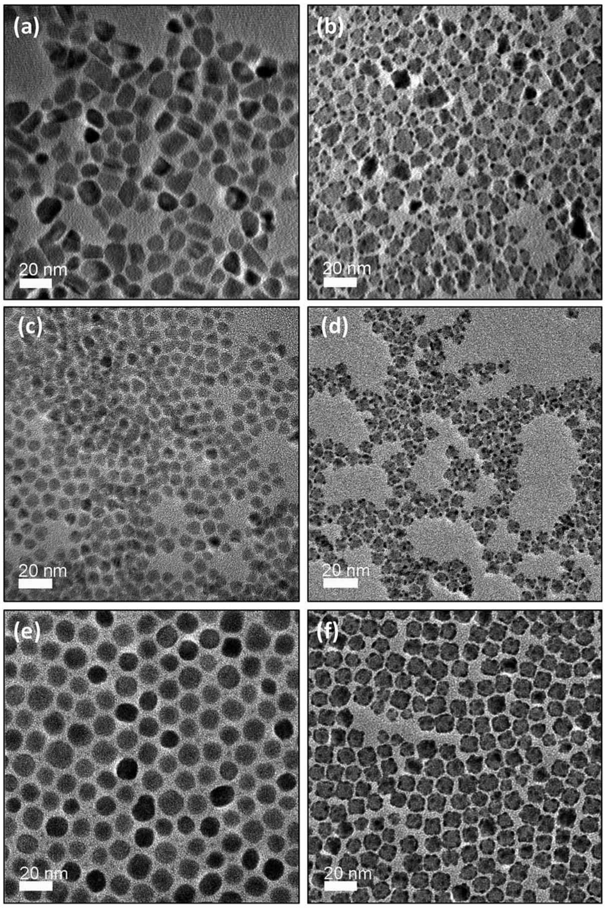

Fig. 46 TEM images of (a) CdS, (b) CdSe and (c) PbS semiconductor nanocrystals, and (d) CdS–Au, (e) CdSe–Au, and (f) PbS–Au nanocomposites. Reproduced from ref. 388 with permission from Wiley-VCH.

and would regenerate the active PbS–Au species for further reactions. By optimizing both the composition and the domain sizes for the nanocomposite system through varying the composition and the ratio of the metal precursor to the semiconductor seeds in the synthesis, a further enhancement in the catalytic activity could be expected. In addition, the noble metal-based nanocomposites could also be of interest as advanced functional materials, and as catalysts for other organic and pharmaceuticals synthesis reactions.

Another important application of noble metal-based nanocomposites is environmental remediation, particularly for the catalytic oxidation of volatile organic compounds (VOCs), *e.g.*, benzene, toluene, and formaldehyde, which have been recognized as major contributors to air pollution, especially in developing countries, and are known to cause the irritation of eyes and respiratory tract, headache, pneumonia, and even cancer.[389,390] Catalytic oxidation is the most effective technology for VOC abatement because VOCs can be oxidized to $CO_2$ over certain catalysts at considerably lower temperatures than in thermal oxidation.[391–393] A large number of noble metal catalysts (Pt, Pd, Rh, Au, Ag) supported on different metal oxide supports have been used for the catalytic oxidation of VOCs. However, the most commonly used strategies for fabricating these noble metal–metal oxide nanocomposites are traditional impregnation methods or flame spray pyrolysis, but the solution-based approaches have not yet been used. Therefore, the applications of the nanocomposites in environmental remediation are not presented in this review work, partly to save space. One can refer to the related literatures to find out the recent advances in this field.[394–399]

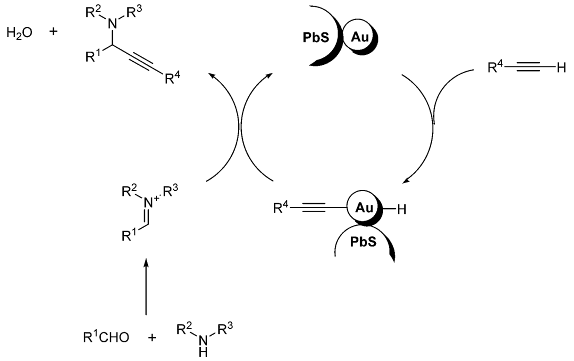

Fig. 47 Schematic illustration showing the tentative mechanism of the PbS–Au catalyzed three-component coupling of an aldehyde, amine and alkyne in water. Reproduced from ref. 388 with permission from Wiley-VCH.

## 10 Conclusion and perspectives

The efforts of many leading research groups have led to a rich variety of composite nanomaterials, and their accumulation has created great opportunities but also presented tremendous challenge to apply these materials in various areas, *e.g.*, structure design, energy conversion, and environmental remediation. In addition, to promote charge separation, an interesting feature for a composite nanoparticle should include electronic coupling between the different domains in the nanocomposites. Future research challenges in composite nanomaterials may include: (1) the phase transfer of semiconductor–metal oxide nanocrystals from organic media to an aqueous medium. Generally, high quality semiconductor–metal oxide nanocrystals are usually synthesized in organic solvents at high temperatures. Their lack of native water solubility severely limits their applications in preparing nanocomposites including noble metals. An effective phase transfer method would circumvent such a deficiency. Future work may begin with the construction of an efficient approach for transferring the semiconductor–metal oxide substrate nanocrystals from organic solvents to aqueous solvent. (2) The deposition of noble metals on different semiconductor substrates. A number of environmental factors, such as initial reactant concentrations, reducing agents, metal precursors, reaction time, reaction temperature, and pH of the reaction medium, systematically affect the deposition of noble metals on different semiconductor substrates. The characterization techniques, including TEM, HRTEM, HAADF-STEM, XRD, XPS, and UV-vis spectroscopy might focus on addressing the following critical

Published on 05 December 2014. Downloaded by Library for Natural Sciences of the RAS on 23/03/2015 11:48:51.

issues: (i) the deposition behavior of metals on semiconductor nanocrystals (wrap around, or only at single/multiple sites); (ii) the morphology change of semiconductor substrates after metal deposition; (iii) the size and morphology of the metal domains; and (iv) the physical and chemical properties of the nanocomposites. (3) Understanding the underlying chemistry for the nanocomposite systems. The systematic identification of the behaviors of the nanocomposites should include the strain or tensile effect of semiconductor substrate particles on the metal components, the relationship between the physical/chemical properties and the particle features, and the coupling effects between the different nanocomposite domains. The mechanistic understanding of the underlying chemistry of the nanocomposite systems might be valuable for the development of more metal-based nanocomposites with interesting architectures and tailored functionalities. (4) Exploration of the catalytic activity of the nanocomposites for energy conversion. The as-synthesized noble metal-based nanocomposites may possess superior properties for highly efficient energy conversion due to their ultrafine size, high stability, ideal morphology, and interesting energy level alignment, some of which are difficult or impossible to achieve by commercial catalysts. The application of these nanocomposites toward direct methanol fuel cells and photocatalysis will accordingly become hot topics. Specific future goals should include the evaluation of the nanocomposites as catalysts for energy conversion, the devices designed with improved performance, efficiency, durability and reduced costs, and the realization of the commercialization of the catalysts as a long-term objective. Furthermore, the catalytic activity of these composite nanomaterials in pharmaceutical syntheses, *e.g.*, in hydrogenation, reductive amination, transfer hydrogenation, hydroamination, might be tested in terms of yield, enantioselectivity, TON (turnover numbers) and recyclability. (5) Exploration of other scientific-related issues. Many interesting scientific findings might be derived from the nanocomposites synthesis and their characterization. For example, the Ostwald ripening process was dynamically observed during the diffusion of Au in $Ag_2S$ nanocrystals. This observation could be used to interpret why the diffusion process does not lead to a homogeneous distribution of Au across the particle. These interesting scientific issues or physical/chemical processes would not only satisfy everlasting human curiosity, but also promise new advances in nanoscience and nanotechnology.

Human being is at the interface of the number of forefront research areas in this period of technological development. Through this research effort, researchers aim to establish a general materials synthesis methodology to influence a rethinking of the current processing technologies: to move towards molecular-level control and regulation, and away from the "top-down" approach and the stringent and expensive control, inherent in conventional manufacturing processes.

## Acknowledgements

Financial support from the 100 Talents Program of the Chinese Academy of Sciences, National Natural Science Foundation of China (no.: 21173226, 21376247), and State Key Laboratory of Multiphase Complex Systems, Institute of Process Engineering, Chinese Academy of Sciences (MPCS-2012-A-11) is gratefully acknowledged.

## Notes and references

1 Y. Xiong and Y. Xia, *Adv. Mater.*, 2007, **19**, 3385.

2 Y. Xia, Y. Xiong, B. Lim and S. E. Skrabalak, *Angew. Chem., Int. Ed.*, 2009, **48**, 60.

3 B. Wiley, T. Herricks, Y. Sun and Y. Xia, *Nano Lett.*, 2004, **4**, 1733.

4 N. R. Jana, L. Gearheart and C. J. Murphy, *J. Phys. Chem. B*, 2001, **105**, 4065.

5 A. Gole and C. J. Murphy, *Chem. Mater.*, 2004, **16**, 3633.

6 T. H. Ha, H. J. Koo and B. H. Chung, *J. Phys. Chem. C*, 2007, **111**, 1123.

7 Y. Sun, B. Mayers and Y. Xia, *Nano Lett.*, 2003, **3**, 675.

8 B. J. Wiley, Z. Wang, J. Wei, Y. Yin, D. H. Cobden and Y. Xia, *Nano Lett.*, 2006, **6**, 2273.

9 X. Sun, S. Dong and E. Wang, *Angew. Chem., Int. Ed.*, 2004, **43**, 6360.

10 B. Liu, J. Xie, J. Y. Lee, Y. P. Ting and J. P. Chen, *J. Phys. Chem. B*, 2005, **109**, 15256.

11 R. Jin, Y. Cao, C. A. Mirkin, K. L. Kelly, G. C. Schatz and J. G. Zheng, *Science*, 2001, **294**, 1901.

12 Y. Sun and Y. Xia, *Science*, 2002, **298**, 2176.

13 D. Yu and V. W.-W. Yam, *J. Phys. Chem. B*, 2005, **109**, 5497.

14 D. Seo, J. C. Park and H. Song, *J. Am. Chem. Soc.*, 2006, **128**, 14863.

15 X. W. Lou, L. A. Archer and Z. Yang, *Adv. Mater.*, 2008, **20**, 3987.

16 H. C. Zeng, *J. Phys. Chem.*, 2006, **16**, 649.

17 F. Caruso, *Chem.–Eur. J.*, 2000, **6**, 413.

18 K. K. Caswell, C. M. Bender and C. J. Murphy, *Nano Lett.*, 2003, **3**, 667.

19 F. Kim and J. H. Song, *J. Am. Chem. Soc.*, 2002, **124**, 14316.

20 S. S. Shankar, A. Rai, B. Ankamwar, A. Singh, A. Ahmad and M. Sastry, *Nat. Mater.*, 2004, **3**, 482.

21 S. W. Kim, M. Kim, W. Y. Lee and T. Hyeon, *J. Am. Chem. Soc.*, 2002, **124**, 7642.

22 N. Toshima and T. Yonezawa, *New J. Chem.*, 1998, **22**, 1179.

23 R. Davies, G. A. Schurr, P. Meenan, R. D. Nelson, H. E. Bergna, C. A. S. Brevett and R. H. Goldbaum, *Adv. Mater.*, 1998, **10**, 1264.

24 L. M. Liz-Marzán, M. Giersig and P. Mulvaney, *Langmuir*, 1996, **12**, 4329.

25 T. A. Taton, C. A. Mirkin and R. L. Letsinger, *Science*, 2000, **289**, 1757.

26 N. Krasteva, I. Besnard, B. Guse, R. E. Bauer, K. Mullen, A. Yasuda and T. Vossmeyer, *Nano Lett.*, 2002, **2**, 551.

27 C. J. Murphy and N. R. Jana, *Adv. Mater.*, 2002, **14**, 80.

28 S. E. Habas, H. Lee, V. Radmilovic, G. A. Somorjai and P. Yang, *Nat. Mater.*, 2007, **6**, 692.

29 J. Luo, L. Wang, D. Mott, P. N. Njoki, Y. Lin, T. He, Z. Xu, B. N. Wanjala, I. S. Lim and C. Zhong, *Adv. Mater.*, 2008, **20**, 4342.

This journal is © The Royal Society of Chemistry 2015

Published on 05 December 2014. Downloaded by Library for Natural Sciences of the RAS on 23/03/2015 11:48:51.

30 S. H. Joo, J. Y. Park, C.-K. Tsung, Y. Yamada, P. Yang and G. A. Somorjai, *Nat. Mater.*, 2009, **8**, 126.

31 W. Zhou, X. Yang, M. B. Vukmirović, B. E. Koel, J. Jiao, G. Peng, M. Mavrikakis and R. R. Adžič, *J. Am. Chem. Soc.*, 2009, **131**, 12755.

32 S. Sun, C. B. Murray, D. Weller, L. Folks and A. Moser, *Science*, 2000, **287**, 1989.

33 E. V. Shevchenko, D. V. Talapin, A. L. Rogach, A. Kornowski, M. Haase and H. Weller, *J. Am. Chem. Soc.*, 2002, **124**, 11480.

34 Z. Liu, J. E. Hu, Q. Wang, K. Gaskell, A. I. Frenkel, G. S. Jackson and B. Eichhorn, *J. Am. Chem. Soc.*, 2009, **131**, 6924.

35 J. Zhang, K. Sasaki and R. R. Adžič, *Science*, 2007, **315**, 220.

36 S. Guo, S. Dong and E. Wang, *J. Phys. Chem. C*, 2008, **112**, 2389.

37 Y. Chen, H. Hung and M. H. Huang, *J. Am. Chem. Soc.*, 2009, **131**, 9114.

38 Z. Peng and H. Yang, *J. Am. Chem. Soc.*, 2009, **131**, 7542.

39 B. Lim, M. Jiang, P. H. C. Camargo, E. C. Cho, J. Tao, X. Lu, Y. Zhu and Y. Xia, *Science*, 2009, **324**, 1302.

40 Y. Kim, J. W. Hong, Y. W. Lee, M. Kim, D. Kim and W. S. Yun, *Angew. Chem., Int. Ed.*, 2010, **122**, 10395.

41 F. Ye, H. Liu, W. Hu, J. Zhong, Y. Chen, H. Cao and J. Yang, *Dalton Trans.*, 2012, **41**, 2898.

42 T. Mokari, E. Rothenberg, I. Popov, R. Costi and U. Banin, *Science*, 2004, **304**, 1787.

43 W. L. Shi, H. Zeng, Y. Sahoo, T. Y. Ohulchanskyy, Y. Ding, Z. L. Wang, M. Swihart and P. N. Prasad, *Nano Lett.*, 2006, **6**, 875.

44 J. Yang, L. Levina, E. H. Sargent and S. O. Kelley, *J. Mater. Chem.*, 2006, **16**, 4025.

45 R. Costi, A. E. Saunders, E. Elmalem, A. Salant and U. Banin, *Nano Lett.*, 2008, **8**, 637.

46 E. Elmalem, A. E. Saunders, R. Costi, A. Salant and U. Banin, *Adv. Mater.*, 2008, **20**, 4312.

47 S. E. Habas, P. D. Yang and T. Mokari, *J. Am. Chem. Soc.*, 2008, **130**, 3294.

48 J. Yang and J. Y. Ying, *Chem. Commun.*, 2009, 3187.

49 J. Yang, E. H. Sargent, S. O. Kelley and J. Y. Ying, *Nat. Mater.*, 2009, **8**, 683.

50 J. Yang and J. Y. Ying, *J. Am. Chem. Soc.*, 2010, **132**, 2114.

51 N. Zhao, L. Li, T. Huang and L. Qi, *Nanoscale*, 2010, **2**, 2418.

52 M. Li, X. F. Yu, S. Liang, X. N. Peng, Z. J. Yang, Y. L. Wang and Q. Q. Wang, *Adv. Funct. Mater.*, 2011, **21**, 1788.

53 J. Qu, H. Liu, Y. Wei, X. Wu, R. Yue, Y. Chen and J. Yang, *J. Mater. Chem.*, 2011, **21**, 11750.

54 W. Hu, H. Liu, F. Ye, Y. Ding and J. Yang, *CrystEngComm*, 2012, **14**, 7049.

55 K. K. Haldar, G. Sinha, J. Lahtinen and A. Patra, *ACS Appl. Mater. Interfaces*, 2012, **4**, 6266.

56 X. Ding, Y. Zou and J. Jiang, *J. Mater. Chem.*, 2012, **22**, 23169.

57 N. E. Motl, J. F. Bondi and R. E. Schaak, *Chem. Mater.*, 2012, **24**, 1552.

58 D. Wang, X. Li, H. Li, L. Li, X. Hong, Q. Peng and Y. Li, *J. Mater. Chem. A*, 2013, **1**, 1587.

59 J. Yang, X. Chen, F. Ye, C. Wang, Y. Zheng and J. Yang, *J. Mater. Chem.*, 2011, **21**, 9088.

60 J. Yang and J. Y. Ying, *Angew. Chem., Int. Ed.*, 2011, **50**, 4637.

61 L. Carbone and P. D. Cozzoli, *Nano Today*, 2010, **5**, 449.

62 Y. Jin and X. Gao, *Nat. Nanotechnol.*, 2009, **4**, 571.

63 J. Zhang, Y. Tang, K. Lee and M. Ouyang, *Nature*, 2010, **466**, 91.

64 M. Jakob and H. Levanon, *Nano Lett.*, 2003, **3**, 353.

65 V. Subramanian, E. Wolf and P. V. Kamat, *J. Am. Chem. Soc.*, 2004, **126**, 4943.

66 A. Salant, E. Amitay-Sadovsky and U. Banin, *J. Am. Chem. Soc.*, 2006, **128**, 10006.

67 G. Ma, J. He, K. Rajiv, S. Tang, Y. Yang and M. Nogami, *Appl. Phys. Lett.*, 2004, **84**, 4684.

68 H. Lin, Y. Chen, J. Wang, D. Wang and C. Chen, *Appl. Phys. Lett.*, 2006, **88**, 161911.

69 A. Dawson and P. V. Kamat, *J. Phys. Chem. B*, 2001, **105**, 96.

70 E. Formo, E. Lee, D. Campbell and Y. Xia, *Nano Lett.*, 2008, **8**, 668.

71 H. Gong, X. Wang, Y. Du and Q. Wang, *J. Chem. Phys.*, 2006, **125**, 024707.

72 J. S. Lee, E. V. Shevchenko and D. V. Talapin, *J. Am. Chem. Soc.*, 2008, **130**, 9673.

73 B. Kraeutler and A. J. Bard, *J. Am. Chem. Soc.*, 1978, **100**, 4317.

74 R. Baba, S. Nakabayashi and A. Fujishima, *J. Phys. Chem.*, 1985, **89**, 1902.

75 I. Pastoriza-Santos, D. S. Koktysh, A. A. Mamedov, M. Giersig, N. A. Kotov and L. M. Liz-Marzan, *Langmuir*, 2000, **16**, 2731.

76 N. Chandrasekharan and P. V. Kamat, *J. Phys. Chem. B*, 2000, **104**, 10851.

77 V. Subramanian, E. Wolf and P. V. Kamat, *J. Phys. Chem. B*, 2001, **105**, 11439.

78 P. V. Kamat, *J. Phys. Chem. B*, 2002, **106**, 7729.

79 T. Hirakawa and P. V. Kamat, *J. Am. Chem. Soc.*, 2005, **127**, 3928.

80 T. Mokari, C. G. Sztrum, A. Salant, E. Rabani and U. Banin, *Nat. Mater.*, 2005, **14**, 855.

81 C. Pacholski, A. Kornowski and H. Weller, *Angew. Chem., Int. Ed.*, 2004, **43**, 4774.

82 F. R. Fan, Y. Ding, D. Y. Liu, Z. Q. Tian and Z. L. Wang, *J. Am. Chem. Soc.*, 2009, **131**, 12036.

83 A. E. Saunders, I. Popov and U. Banin, *J. Phys. Chem. B*, 2006, **110**, 25421.

84 G. Menagen, D. Mocatta, A. Salant, I. Popov, D. Dorfs and U. Banin, *Chem. Mater.*, 2008, **20**, 6900.

85 T. Mokari, A. Aharoni, I. Popov and U. Banin, *Angew. Chem., Int. Ed.*, 2006, **45**, 8001.

86 M. Casavola, V. Grillo, E. Carlino, C. Giannini, F. Gozzo, E. F. Pinel, M. A. Garcia, L. Manna, R. Cingolani and P. D. Cozzoli, *Nano Lett.*, 2007, **7**, 1386.

87 H. Yu, M. Chen, P. M. Rice, S. X. Wang, R. L. White and S. Sun, *Nano Lett.*, 2005, **5**, 379.

88 Y. Li, Q. Zhang, A. V. Nurmikko and S. Sun, *Nano Lett.*, 2005, **5**, 1689.

89 J. Yang, H. I. Elim, Q. Zhang, J. Y. Lee and W. Ji, *J. Am. Chem. Soc.*, 2006, **128**, 11921.

Published on 05 December 2014. Downloaded by Library for Natural Sciences of the RAS on 23/03/2015 11:48:51.

90 D. V. Talapin, H. Yu, E. V. Shevchenko, A. Lobo and C. B. Murray, *J. Phys. Chem. C*, 2007, **111**, 14049.
91 H. Gu, R. Zheng, X. Zhang and B. Xu, *J. Am. Chem. Soc.*, 2004, **126**, 5664.
92 I. Jen-La Plante, S. E. Habas, B. D. Yuhas, D. J. Gargas and T. Mokari, *Chem. Mater.*, 2009, **21**, 3662.
93 Q. F. Zhou, J. C. Bao and Z. Xu, *J. Mater. Chem.*, 2002, **12**, 384.
94 G. Carotenuto and L. Nicolais, *J. Mater. Chem.*, 2003, **13**, 1038.
95 W. Wang, S. Efrima and O. Regev, *Langmuir*, 1998, **14**, 602.
96 N. Lala, S. P. Lalbegi, S. D. Adyanthaya and M. Sastry, *Langmuir*, 2001, **17**, 3766.
97 M. Sastry, *Curr. Sci.*, 2003, **85**, 1735.
98 J. Yang, J. Y. Lee and J. Y. Ying, *Chem. Soc. Rev.*, 2011, **40**, 1672.
99 I. L. Medintz, H. T. Uyeda, E. R. Goldman and H. Mattoussi, *Nat. Mater.*, 2005, **4**, 435.
100 X. Wang, J. Zhuang, Q. Peng and Y. Li, *Nature*, 2005, **437**, 121.
101 B. Cushing, V. L. Kolesnichenko and C. J. O'Connor, *Chem. Rev.*, 2004, **104**, 3893.
102 M. Brust, M. Walker, D. Bethell, D. J. Schiffrin and R. Whyman, *J. Chem. Soc., Chem. Commun.*, 1994, 801.
103 M. Brust, J. Fink, D. Bethell, D. J. Schiffrin and C. Kiely, *J. Chem. Soc., Chem. Commun.*, 1995, 1655.
104 K. Meguro, M. Torizuka and K. Esumi, *Bull. Chem. Soc. Jpn.*, 1988, **61**, 341.
105 K. Meguro, T. Tano, K. Torigoe, H. Nakamura and K. Esumi, *Colloids Surf.*, 1988/1989, **34**, 381.
106 M. J. Hostetler, J. E. Wingate, C. J. Zhong, J. E. Harris, R. W. Vachet, M. R. Clark, J. D. Londono, S. J. Green, J. J. Stokes, G. D. Wignall, G. L. Glish, M. D. Porter, N. D. Evans and R. W. Murray, *Langmuir*, 1998, **14**, 17.
107 R. L. Donkers, Y. Song and R. W. Murray, *Langmuir*, 2004, **20**, 4703.
108 V. L. Jimenez, D. G. Georganopoulou, R. J. White, A. S. Harper, A. J. Mills, D. Lee and R. W. Murray, *Langmuir*, 2004, **20**, 6864.
109 R. H. Terrill, T. A. Postlethwaite, C. H. Chen, C. D. Poon, A. Terzis, A. Chen, J. E. Hutchison, M. R. Clark, G. Wignall, J. D. Londono, R. Superfine, M. Falvo, C. S. Johnson Jr, E. T. Samulski and R. W. Murray, *J. Am. Chem. Soc.*, 1995, **117**, 12537.
110 S. R. Johnson, S. D. Evans and R. Brydson, *Langmuir*, 1998, **14**, 6639.
111 L. A. Porter Jr, D. Ji, S. L. Westcott, M. Graupe, R. S. Czernuszewicz, N. J. Halas and T. R. Lee, *Langmuir*, 1998, **14**, 7378.
112 R. L. Whetten, J. T. Khoury, M. M. Alvarez, S. Murthy, I. Vezmar, Z. L. Wang, P. W. Stephens, C. L. Cleveland, W. D. Luedtke and U. Landman, *Adv. Mater.*, 1996, **8**, 428.
113 S. Chen, A. C. Templeton and R. W. Murray, *Langmuir*, 2000, **16**, 3543.
114 T. G. Schaaff, M. N. Shafigullin, J. T. Khoury, I. Vezmar, R. L. Whetten, W. G. Cullen, P. N. First, C. Gutierrez-Wing, J. Ascensio and M. J. Jose-Yacaman, *J. Phys. Chem. B*, 1997, **101**, 7885.
115 T. G. Schaaff and R. L. Whetten, *J. Phys. Chem. B*, 1999, **103**, 9394.
116 S. L. Horswell, C. J. Kiely, I. A. O'Neil and D. J. Schiffrin, *J. Am. Chem. Soc.*, 1999, **121**, 5573.
117 D. V. Leff, L. Brandt and J. R. Heath, *Langmuir*, 1996, **12**, 4723.
118 K. Wikander, C. Petit, K. Holmberg and M. P. Pileni, *Langmuir*, 2006, **22**, 4863.
119 P. R. Selvakannan, S. Mandal, R. Pasricha and M. Sastry, *J. Colloid Interface Sci.*, 2004, **279**, 124.
120 A. N. Grace and K. Pandian, *J. Phys. Chem. Solids*, 2007, **68**, 2278.
121 Y. Chen and X. Wang, *Mater. Lett.*, 2008, **62**, 2215.
122 X. Song, S. Sun, W. Zhang and Z. Yin, *J. Colloid Interface Sci.*, 2004, **273**, 463.
123 A. Demortiere and C. Petit, *Langmuir*, 2007, **23**, 8575.
124 T. G. Schaaff and A. J. Rodinone, *J. Phys. Chem. B*, 2003, **107**, 10416.
125 H. Shi, X. Fu, X. Zhou and H. Zhengshui, *J. Mater. Chem.*, 2006, **16**, 2097.
126 W. Song, C. Wu, H. Yin, X. Liu, P. Sa and J. Hu, *Anal. Lett.*, 2008, **41**, 2844.
127 J. Yang, J. Y. Lee, T. C. Deivaraj and H.-P. Too, *J. Colloid Interface Sci.*, 2004, **277**, 95.
128 J. Yang, J. Y. Lee and H.-P. Too, *Anal. Chim. Acta*, 2007, **588**, 34.
129 J. Yang, J. Y. Lee, H.-P. Too, G.-M. Chow and L. M. Gan, *Chem. Lett.*, 2005, **34**, 354.
130 J. Yang, J. Y. Lee, H.-P. Too and S. Valiyaveettil, *J. Phys. Chem. B*, 2006, **110**, 125.
131 K. V. Sarathy, G. U. Kulkarni and C. N. R. Rao, *Chem. Commun.*, 1997, 537.
132 K. V. Sarathy, G. Raina, R. T. Yadav, G. U. Kulkarni and C. N. R. Rao, *J. Phys. Chem. B*, 1997, **101**, 9876.
133 S. S. Huang, J. M. Huang, J. A. Yang, J. J. Peng, Q. B. Zhang, F. Peng, H. J. Wang and H. Yu, *Chem.–Eur. J.*, 2010, **16**, 5920.
134 D. S. Ginger and N. C. Greenham, *J. Appl. Phys.*, 2000, **87**, 1361.
135 N. Koch, A. Kahn, J.-J. Pireaux, J. Schwartz, R. L. Johnson and A. Elschner, *Appl. Phys. Lett.*, 2003, **82**, 70.
136 X. G. Peng, L. Manna, W. D. Yang, J. Wickham, E. Scher, A. Kadavanich and A. P. Alivisatos, *Nature*, 2000, **404**, 59.
137 W. C. W. Chan and S. Nie, *Science*, 1998, **281**, 2016.
138 N. Zhao and L. Qi, *Adv. Mater.*, 2006, **18**, 359.
139 J. M. Zhu, Y. H. Shen, A. J. Xie and L. Zhu, *J. Mater. Chem.*, 2009, **19**, 8871.
140 I. Pastoriza-Santos, J. Pérez-Juste and L. M. Liz-Marzán, *Chem. Mater.*, 2006, **18**, 2465.
141 Z. Sun, Z. Yang, J. Zhou, M. H. Yeung, W. Ni, H. Wu and J. Wang, *Angew. Chem., Int. Ed.*, 2009, **48**, 2881.
142 J. Zhang, Y. Tang, K. Lee and M. Ouyang, *Science*, 2010, **327**, 1634.
143 D. H. Son, S. M. Hughes, Y. D. Yin and A. P. Alivisatos, *Science*, 2004, **306**, 1009.

This journal is © The Royal Society of Chemistry 2015

Published on 05 December 2014. Downloaded by Library for Natural Sciences of the RAS on 23/03/2015 11:48:51.

144 R. D. Robinson, B. Sadtler, D. O. Demchenko, C. K. Erdonmez, L. W. Wang and A. P. Alivisatos, *Science*, 2007, **317**, 355.
145 H. Liu, F. Ye, X. Ma, H. Cao and J. Yang, *CrystEngComm*, 2013, **15**, 7740.
146 W. F. Ostwald, *Z. Phys. Chem.*, 1897, **22**, 289.
147 D. V. Talapin, A. L. Rogach, M. Haase and H. Weller, *J. Phys. Chem. B*, 2001, **105**, 12278.
148 G. Dukovic, M. G. Merkle, J. H. Nelson, S. M. Hughes and A. P. Alivisatos, *Adv. Mater.*, 2008, **20**, 4306.
149 J. R. Harbour, R. Wolkow and M. L. Hair, *J. Phys. Chem.*, 1981, **85**, 4026.
150 J. F. Reber and M. Rusek, *J. Phys. Chem.*, 1986, **90**, 824.
151 A. J. Frank, Z. Goren and I. Willner, *Chem. Commun.*, 1986, 1029.
152 L. Manna, E. C. Scher, L. S. Li and A. P. Alicisatos, *J. Am. Chem. Soc.*, 2002, **124**, 7136.
153 A. J. Bard, *IUPAC*, Marcel Dekker, New York, 1985.
154 L. Carbone, S. Kudera, C. Giannini, G. Ciccarella, P. D. Cozzoli and L. Manna, *J. Mater. Chem.*, 2006, **16**, 3952.
155 L. Motte and M. P. Pileni, *J. Phys. Chem. B*, 1998, **102**, 4104.
156 F. Gao, Q. Lu and D. Zhao, *Nano Lett.*, 2003, **3**, 85.
157 J. Liu, P. Raveendran, Z. Shervani and Y. Ikushima, *Chem. Commun.*, 2004, 2582.
158 X. Wang, W. Liu, J. Hao, X. Fu and B. Xu, *Chem. Lett.*, 2005, **34**, 1664.
159 F. Gao, Q. Lu and S. Komarneni, *Chem. Mater.*, 2005, **17**, 856.
160 M. C. Brelle, J. Z. Zhang, L. Nguyen and P. K. Mehra, *J. Phys. Chem. A*, 1999, **103**, 10194.
161 L. Yang, R. Xing, Q. Shen, K. Jiang, J. Wang and Q. Ren, *J. Phys. Chem. B*, 2006, **110**, 10534.
162 X. Mo, M. P. Krebs and S. M. Yu, *Small*, 2006, **2**, 526.
163 Y. N. Tan, J. Yang, J. Y. Lee and D. I. Wang, *J. Phys. Chem. C*, 2007, **111**, 14084.
164 D. E. Eastman, *Phys. Rev. B: Solid State*, 1970, **2**, 1.
165 H. B. Michaelson, *J. Appl. Phys.*, 1977, **48**, 4729.
166 E. Yeager, *Electrochim. Acta*, 1984, **29**, 1527.
167 A. S. Aricò, S. Srinivasan and V. Antonucci, *Fuel Cells*, 2001, **1**, 133.
168 N. M. Marković and P. N. Ross, *Surf. Sci. Rep.*, 2002, **45**, 117.
169 W. Chen, J. Kim, S. Sun and S. Chen, *J. Phys. Chem. C*, 2008, **112**, 3891.
170 I. Toda, H. Iqarashi, H. Uchida and M. Watanabe, *J. Electrochem. Soc.*, 1999, **146**, 3750.
171 J. Zhang, M. B. Vukmirović, K. Sasaki, A. U. Nilekar, M. Mavrikakis and R. R. Adžič, *J. Am. Chem. Soc.*, 2005, **127**, 12480.
172 J. Zhang, M. B. Vukmirović, Y. Xu, M. Mavrikakis and R. R. Adžič, *Angew. Chem., Int. Ed.*, 2005, **44**, 2132.
173 V. R. Stamenković, B. Fowler, B. S. Mun, G. F. Wang, P. N. Ross, C. A. Lucas and N. M. Marković, *Science*, 2007, **315**, 493.
174 V. R. Stamenković, B. S. Mun, M. Arenz, K. J. J. Mayrhofer, C. A. Lucas, G. F. Wang, P. N. Ross and N. M. Marković, *Nat. Mater.*, 2007, **6**, 241.
175 C. Xu and D. W. Goodman, *J. Phys. Chem.*, 1996, **100**, 245.
176 M. Baldauf and D. M. Kolb, *J. Phys. Chem.*, 1996, **100**, 11375.
177 L. A. Kibler and D. M. Kolb, *Z. Phys. Chem.*, 2003, **217**, 1265.
178 I. Chorkendorff and J. W. Niemantsverdriet, *Concepts of modern catalysis and kinetics*, Wiley-VCH, Weinheim, 2003.
179 L. A. Kibler, A. M. El-Aziz, R. Hoyer and D. M. Kolb, *Angew. Chem., Int. Ed.*, 2005, **44**, 2080.
180 S. Kumar and S. Zou, *Langmuir*, 2007, **23**, 7365.
181 H. Naohara, S. Ye and K. Uosaki, *Electrochim. Acta*, 2000, **45**, 3305.
182 H. Naohara, S. Ye and K. Uosaki, *J. Electroanal. Chem.*, 2001, **500**, 435.
183 A. M. El-Aziz and L. A. Kibler, *J. Electroanal. Chem.*, 2002, **534**, 107.
184 L. A. Kibler, A. M. El-Aziz and D. M. Kolb, *J. Mol. Catal. A: Chem.*, 2003, **199**, 57.
185 J. H. Yang, C. H. Cheng, W. Zhou, J. Y. Lee and Z. Liu, *Fuel Cells*, 2010, **10**, 907.
186 J. H. Yang, W. Zhou, C. H. Cheng, J. Y. Lee and Z. Liu, *ACS Appl. Mater. Interfaces*, 2010, **2**, 119.
187 J. H. Yang, J. Y. Lee, Q. Zhang, W. Zhu and Z. Liu, *J. Electrochem. Soc.*, 2008, **155**, B776.
188 S. Chakrabortty, G. Xing, Y. Xu, S. W. Ngiam, N. Mishra, T. C. Sum and Y. Chan, *Small*, 2011, **7**, 2847.
189 H. A. Gasteiger, S. S. Kocha, B. Sompalli and F. T. Wagner, *Appl. Catal., B*, 2005, **56**, 9.
190 H. Liu, C. Song, L. Zhang, J. Zhang, H. Wang and D. P. Wilkinson, *J. Power Sources*, 2006, **155**, 95.
191 E. Antolini, T. Lopes and E. R. Gonzalez, *J. Alloys Compd.*, 2008, **461**, 253.
192 R. R. Adžič, J. Zhang, K. Sasaki, M. B. Vukmirović, M. Shao, J. X. Wang, A. U. Nilekar, M. Mavrikakis, J. A. Valerio and F. Uribe, *Top. Catal.*, 2007, **46**, 249.
193 V. R. Stamenković, T. J. Schmidt, P. N. Ross and N. M. Narković, *J. Phys. Chem. B*, 2002, **106**, 11970.
194 Y. Xu, A. V. Ruban and M. Mavrikakis, *J. Am. Chem. Soc.*, 2004, **126**, 4717.
195 R. G. Allen, C. Lim, L. X. Yang, K. Scott and S. Roy, *J. Power Sources*, 2005, **143**, 142.
196 H. A. Gasteiger, N. M. Marković, P. N. Ross and E. J. Cairms, *J. Phys. Chem.*, 1993, **97**, 12020.
197 J. M. Wang, S. R. Branković, Y. Zhu, J. C. Hanson and R. R. Adžič, *J. Electrochem. Soc.*, 2003, **150**, A1108.
198 E. Antolini, J. R. C. Salgado and E. R. Gonzalez, *J. Electroanal. Chem.*, 2005, **580**, 145.
199 M. Sheldon, P. E. Trudeau, T. Mokari, L. W. Wang and A. P. Alivisatos, *Nano Lett.*, 2009, **9**, 3676.
200 Y. Shemesh, J. E. Macdonald, G. Menagen and U. Banin, *Angew. Chem., Int. Ed.*, 2011, **50**, 1185.
201 E. Shaviv, O. Schubert, M. Alves-Santos, G. Goldoni, R. D. Felice, F. Vallée, N. D. Fatti, U. Banin and C. Sönnichsen, *ACS Nano*, 2011, **5**, 4712.
202 Y. Li, P. Zhou, Z. Dai, Z. Hu, P. Sun and J. Bao, *New J. Chem.*, 2006, **30**, 832.
203 F. Cheng, H. Ma, Y. Li and J. Chen, *Inorg. Chem.*, 2007, **46**, 788.
204 J. Liu, S. Z. Qiao, S. B. Hartono and G. Q. Lu, *Angew. Chem., Int. Ed.*, 2010, **49**, 4981.

Published on 05 December 2014. Downloaded by Library for Natural Sciences of the RAS on 23/03/2015 11:48:51.

205 J. Gao, G. Liang, B. Zhang, Y. Kuang, X. Zhang and B. Xu, *J. Am. Chem. Soc.*, 2007, **129**, 1428.

206 W. Zhao, H. Chen, Y. Li, L. Li, M. Lang and J. Shi, *Adv. Funct. Mater.*, 2008, **18**, 2780.

207 Y. Zhu, T. Ikoma, N. Hanagata and S. Kaskel, *Small*, 2010, **6**, 471.

208 H. P. Liang, H. M. Zhang, J. S. Hu, Y. G. Guo, L. J. Wan and C. L. Bai, *Angew. Chem., Int. Ed.*, 2004, **43**, 1540.

209 H. Liu, J. Qu, Y. Chen, J. Li, F. Ye, J. Y. Lee and J. Yang, *J. Am. Chem. Soc.*, 2012, **134**, 11602.

210 H. Liu, F. Ye, H. Cao, G. Ji, J. Y. Lee and J. Yang, *Nanoscale*, 2013, **5**, 6901.

211 Y. Feng, H. Liu, P. Wang, F. Ye, Q. Tan and J. Yang, *Sci. Rep.*, 2014, **4**, 6204.

212 M. Valden, X. Lai and D. W. Goodman, *Science*, 1998, **281**, 1647.

213 M. S. Chen and D. W. Goodman, *Science*, 2004, **306**, 252.

214 C. Milone, R. Ingoglia and S. Galvagno, *Gold Bull.*, 2006, **39**, 54.

215 Z. P. Liu, X. Q. Gong, J. Kohanoff, C. Sanchez and P. Hu, *Phys. Rev. Lett.*, 2003, **91**, 266102.

216 N. Zheng and G. D. Stucky, *J. Am. Chem. Soc.*, 2006, **128**, 14278.

217 M. Comotti, W. C. Li, B. Spliethoff and F. Schuth, *J. Am. Chem. Soc.*, 2006, **128**, 917.

218 J. D. Grunwaldt and A. Baiker, *J. Phys. Chem. B*, 1999, **103**, 1002.

219 L. M. Molina and B. Hammer, *Phys. Rev. Lett.*, 2003, **90**, 206102.

220 M. Haruta, T. Kobayashi, H. Sano and N. Yamada, *Chem. Lett.*, 1987, **2**, 405.

221 M. Haruta, N. Yamada, T. Kobayashi and S. Iijima, *J. Catal.*, 1989, **115**, 301.

222 A. S. K. Hashmi and G. J. Hutchings, *Angew. Chem., Int. Ed.*, 2006, **45**, 7896.

223 X. Wang, N. Na, S. Zhang, Y. Wu and X. Zhang, *J. Am. Chem. Soc.*, 2012, **129**, 6062.

224 A. A. Herzing, C. J. Kiely, A. F. Carley, P. Landon and G. J. Hutchings, *Science*, 2008, **321**, 1331.

225 S. Laursen and S. Linic, *Phys. Rev. Lett.*, 2006, **97**, 026101.

226 C. Wang, C. Xu, H. Zeng and S. Sun, *Adv. Mater.*, 2009, **21**, 3045.

227 M. I. Brittan, H. Bliss and C. A. Walker, *AIChE J.*, 1970, **16**, 305.

228 G. C. Bond, L. R. Molloy and M. J. Fuller, *J. Chem. Soc., Chem. Commun.*, 1975, 796.

229 J. P. Dauchot and J. P. Dath, *J. Catal.*, 1984, **86**, 373.

230 M. N. Desai, J. B. Butt and J. S. Dranoff, *J. Catal.*, 1983, **79**, 95.

231 R. M. Finch, N. A. Hodge, G. J. Hutchings, A. Meagher, Q. A. Pankhurst, M. R. H. Siddiqui, F. E. Wagner and R. Whyman, *Phys. Chem. Chem. Phys.*, 1999, **1**, 485.

232 S. Golunski, R. Rajaram, N. Hodge, G. J. Hutchings and C. J. Kiely, *Catal. Today*, 2002, **72**, 107.

233 M. J. Kahlich, H. A. Gasteiger and R. J. Behm, *J. Catal.*, 1999, **182**, 430.

234 B. Qiao and Y. Deng, *Chem. Commun.*, 2003, 2192.

235 G. Avgouropoulos, T. Ioannides, C. Papadopoulou, J. Batista, S. Hocevar and H. K. Matralis, *Catal. Today*, 2002, **75**, 157.

236 G. Avgouropoulos, T. Ioannides, H. K. Matralis, J. Batista and S. Hocevar, *Catal. Lett.*, 2001, **73**, 33.

237 P. Landon, J. Ferguson, B. E. Solsona, T. Garcia, A. F. Carley, A. A. Herzing, C. J. Kiely, S. E. Golunski and G. J. Hutchings, *Chem. Commun.*, 2005, 3385.

238 P. Landon, J. Ferguson, B. E. Solsona, T. Garcia, S. Al-Sayari, A. F. Carley, A. A. Herzing, C. J. Kiely, M. Makkee, J. A. Moulijn, A. Overweg, S. E. Golunski and G. J. Hutchings, *J. Mater. Chem.*, 2006, **16**, 199.

239 F. Moreau, G. C. Bond and A. O. Taylor, *J. Catal.*, 2005, **231**, 105.

240 R. Zanella, S. Giorgio, C. R. Henry and C. Louis, *J. Phys. Chem. B*, 2002, **106**, 7634.

241 R. Zanella, L. Delannoy and C. Louis, *Appl. Catal., A*, 2005, **291**, 62.

242 R. Zanella and C. Louis, *Catal. Today*, 2005, **107–108**, 768.

243 W. C. Li, M. Comotti and F. Schueth, *J. Catal.*, 2006, **237**, 190.

244 G. C. Bond and D. T. Thompson, *Gold Bull.*, 2000, **33**, 41.

245 H. H. Kung, M. C. Kung and C. K. Costello, *J. Catal.*, 2003, **216**, 425.

246 M. S. Chen and D. W. Goodman, *Catal. Today*, 2006, **111**, 22.

247 S. Sun, H. Zeng, D. B. Robinson, S. Raoux, P. M. Rice, S. X. Wang and G. Li, *J. Am. Chem. Soc.*, 2004, **126**, 273.

248 C. Xu, J. Xie, D. Ho, C. Wang, N. Kohler, E. G. Walsh, J. R. Morgan, Y. E. Chin and S. Sun, *Angew. Chem., Int. Ed.*, 2008, **47**, 173.

249 K. Sokolov, M. Follen, J. Aaron, I. Pavlova, A. Malpica, R. Lotan and R. Richards-Kortum, *Cancer Res.*, 2003, **63**, 1999.

250 D. A. Schultz, *Curr. Opin. Biotechnol.*, 2003, **14**, 13.

251 I. H. El-Sayed, X. H. Huang and M. A. El-Sayed, *Nano Lett.*, 2005, **5**, 829.

252 A. K. Gupta, R. R. Naregalkar, V. D. Vaidya and M. Gupta, *Nanomedicine*, 2007, **2**, 23.

253 J. E. Lee, N. Lee, H. Kim, J. Kim, S. H. Choi, J. H. Kim, T. Kim, I. C. Song, S. P. Park, W. K. Moon and T. Hyeon, *J. Am. Chem. Soc.*, 2010, **132**, 552.

254 K. Cheng, S. Peng, C. Xu and S. Sun, *J. Am. Chem. Soc.*, 2009, **131**, 10637.

255 B. Wang, C. Xu, J. Xie, Z. Yang and S. Sun, *J. Am. Chem. Soc.*, 2008, **130**, 14436.

256 Q. Tian, J. Hu, Y. Zhu, R. Zou, Z. Chen, S. Yang, R. Li, Q. Su, Y. Han and X. Liu, *J. Am. Chem. Soc.*, 2013, **135**, 8571.

257 N. Lee, H. R. Cho, M. H. Oh, S. H. Lee, K. Kim, B. H. Kim, K. Shin, T. Y. Ahn, J. W. Choi, Y. W. Kim, S. H. Choi and T. Hyeon, *J. Am. Chem. Soc.*, 2012, **134**, 10309.

258 J. Xie, K. Chen, H. Y. Lee, C. Xu, A. R. Hsu, S. Peng, X. Chen and S. Sun, *J. Am. Chem. Soc.*, 2008, **130**, 7542.

259 C. Xu, B. Wang and S. Sun, *J. Am. Chem. Soc.*, 2009, **131**, 4216.

260 C. Wang, Y. Wei, H. Jiang and S. Sun, *Nano Lett.*, 2009, **9**, 4544.

This journal is © The Royal Society of Chemistry 2015

Published on 05 December 2014. Downloaded by Library for Natural Sciences of the RAS on 23/03/2015 11:48:51.

261 Y. Lee, M. A. Garcia, N. A. F. Huls and S. Sun, *Angew. Chem., Int. Ed.*, 2010, **49**, 1271.
262 C. Wang, H. Daimon and S. Sun, *Nano Lett.*, 2009, **9**, 1493.
263 C. Wang, H. Yin, S. Dai and S. Sun, *Chem. Mater.*, 2010, **22**, 3277.
264 Y. Yu, K. Sun, Y. Tian, X. Z. Li, M. J. Kramer, D. J. Sellmyer, J. E. Shield and S. Sun, *Nano Lett.*, 2013, **13**, 4975.
265 X. Sun, S. Guo, Y. Lu and S. Sun, *Nano Lett.*, 2012, **12**, 4859.
266 J. Xie, F. Zhang, M. Aronova, L. Zhu, X. Lin, Q. Quan, G. Liu, G. Zhang, K. Y. Choi, K. Kim, X. Sun, S. Lee, S. Sun, R. Leapman and X. Chen, *ACS Nano*, 2011, **5**, 3043.
267 S. Chandra, N. A. F. Huls, M. H. Phan, S. Srinath, M. A. Garcia, Y. Lee, C. Wang, S. Sun, Ò. Iglesias and H. Srikanth, *Nanotechnology*, 2014, **25**, 055702.
268 H. Gu, Z. Yang, J. Gao, C. K. Chang and B. Xu, *J. Am. Chem. Soc.*, 2005, **127**, 34.
269 J. Jiang, H. Gu, H. Shao, E. Devlin, G. C. Papaefthymiou and J. Y. Ying, *Adv. Mater.*, 2008, **20**, 4403.
270 R. Costi, A. E. Saunders and U. Banin, *Angew. Chem., Int. Ed.*, 2010, **49**, 4878.
271 P. D. Cozzoli, T. Pellegrino and L. Manna, *Chem. Soc. Rev.*, 2006, **35**, 1195.
272 Y. Jang, J. Chung, S. Kim, S. W. Jun, B. H. Kim, D. W. Lee, B. M. Kim and T. Hyeon, *Phys. Chem. Chem. Phys.*, 2011, **13**, 2512.
273 H. Yin, C. Wang, H. Zhu, S. H. Overbury and S. Sun, *Chem. Commun.*, 2008, 4357.
274 Y. Feng, J. Yang, H. Liu, F. Ye and J. Yang, *Sci. Rep.*, 2014, **4**, 3813.
275 H. Liu, Y. Feng, H. Cao and J. Yang, *Nano-Micro Lett.*, 2014, **6**, 252.
276 J.-S. Choi, Y.-W. Jun, S.-I. Yeon, H. C. Kim, J.-S. Shin and J. Cheon, *J. Am. Chem. Soc.*, 2006, **128**, 15982.
277 A. Figuerola, A. Fiore, R. D. Corato, A. Falqiu, C. Giannini, E. Micotti, A. Lascialfari, M. Corti, R. Cingolani, T. Pellegrino, P. D. Cozzoli and L. Manna, *J. Am. Chem. Soc.*, 2008, **130**, 1477.
278 M. R. Buck, J. F. Bondi and R. E. Schaak, *Nat. Chem.*, 2012, **4**, 37.
279 S. J. Tauster, S. C. Fung, R. T. K. Baker and J. A. Horsley, *Science*, 1981, **211**, 1121.
280 S. J. Tauster, *Acc. Chem. Res.*, 1987, **20**, 389.
281 D. W. Goodman, *Catal. Lett.*, 2005, **99**, 1.
282 J. A. Horsley, *J. Am. Chem. Soc.*, 1979, **101**, 2870.
283 J. Ohyama, A. Yamamoto, K. Teramura, T. Shishido and T. Tanaka, *ACS Catal.*, 2011, **1**, 187.
284 Z.-H. Qin, M. Lewandowski, Y.-N. Sun, S. Shaikhutdinov and H. J. Freund, *J. Phys. Chem. C*, 2008, **112**, 10209.
285 J. S. Beveridge, M. R. Buck, J. F. Bondi, R. Misra, P. Schiffer, R. E. Schaak and M. E. Williams, *Angew. Chem., Int. Ed.*, 2011, **50**, 9875.
286 A. H. Latham, R. S. Frietas, P. Schiffer and M. E. Williams, *Anal. Chem.*, 2005, **77**, 5055.
287 J. S. Beveridge, J. R. Stephens, A. H. Latham and M. E. Williams, *Anal. Chem.*, 2009, **81**, 9618.
288 G. Chen, Y. Wang, L. H. Tan, M. Yang, L. S. Tan, Y. Chen and H. Chen, *J. Am. Chem. Soc.*, 2009, **131**, 4218.
289 Y. Wang, G. Chen, M. Yang, G. Silber and S. Xing, A systems approach towards the stoichiometry-controlled heteroassembly of nanoparticles, *Nat. Commun.*, 2010, **1**, 83.
290 B. M. Leonard, M. E. Anderson, K. D. Oyler, T.-H. Phan and R. E. Schaak, *ACS Nano*, 2009, **3**, 940.
291 P. Wang, H. Liu, Q. Tan and J. Yang, *RSC Adv.*, 2014, **4**, 42839.
292 C. Burda, X. B. Chen, R. Narayanan and M. A. El-Sayed, *Chem. Rev.*, 2005, **105**, 1025.
293 R. Ferrando, J. Jellinek and R. L. Johnston, *Chem. Rev.*, 2008, **108**, 845.
294 R. W. Murray, *Chem. Rev.*, 2008, **108**, 2688.
295 K. Watanabe, D. Menzel, N. Nilius and H.-J. Freund, *Chem. Rev.*, 2006, **106**, 4301.
296 M.-C. Daniel and D. Astruc, *Chem. Rev.*, 2004, **104**, 293.
297 L. Brus, *Acc. Chem. Res.*, 2008, **41**, 1742.
298 S. Laurent, D. Forge, M. Port, A. Roch, C. Robic, L. V. Elst and R. N. Muller, *Chem. Rev.*, 2008, **108**, 2064.
299 G. Cao, *Synthesis properties and applications*, Imperial College Press, London, 2004.
300 P. C. Anderson and K. L. Rowlen, *Appl. Spectrosc.*, 2002, **56**, 124A.
301 E. Hutter and J. H. Fendler, *Adv. Mater.*, 2004, **16**, 1685.
302 W. P. Lim, Z. Zhang, H. Y. Low and W. S. Chin, *Angew. Chem., Int. Ed.*, 2004, **43**, 5685.
303 W. J. Lou, X. B. Wang, M. Chen, W. M. Liu and J. C. Hao, *Nanotechnology*, 2008, **19**, 225607.
304 Y. Du, B. Xu, T. Fu, M. Cai, F. Li, Y. Zhang and Q. Wang, *J. Am. Chem. Soc.*, 2010, **132**, 1470.
305 S. Shen, J. Zhang, L. Peng, Y. Du and Q. Wang, *Angew. Chem., Int. Ed.*, 2011, **50**, 7115.
306 Y. Zhang, G. Hong, Y. Zhang, G. Chen, F. Li, H. Dai and Q. Wang, *ACS Nano*, 2012, **6**, 3695.
307 P. Jiang, Z.-Q. Tian, C.-N. Zhu, Z.-L. Zhang and D.-W. Pang, *Chem. Mater.*, 2012, **24**, 3.
308 D. Wang, T. Xie, Q. Peng and Y. Li, *J. Am. Chem. Soc.*, 2008, **130**, 4016.
309 G. Zhu and Z. Xu, *J. Am. Chem. Soc.*, 2011, **133**, 148.
310 D. O. Demchenko, R. D. Robinson, B. Sadtler, C. K. Erdonmez, A. P. Alivisatos and L. Wang, *ACS Nano*, 2008, **2**, 627.
311 P. Peng, B. Sadtler, A. P. Alivisatos and R. J. Saykally, *J. Phys. Chem. C*, 2010, **114**, 5879.
312 M. Pang, J. Hu and H. Zeng, *J. Am. Chem. Soc.*, 2010, **132**, 10771.
313 H. Liu, W. Hu, F. Ye, Y. Ding and J. Yang, *RSC Adv.*, 2013, **3**, 616.
314 V. K. LaMer, *J. Am. Chem. Soc.*, 1950, **72**, 4847.
315 S. M. Saraiva and J. F. de Oliveira, *J. Dispersion Sci. Technol.*, 2002, **23**, 837.
316 J. Svoboda, F. D. Fischer, P. Fratzl and A. Kroupa, *Acta Mater.*, 2002, **50**, 1369.
317 K. Matsukawa, K. Shirai, H. Yamaguchi and H. Katayama-Yoshida, *Phys. B*, 2007, **401–402**, 151.
318 A. Höglund, C. W. M. Castleton and S. Mirbt, *Phys. Rev. B: Condens. Matter Mater. Phys.*, 2008, **77**, 113201.

View Article Online

Published on 05 December 2014. Downloaded by Library for Natural Sciences of the RAS on 23/03/2015 11:48:51.

319 V. I. Baykov, P. A. Korzhavyi and B. Johansson, *Phys. Rev. Lett.*, 2008, **101**, 177204.

320 H.-C. Yu, A. Van der Ven and K. Thornton, *Appl. Phys. Lett.*, 2008, **93**, 091908.

321 A. Van der Ven, H.-C. Yu, G. Ceder and K. Thornton, *Prog. Mater. Sci.*, 2010, **55**, 61.

322 G. Schmid, *Chem. Rev.*, 1992, **92**, 1709.

323 A. P. Alivisatos, *J. Phys. Chem.*, 1996, **100**, 13226.

324 S. Nie and S. R. Emory, *Science*, 1997, **275**, 1102.

325 I. R. Franchini, G. Bertoni, A. Falqui, C. Giannini, L. W. Wang and L. Manna, *J. Mater. Chem.*, 2010, **20**, 1357.

326 A. Henglein, A. Holzwartb and P. Mulvaney, *J. Phys. Chem.*, 1992, **96**, 8700.

327 A. Courty, A.-I. Henry, N. Goubet and M. P. Pileni, *Nat. Mater.*, 2007, **6**, 900.

328 E. Ramirez, L. Eradès, K. Philippot, P. Lecante and B. Chaudret, *Adv. Funct. Mater.*, 2007, **17**, 2219.

329 S. H. Johnson, C. L. Johnson, S. J. May, S. Hirsch, M. W. Cole and J. E. Spanier, *J. Mater. Chem.*, 2010, **20**, 439.

330 M. Grouchko, I. Popov, V. Uvarov, S. Magdassi and A. Kamyshny, *Langmuir*, 2009, **25**, 2501.

331 D. V. Radziuk, W. Zhang, D. Shchukin and H. Möhwald, *Small*, 2010, **6**, 545.

332 E. Antolini, *Mater. Chem. Phys.*, 2003, **78**, 563.

333 M. L. Perry and T. F. Fuller, *J. Electrochem. Soc.*, 2002, **149**, S59.

334 B. C. H. Steele and A. Heinzel, *Nature*, 2004, **414**, 345.

335 X. Wang, M. Waje and Y. Yan, *J. Electrochem. Soc.*, 2004, **151**, A2183.

336 J. Chen, B. Lim, E. P. Lee and Y. Xia, *Nano Today*, 2009, **4**, 81.

337 Z. Peng and H. Yang, *Nano Today*, 2009, **4**, 143.

338 B. Y. Xia, H. B. Wu, Y. Yan, X. W. Low and X. Wang, *J. Am. Chem. Soc.*, 2013, **135**, 9480.

339 F. Liu, G. Lu and C.-Y. Wang, *J. Electrochem. Soc.*, 2006, **153**, A543.

340 C. Y. Du, T. S. Zhao and W. W. Yang, *Electrochim. Acta*, 2007, **52**, 5266.

341 N. Jia, M. C. Lefebvre, J. Halfyard, Z. Qi and P. G. Pickup, *Electrochem. Solid-State Lett.*, 2000, **3**, 529.

342 B. Gurau and E. S. Smotkin, *J. Power Sources*, 2002, **112**, 339.

343 Y.-M. Kim, K.-W. Park, J.-H. Choi, I.-S. Park and Y.-H. Sung, *Electrochem. Commun.*, 2003, **5**, 571.

344 A. K. Sahu, S. Pitchumani, P. Sridhar and A. K. Shukla, *Bull. Mater. Sci.*, 2009, **32**, 285.

345 H. Zhang, H. Huang and P. K. Shen, *Int. J. Hydrogen Energy*, 2012, **37**, 6875.

346 Y. Zhang, W. Cai, F. Si, J. Ge, L. Liang, C. Liu and W. Xing, *Chem. Commun.*, 2012, **48**, 2870.

347 C. Beauger, G. Lainé, A. Burr, A. Taguet, B. Otazaghine and A. Rigacci, *J. Membr. Sci.*, 2013, **130**, 167.

348 D. S. Cameron, G. A. Hards, B. Harrison and R. J. Potter, *Platinum Met. Rev.*, 1987, **31**, 173.

349 R. Ferrigno, A. D. Stroock, T. D. Clark, M. Mayer and G. M. Whitesides, *J. Am. Chem. Soc.*, 2002, **124**, 12930.

350 R. S. Jayashree, D. Egas, J. S. Spendelow, D. Natarajan, L. J. Markoski and P. J. A. Kenis, *Electrochem. Solid-State Lett.*, 2006, **9**, A252.

351 A. Lam, D. P. Wilkinson and J. Zhang, *Electrochim. Acta*, 2008, **53**, 6890.

352 A. Lam, D. P. Wilkinson and J. Zhang, *J. Power Sources*, 2009, **194**, 991.

353 A. Lam, M. S. Dara, D. P. Wilkinson and K. Fatih, *Electrochem. Commun.*, 2012, **17**, 22.

354 S. Tominaka, S. Ohta, H. Obata, T. Momma and T. Osaka, *J. Am. Chem. Soc.*, 2008, **130**, 10456.

355 K. Cheng and S. Sun, *Nano Today*, 2010, **5**, 183.

356 A. Sitt, I. Hadar and U. Banin, *Nano Today*, 2013, **8**, 494.

357 C. Xu and S. Sun, *Adv. Drug Delivery Rev.*, 2013, **65**, 732.

358 U. Banin, Y. Ben-Shahar and K. Vinokurov, *Chem. Mater.*, 2014, **26**, 97.

359 S. Sun, *J. Inorg. Organomet. Polym.*, 2014, **24**, 33.

360 N. Miyachi, F. Kanada and M. Shibasaki, *J. Org. Chem.*, 1989, **54**, 3511.

361 M. A. Huffman, N. Yasuda, A. E. Decamp and E. J. J. Grabowski, *J. Org. Chem.*, 1995, **60**, 1590.

362 M. Miura, M. Enna, K. Okuro and M. Nomura, *J. Org. Chem.*, 1995, **60**, 4999.

363 T. Naota, H. Takaya and S.-I. Murahashi, *Chem. Rev.*, 1998, **98**, 2599.

364 J. J. Fleming and J. Du Bois, *J. Am. Chem. Soc.*, 2006, **128**, 3926.

365 L. Zani and C. Bolm, *Chem. Commun.*, 2006, 4263.

366 P. Li, Y. Zhang and L. Wang, *Chem.–Eur. J.*, 2009, **15**, 2045.

367 L. Shi, Y.-Q. Tu, M. Wang, F.-M. Zhang and C.-A. Fan, *Org. Lett.*, 2004, **6**, 1001.

368 N. Gommermann and P. Knochel, *Chem.–Eur. J.*, 2006, **12**, 4380.

369 C. Wei, Z. Li and C.-J. Li, *Org. Lett.*, 2003, **5**, 4473.

370 X. Yao and C.-J. Li, *Org. Lett.*, 2005, **7**, 4395.

371 K. M. Reddy, N. S. Babu, I. Suryanarayana, P. S. S. Prasad and N. Lingaiah, *Tetrahedron Lett.*, 2006, **47**, 7563.

372 Y. Zhang, A. M. Santos, E. Herdtweck, J. Mink and F. E. Kühn, *New J. Chem.*, 2005, **29**, 366.

373 C. Wei and C.-J. Li, *J. Am. Chem. Soc.*, 2003, **125**, 9584.

374 B. Huang, X. Yao and C.-J. Li, *Adv. Synth. Catal.*, 2006, **348**, 1528.

375 V. K.-Y. Lo, Y. Liu, M.-K. Wong and C.-M. Che, *Org. Lett.*, 2006, **8**, 1529.

376 V. K.-Y. Lo, K. K.-Y. Kung, M.-K. Wong and C.-M. Che, *J. Organomet. Chem.*, 2009, **694**, 583.

377 C. Fischer and E. M. Carreira, *Org. Lett.*, 2001, **3**, 4319.

378 P.-H. Li and L. Wang, *Chin. J. Chem.*, 2005, **23**, 1076.

379 C.-J. Li and C. Wei, *Chem. Commun.*, 2002, 268.

380 B. M. Choudary, C. Sridhar, M. L. Kantam and B. Sreedhar, *Tetrahedron Lett.*, 2004, **45**, 7319.

381 M. Wang, P. Li and L. Wang, *Eur. J. Org. Chem.*, 2008, 2255.

382 P. Li and L. Wang, *Tetrahedron*, 2007, **63**, 5455.

383 M. L. Kantam, S. Laha, J. Yadav and S. Bhargava, *Tetrahedron Lett.*, 2008, **49**, 3083.

384 Z. Li, C. Wei, L. Chen, R. S. Varma and C.-J. Li, *Tetrahedron Lett.*, 2004, **45**, 2443.

This journal is © The Royal Society of Chemistry 2015

Published on 05 December 2014. Downloaded by Library for Natural Sciences of the RAS on 23/03/2015 11:48:51.

385 M. Kidwai, V. Bansal, A. Kumar and S. Mozumdar, *Green Chem.*, 2007, **9**, 742.

386 X. Zhang and A. Corma, *Angew. Chem., Int. Ed.*, 2008, **47**, 4358.

387 M. L. Kantam, B. V. Prakash, C. R. V. Reddy and B. Sreedhar, *Synlett*, 2005, 2329.

388 L. L. Chng, J. Yang, Y. Wei and J. Y. Ying, *Adv. Synth. Catal.*, 2009, **351**, 2887.

389 J. J. Collins, R. Ness, R. W. Tyl, N. Krivanek, N. A. Esmen and T. A. Hall, *Regul. Toxicol. Pharmacol.*, 2001, **34**, 17.

390 A. P. Jones, *Atmos. Environ.*, 1999, **33**, 4535.

391 J. J. Spivey, *Ind. Eng. Chem. Res.*, 1987, **26**, 2165.

392 S. Scirè, S. Minicò, C. Crisafulli and S. Galvagno, *Catal. Commun.*, 2001, **2**, 229.

393 S. Scirè, S. Minicò, C. Crisafulli, C. Satriano and A. Pistone, *Appl. Catal., B*, 2003, **40**, 43.

394 T. Garcia, W. Weng, B. Solsona, E. Carter, A. F. Carley, C. J. Kiely and S. H. Taylor, *Catal. Sci. Technol.*, 2011, **1**, 1367.

395 B. Solsona, E. Aylón, R. Murillo, A. M. Mastral, A. Monzonís, S. Agouram, R. E. Davies, S. H. Taylor and T. Garcia, *J. Hazard. Mater.*, 2011, **187**, 544.

396 C. Zhang, F. Liu, Y. Zhai, H. Ariga, N. Yi, Y. Liu, K. Asakura, M. Flytzani-Stephanopoulos and H. He, *Angew. Chem., Int. Ed.*, 2012, **51**, 9628.

397 M. N. Taylor, W. Zhou, T. Garcia, B. Solsona, A. F. Carley, C. J. Kiely and S. H. Taylor, *J. Catal.*, 2012, **285**, 103.

398 G. Liu, K. Yang, J. Li, W. Tang, J. Xu, H. Liu, R. Yue and Y. Chen, *J. Phys. Chem. C*, 2014, **118**, 22719.

399 Z. Li, K. Yang, G. Liu, G. Deng, J. Li, G. Li, R. Yue, J. Yang and Y. Chen, *Catal. Lett.*, 2014, **144**, 1080.